Development of Thermoplastic Foams with Heterogeneous Cellular Structures for Acoustic Applications

By

Ibrahim Samir Saad Naeem

A Thesis Submitted in Partial Fulfillment
of the Requirements for the Degree of
Doctor of Philosophy
in

The Faculty of Engineering and Applied Science
Mechanical Engineering Program

University of Ontario Institute of Technology

August 2016

Abstract

Manufacture of heterogeneous thermoplastic foams is of great interest to automotive, transportation, and building industries, owing to their capability of damping low frequency noise. Unfortunately, most of the fabrication methods reported in literature either use cumbersome batch processes which have long processing times and produce small sized samples, or produce foams that are not appropriate for sound absorption applications.

In this context, this work aimed at manufacturing of thermoplastic acoustic foams with double porosity and graded porosity by processes that can potentially be scaled up for mass production. To this end, three different strategies were proposed and examined in this thesis. In the first approach, bimodal porous foams were developed by foaming a low melt strength polymer in presence of additives, such as sodium bicarbonate and wollastonite that can increase the population of small cells. Double porosity foams were also developed by foaming a base polymer after blending it with another low melt strength polymer to introduce large cells into its fine cellular structure. A third approach was utilized to produce graded porous foams by applying a temperature gradient to induce varying pre-foaming during compression molding followed by oven expansion.

Experimental results showed that foams containing a combination of small cells and large cells were developed by simultaneous addition of wollastonite and sodium bicarbonate. Compared with homogeneous sample, sound absorption coefficient of the sample prepared by 1% wollastonite and 1% sodium bicarbonate increased from 0.11 to 0.53 at 250Hz, from 0.21 to 0.72 at 500Hz, and from 0.20 to 0.61 at 1000Hz. Cells larger than 2mm were developed within a finer cellular structure by addition of a low melt strength EVA grade to a foamable base polymer. Addition of 5%wt. of the polymer increased sound absorption coefficient from 0.11 to 0.42 at 250 Hz, from 0.20 to 0.56 at 500Hz, and from 0.20 to 0.55 at 1000Hz. The porosity gradient developed across the foam sample increased when the temperature gradient increased, and a porosity difference of 9.1%was developed when imposing a temperature gradient of 60°C for 4 min. For these conditions, sound absorption coefficient increased from 0.12 to 0.33 at 250Hz, from 0.26 to 0.59 at 500Hz and from 0.25 to 0.62 at 1000Hz.

Acknowledgements

First of all, I give all the glory and praise to my God for he has guided me and brought me to this very hour. All my power and wisdom came from Him and here I humbly worship and praise Him with all my heart.

I would like to express my sincere gratitude and deep appreciation to my advisors, Dr. Atef Mohany and Dr. Ghaus Rizvi, for their encouragement and guidance during the entire course of this research project.

I would also like to thank Dr. Hossam Kishawy, Dr. Remon Pop-Iliev, Dr. Xiaodong Lin and Dr. Laurent Matuana for agreeing to serve on my doctoral committee. I am thankful to them for their valuable suggestions and advice.

Also I would like to extend my thanks to everyone in the Aeroacoustics and Noise Control Lab at the University of Ontario Institute of Technology for their continual support, encouragement and valuable suggestions

Last but not least, I would like to thank my parents, parents-in-law, and my brothers for their constant love and prayer for my PhD study. Finally it is time to thank my beloved wife, Heba, Frankly, I don't even know how much I owed her during my study, because she afforded a lot and sacrificed herself to support me in my study. Now I promise that I will be beside her and make her happy in the rest of my life.

Table of Contents

List of Tables

List of Figures

List of Symbols

Symbol	Parameters
a	Radius of impedance tube (m)
A_{air}	Absorption term related to air
b	Diameter of the holes in Helmholtz resonator
B	Center to center hole distance in Helmholtz resonator
c_0	Speed of sound (m/s)
C_0	Concentration of gas molecules in solution
d	Material thickness
D	Diameter of impedance tube (m)
f	Frequency of sound wave (Hz)
f_0	Frequency factor of gas molecules joining the nucleus
f_l	Lower frequency limit (Hz)
f_u	Upper frequency limit (Hz)
$f(\theta)$	Heterogeneity factor
ΔG^*_{hetero}	Gibbs free energy in heterogeneous nucleation
ΔG^*_{homo}	Gibbs free energy in homogeneous nucleation
h	Thickness of the micro-perforated sheet
H_{12}	Transfer function between microphones 1 and 2
H_i	Imaginary part of the transfer function between microphones 1 and 2
H_r	Real part of the transfer function between microphones 1 and 2
I_i	Intensity of incident sound waves
I_r	Intensities of reflected sound waves
j	$=\sqrt{-1}$
k	Boltzmann constant
$\bar{k}$	Wavenumber of sound wave
l	Depth of the air gap behind the resonator
l_x, l_y, l_z	Dimensions of the room (m)

L	Optical path length
L_i	Optical path length within material (i)
m	Absorption of air
M	Distance between the sample and the farther microphone
M_1	Distance between microphone 1 and speaker (m)
M_2	Distance between microphone 3 and sample (m)
M_3	Total length of impedance tube (m)
$\bar{M}_v$	Viscosity average molecular weight (g/mol)
N^*_{homo}	Rate of homogeneous nucleation
p	Acoustic pressure
p_i	Pressure of incident sound wave
p_r	Pressure of reflected sound wave
P_i	Amplitude of incident pressure wave
P_f	Foaming pressure in solid state foaming (MPa)
P_s	Surrounding pressure
P_{sat}	Saturation pressure
ΔP	Pressure drop across the sample (Pa)
q_1	Separation between microphones 1 and 3 (m)
q_2	Separation between microphones 2 and 3 (m)
q_3	Separation between microphones 1 and 2 (m)
Q	Volumetric flow rate (m^3/s)
r^*	Radius of critical nucleus
R	Sound reflection coefficient
S	Surface area (m^2)
S_i	Surface area of component (i) (m^2)
t	Time (s)
$t_{annealing}$	Annealing time (min)
T	Absolute temperature (°K)
T_c	Crystallization temperature (°C)

T_g	Glass transition temperature
T_H	Mold upper plate temperature (°C)
T_L	Mold lower plate temperature (°C)
T_m	Melting temperature (°C)
T_{60}	Reverberation time (s)
V	Volume (m^3)
V_c	Volume Inaccessible by helium gas
V_g	Geometric volume
W_a	Energy of absorbed sound waves
W_i	Energy of incident sound waves
W_r	Energy of reflected sound waves
W_s	Energy of structure-borne sound waves
W_t	Energy of transmitted sound waves
x	Distance from the surface of the material (m)
X	Intensity of transmitted X-ray
X_0	Intensity of incident X-ray
Z	Acoustic impedance (MKS rayl)
$Z`$	Real part of acoustic impedance
$Z``$	Imaginary part of acoustic impedance
Z_c	Characteristic impedance (MKS rayl)
Z_s	Surface impedance (MKS rayl)
$\bar{\alpha}$	Average sound absorption coefficient
α_i	Sound absorption coefficient of component (*i*)
α_∞	tortuosity
β	X-ray attenuation coefficient
β_i	X-ray attenuation coefficient of material (i)
γ	Surface tension
ε	Matching ratio
η_0	Zero shear viscosity (Pa.s)

θ	Wetting angle of the polymer-additive gas interface
λ	Wavelength of sound wave
μ	Proportional factor associated with sound dissipation in homogeneous material
υ	Acoustic particle velocity
ρ_0	Air density (kg/m^3)
σ	Air flow resistivity (rayl/m)
ϕ	Porosity
ω	Angular frequency (rad/s)

List of Abbreviations

ABS	Acrylonitrile butadiene styrene trepolymer
ADC	Azodicarbonamide
ASTM	American society for testing and materials
CBAs	Chemical blowing agents
CFCs	Chlorofluorocarbons
DOP	Dioctyl phthalate
DSC	Differential scanning calorimetry
EVA	Ethylene vinyl acetate copolymer
FGMs	Functionally graded materials
GWP	Global warming potential
HCFCs	Hydrofluorochlorocarbons
HS	Homogeneous sample made from microthene MU7300 foam sample
LS	Foam sample prepared with the 500-850μm salt size
LVR	Linear viscoelastic region
Micro-CT	X-ray micro-computed tomography
MMP	Microperforated panels
MS	Foam sample prepared with the 250-500μm salt size
OBSH	4,4' oxybis(benzene sulfonyl hydrazine)
ODP	Ozone depletion potential
PBAs	Physical blowing agents
PC	Polycarbonate
PCL	Poly(ε-caprolactone)
PE	Polyethylene
PEG	polyethylene glycol
PET	Polyethylene terephthalate
PLA	Polylactic acid

PMMA	Polymethyl methacrylate
PP	Polypropylene
PS	Polystyrene
PU	Polyurethane foam
PVC	Polyvinyl chloride
SEM	Scanning electron microscope
SS	Foam sample prepared with the 106-250μm salt size
TG	Thermoplastic gelatin
TGA	Thermogravimetric analysis
VA	Vinyl acetate content
VI	LabVIEW virtual instrument

Chapter 1 Introduction

1.1 Background and Motivation

Damping of low frequency noise constitutes a big challenge to automotive, transportation and building industries. Despite the fact that homogeneous foams exhibit excellent performance in damping high frequency noise (i.e. above 1000Hz), they fail to absorb low frequency noise at reasonable thickness; while a material thickness of 8.5cm is sufficient to damp the 1000Hz noise, a thickness of 85cm is required to damp the 100Hz noise. Such thickness excludes large volume of the space to be acoustically treated, besides it imposes constraints on other non-acoustic treatments. Techniques available in noise engineering field, such as multi-layered structures, resonating devices, micro-perforated panels, and corrugated-surface absorbers experience some shortcomings which limit their applicability. These shortcomings include increased material thickness, high cost, delamination issues, narrow absorption band, and difficulty of fabrication and fixation of acoustic material.

Heterogeneous porous foams, such as bimodal porous foams and graded porous foams, are advantageous over homogeneous foams in many aspects. The unique cellular structure of these material results in their optimum performance in certain applications due to customization of two or more contradicting properties. This customization of opposing properties cannot be achieved in homogeneous foams. For instance, bimodal porous foams, which consist of a combination of small cells and large cells, are excellent candidates for application in mass/heat exchange and tissue implantation. The small cells are characterized by large surface area, and are therefore important for heat/mass transfer operations, and living cells implantation. While the role of large cells is to provide easy and fast access paths to the material helping accelerate diffusion processes, and minimize the pressure drop developed across it. Graded porous foams, on the other hand, are characterized by a continuous change of porosity across the material. These materials have higher stiffness/mass and strength/mass ratios compared to homogeneous foams.

Moreover, they are superior to laminated composites as they do not experience delamination and stress jump issues that occur at the interfaces of laminated composites.

Interestingly, heterogeneous open cell foams have been found to be effective in dissipating low frequency noise. The unique cellular structure of such materials increases their acoustic efficiency, which leads to reducing the thickness of the acoustic treatment, and broadening the sound absorption band. Additionally, they do not experience delamination, or fixation/fabrication issues present in other acoustic treatments.

Some methods and concepts have been proposed in literature to produce heterogeneous polymer foams. However, there are still some limitations associated with each of these methods. For example, the mechanical perforation method used to produce double porosity foams requires additional post processing step which increases the production cost, and the produced foams experience high sound transmission. Moreover, the particulate leaching, and batch gas foaming methods used to produce double porosity foams are not suitable for large scale production because of long processing times, small sample sizes, and poor structure integrity of the produced foams. On the other hand, graded porosity foams fabricated by proposed methods are either non-recyclable, or have decreased porosity/closed cell structure. Such foams are not appropriate for sound absorption applications, and their use is not favored for environmental considerations.

1.2 Thesis Objectives

The purpose of this work is to develop heterogeneous thermoplastic foams with either double porosity or with graded porosity by using processes that can potentially be scaled up for mass production. The developed heterogeneous thermoplastic foams are intended for the purpose of improving the absorption of the low frequency noise, which constitutes a prevailing challenge in noise engineering field. To this end, three different strategies for developing heterogeneous thermoplastic foams have been proposed and examined in the thesis. These stragegies include the following:

- foaming of a low melt strength polymer in presence of additives such as sodium bicarbonate and wollastonite.
- foaming a blend consisting of a base foamable polymer and another low melt strength polymer.
- heterogeneous pre-foaming in compression molding under an applied temperature gradient, followed by oven expansion of cells in an oven.

1.3 Methodology

To develop double porosity open cell thermoplastic foams, two different approaches were applied. The first approach was based on the foaming of a low melt strength polymer in presence of some additives, such as sodium bicarbonate and wollastonite. The inherent low melt strength of the polymer causes cell coalescence during foaming forming foams with a majority of large cells. Addition of the endothermic chemical blowing agent 'sodium bicarbonate', and/or the nucleating agent 'wollastonite' is intended to increase the population of small cells forming a combination of small cells and large cells. In the second approach, a foamable EVA grade, capable of producing uniform fine cellular structure, was blended with another low melt strength polymer, such as PEO and low melt strength EVA grade. Upon foaming, the domains of the low melt strength polymer experience cell coalescence leading to formation of dispersed large cells throughout the developed fine cellular structure of the base polymer.

In the third approach, thermoplastic foams with graded porosity were developed by applying different temperature gradients during compression molding of samples to induce heterogeneous prefoaming as a first step. These pre-foamed samples were further expanded in a heating oven to obtain the final expansion ratio, and to achieve high porosity.

1.4 Thesis Main Contributions

The main contributions of the work can be summarized in the following:

- Development of three different strategies for fabrication of thermoplastic foams with double porosity or graded porosity.
- Development of open celled bimodal and graded porous thermoplastic foams with open cell content of 88%.
- Improving reduction of noise over the low frequency range, more specifically from 177 up to 1000Hz.
- Using X-ray computed tomography technique to extract all cellular structure characteristics of thermoplastic foams.
- Fabrication of open celled highly porous thermoplastic foams by a simple foaming process that does not include crosslinking, mechanical crushing, or any of the approaches used to increase the open cell content.

1.5 Thesis Outline

The thesis is divided into eight chapters. Chapter one provides the motivation of this work, its main objectives, and the technical approaches proposed to achieve the intended goals. The main contributions of the study, and thesis organization are also included in this chapter. Chapter two reviews the fundamental basics relevant to thermoplastic foams including their classifications, foaming mechanism, materials used for foam production, and foaming processes. In addition, the chapter discusses some important topics in noise control engineering, in particular sound absorption terminologies, and the low frequency problem. It also discusses previous studies that have been undertaken to produce double porosity, and graded porosity polymer foams. Finally the chapter concludes with a summary of the literature review, highlighting the shortcomings associated with the existing manufacturing methods, and research need.

Chapter three provides an overview of the experimental methods used in this study to develop and characterize heterogeneous thermoplastic foams. This includes listing the properties of all materials used in the study, equipment that were used to produce foams, in

addition to describing the methods, instruments that were utilized to characterize the cellular structure, and acoustic performance of the developed foams.

Chapter four investigates the effect of cell size on sound absorption coefficient over the measurement frequency range which extends from 100 to 2000Hz. The chapter also includes a study on the feasibility of using some noise engineering techniques, such as air gap and/or impervious facing to improve sound absorption performance of homogeneous thermoplastic foams.

Chapter five summarizes the experimental work conducted on producing bimodal porous foam by foaming of a low melt strength polymer in presence of the endothermic chemical blowing agent ‘sodium bicarbonate’ and nucleating agent ‘wollastonite’.

Chapter six describes the approach of producing bimodal porous foams by blending a foamable base polymer with another low melt strength polymer. Factors such as polymer type and polymer concentration were examined and discussed throughout the chapter.

Chapter seven summarizes the experimental work conducted to produce graded porous foams by combining heterogeneous prefoaming with oven expansion. The effect of factors such as applied temperature gradient and molding time on the developed cellular structure was examined in detail.

Finally, chapter eight serves as a summary of the work done. The major contributions of this thesis, as well as a list of recommendations for future research are reiterated in this chapter.

Chapter 2 Literature Review and Theoretical Background

2.1 Sound Absorption Fundamentals

2.1.1 Introduction

Noise is defined as unpleasant, but not necessarily loud sound that causes disturbance and makes individuals feel uncomfortable. Noise like other types of pollution is an inseparable byproduct of human activities. Noise issues arise in many live cases including, but not limited to, means of transportation such as automobiles, buses, trains, and airplanes, residential areas near highways and airports, plants, and different types of auditoria (e.g. lecture rooms, concert halls, conference rooms, opera houses, movie theaters, worship places, and restaurants halls. Acoustic treatments are critical for such cases not only to improve the quality of life, which is achieved by providing tranquil and friendly acoustic surroundings, but most importantly to protect health. It was reported in many studies that noise has a negative impact on one's health, which in turn adversely affects behavior, and reduces productivity. The impact of noise can vary from just mild physiological effects including stress, annoyance, frequent anger, suppressed emotions, sleep disorder, inability to focus, and communication problems to harsh biological effects such as fatigue, headache, backache, digestive disorders, asthma, hearing loss, and cardiovascular disorders [1]. The reaction paths of sound on human body are shown schematically in Figure 2-1.

2.1.2 Sound absorption coefficient

When an incident plane sound wave with power (W_i) impinges upon a porous material having thickness *(d)* and backed with a rigid surface (as shown schematically in Figure 2-2), some of its power is reflected back (W_r), a second part is transmitted as air-borne noise behind the solid surface (W_t), a third part is converted into vibrations throughout the solid surface (W_s), and the remaining portion is dissipated as heat (W_a) within the porous material due to friction of air with material tiny cellular network. The

incident power, according to the conservation of energy principle, is therefore equivalent to the sum of all these shares i.e.:

$$W_i = W_r + W_t + W_s + W_a \tag{2.1}$$

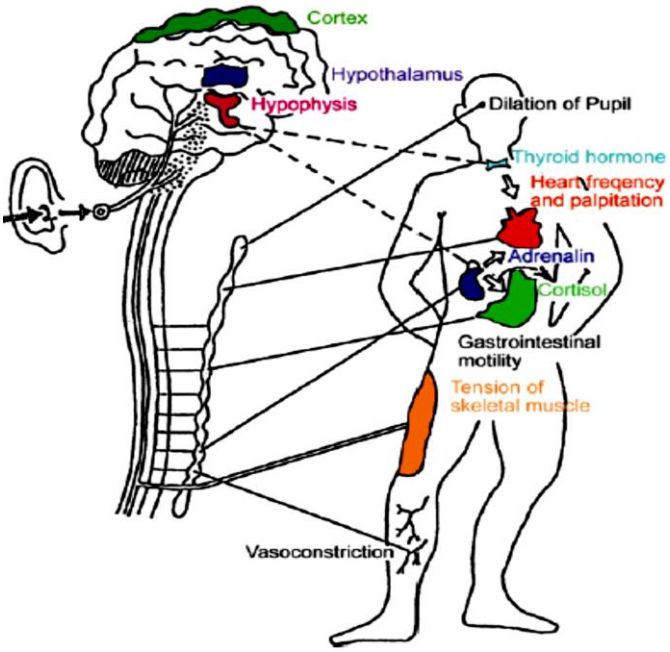

Figure 2-1: Extra aural reaction lines [2]

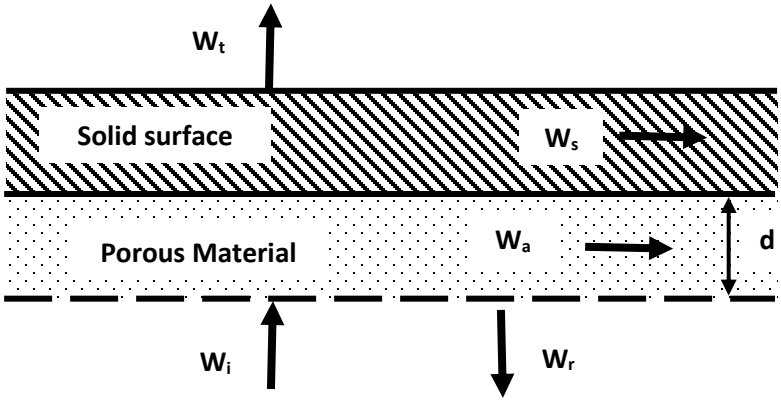

Figure 2-2: Possible paths of sound wave power upon impinging a porous material

Sound absorption coefficient (α) is used as a performance index to evaluate the efficiency of sound absorbing materials such as fibers and open cell polymer foams. It represents the sound energy fraction, or alternatively the power fraction, that is dampened,

and not reflected back to the surrounding when sound waves impinge on the surface of the material. For normal incidence, it is expressed mathematically as [3]:

$$\alpha(\omega) = \frac{W_t + W_s + W_a}{W_i} = \frac{W_i - W_r}{W_i} = 1 - \frac{W_r}{W_i} = 1 - \frac{I_r}{I_i} \tag{2.2}$$

The power of both incident and reflected sound waves in the above equation were expressed in terms of the corresponding sound intensities (I_i and I_r) as the cross-sectional area is the same in both cases. Also, it is obvious that absorption coefficient is a scalar quantity, as it is a power ratio, which means that sound absorption coefficient has no information about phase.

2.1.3 Sound reflection coefficient

Sound reflection coefficient (R) is an alternative way of evaluating the performance of sound absorbing materials. It is defined as the ratio of the pressure amplitude of the reflected sound wave to that of the incident sound wave for a plane sound wave [3]:

$$R(\omega) = \frac{p_r}{p_i} \Rightarrow p_r = R(\omega)\, p_i \tag{2.3}$$

where p_r is the pressure of reflected sound wave, p_i is the pressure of incident sound wave, and ω is the angular frequency. Unlike sound absorption coefficient, R is a complex quantity with a phase term expressing the phase lag between these two pressure waves. For a plane sound wave, sound pressure and sound intensity are correlated according to the following equation [3]:

$$I_i = \frac{p_i^2}{\rho_0 c_0} \; and \; I_r = \frac{p_r^2}{\rho_0 c_0} = \frac{|R|^2 \, p_i^2}{\rho_0 c_0} \tag{2.4}$$

where ρ_0 is the air density, and c_0 is the sound speed in air. By substituting for I_r and I_i from Equation 2.4 into Equation 2.3, we obtain the correlation between α and R:

$$\alpha(\omega) = 1 - \frac{|R|^2 \, p_i^2 / \rho_0 c_0}{p_i^2 / \rho_0 c_0} \Rightarrow \alpha(\omega) = 1 - |R|^2 \tag{2.5}$$

2.1.4 Acoustic impedance

Sound is reflected when it transfers from one medium to another owing to the difference in the acoustic impedance between these two media. Medium specific impedance is defined as the ratio of the acoustic pressure to the corresponding particle velocity within the medium. Mathematically, acoustic impedance is expressed as [3]:

$$Z(x,t) = \frac{p(x,t)}{v(x,t)} = Z' + jZ'' \tag{2.6}$$

where Z is the acoustic impedance, p and v are the acoustic pressure and the medium particle velocity, respectively. In general, acoustic impedance is a complex quantity with a real component (Z') expressing the magnitude of resistance that sound waves experience through the medium, and an imaginary component (Z'') expressing the reactance or the phase lag between the acoustic pressure and the medium particle velocity. For progressive plane sound waves in the air, the impedance is purely real (resistive), since both acoustic pressure and particle velocity are in phase. The acoustic impedance of air is given by the following equation:

$$Z_c = \rho_0 c_0 \tag{2.7}$$

where Z_c is the characteristic impedance. At 20 ^{o}C and 10^5 Pa, $\rho_0 = 1.21\ kg/m^3$, $c_0 = 344 m/s$, and $Z_c = \rho_0 c_0 = 1.21 \times 344 = 416.24\ Pa.s.m^{-1} (MKS\ rayl)$. If the impedance is being measured at the interface between two media, then it is called surface impedance (Z_s). The impedance at the surface of any sound absorbing material depends primarily on the material specific impedance, which is totally governed by the material bulk properties such as porosity, flow resistivity, tortuosity, thermal characteristic length, and viscous characteristic length. Surface impedance also depends on material thickness, mounting condition, and incidence angle of sound waves.

The correlation between surface impedance and sound reflection coefficient can be derived by considering a plane sound wave propagating in the positive *x*-direction towards the surface of a sound absorbing material as shown schematically in Figure 2-3. Upon impingement, part of the sound energy is reflected in the reverse direction. The reflected sound wave interferes with the original incident wave, forming a standing wave. The total pressure of this standing wave is calculated by applying the superposition principle [3]:

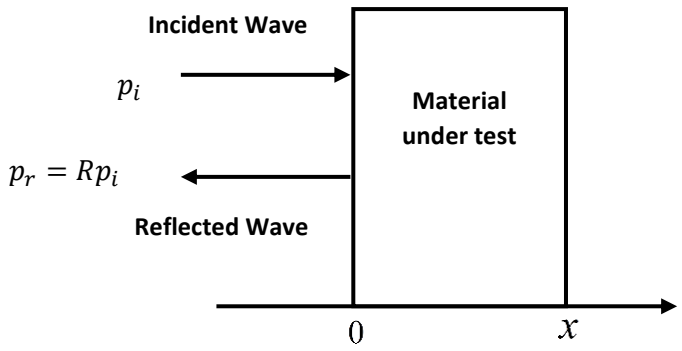

Figure 2-3: Reflection of the incident pressure wave at the material surface

$$p(x,t) = p_i + p_r = P_i e^{j(\omega t - \bar{k}x)} + RP_i e^{j(\omega t - \bar{k}x)} \tag{2.8}$$

Where p_i is the pressure of the incident sound wave, p_r is the pressure of the reflected sound wave, P_i is the pressure amplitude of the incident sound wave, t is the time, x is the distance from the material surface, ω is the angular frequency ($= 2\pi f$), $\bar{k}$ is the wavenumber ($= \omega/c_0 = 2\pi/\lambda$), c_0 is the speed of sound in air, f and λ are the sound frequency and wavelength, respectively. The particle velocity is given by [3]:

$$v(x) = \frac{p(x)}{Z_c} = \frac{P_i}{Z_c} e^{j(\omega t - \bar{k}x)} - \frac{RP_i}{Z_c} e^{j(\omega t + \bar{k}x)} \tag{2.9}$$

At the surface of the material ($x = 0$), we have:

$$p(0) = (1+R) P_i e^{(j\omega t)} \tag{2.10}$$

$$v(0) = (1-R)\frac{P_i}{Z_c}e^{(j\omega t)} \tag{2.11}$$

And the corresponding surface impedance for this case equals:

$$Z_s = \frac{p(0)}{v(0)} = \frac{(1+R)P_i e^{(j\omega t)}}{(1-R)\frac{P_i}{Z_c}e^{(j\omega t)}} = Z_c\frac{1+R}{1-R} \tag{2.12}$$

Rearranging the above equation to obtain sound reflection coefficient in terms of material surface impedance:

$$R(\omega) = \frac{Z_s - Z_c}{Z_s + Z_c} \tag{2.13}$$

Substituting for R from Equation 2.13 into Equation 2.5, and expanding the Z_s term:

$$\alpha(\omega) = 1 - |R|^2 = \frac{4Z'_s Z_c}{(Z'_s + Z_c)^2 + Z''^2_s} \tag{2.14}$$

Equation 2.14 is called "the matching law", and it shows the influence of the acoustic impedance at the material surface on sound reflection. Apparently, absorption coefficient increases as the reactance term (Z_s'') approaches zero, and α takes the value of unity only in a unique single case when the surface impedance matches air impedance (i.e. only when $Z_s = Z_s' = Z_c$). For the extreme case when $\alpha = 0.01$ (i.e. hard wall), a standing wave is formed, and a sound pressure level difference of 50dB is observed. While for the other extreme case when $\alpha = 0.99$ (i.e. highly absorptive material), only progressive sound waves predominate, and a pressure level difference of only 2dB is observed [1].

2.2 Acoustic Performance of Homogeneous Passive Absorbers

For a homogeneous sound absorbing material that is characterized by porosity (ϕ), static air flow resistivity (σ), and tortuosity (α_∞), the surface impedance (Z_s) can be calculated by using the following equation [4]:

$$Z_s = Z_c \frac{\sqrt{\alpha_\infty}}{\phi} \sqrt{1 - j \frac{\phi\sigma}{2\pi f \rho_0 \alpha_\infty}} \tag{2.15}$$

If air flow resistivity is negligibly small, which is met by utilizing sound absorbing material with a very large thickness, Equation 2.15 is then shortened to:

$$\sigma \ll 2\pi f \rho_0 \rightarrow Z_s = Z_c \frac{\sqrt{\alpha_\infty}}{\phi}; \alpha = \frac{4}{2 + \frac{\phi}{\sqrt{\alpha_\infty}} + \frac{\sqrt{\alpha_\infty}}{\phi}} \tag{2.16}$$

And since $\phi \approx \alpha_\infty \approx 1$ for most acoustic passive absorbers, the surface impedance (Z_s) in equation 2.16 matches air impedance and the value of sound absorption coefficient becomes unity. For the latter case, no sound reflection takes place at the material surface and a plane sound wave is dissipated exponentially with an exponent (μ) [4]:

$$\mu \sim \sqrt{\frac{\phi\alpha_\infty}{\rho_0 c_0^2}} f \tag{2.17}$$

It can be concluded from Equation 2.17 that when the frequency goes down, the exponent (μ) decreases correspondingly, which means that larger thickness of the acoustic material will be required to dampen noise as its frequency goes down. In real life, finite thickness of sound absorbing materials is commonly utilized in acoustic treatments, and in that case both air flow resistivity (σ) and material thickness (d) become influential on acoustic efficiency. Increasing the material thickness and/or increasing air flow resistivity help dissipate more sound energy by viscous losses. But, at the same time, increasing these two parameters has an adverse effect, as they tend to increase material surface impedance, which in turn causes sound reflection at the material surface. This implies that there are

optimum values for these two parameters for optimum performance. This is mathematically represented by the following equation [4]:

$$2\langle\varepsilon = (\frac{\sigma d}{\rho_0 c_0})(\frac{\phi}{\sqrt{\alpha_\infty}})\langle 6 \tag{2.18}$$

where ε is called the matching ratio, and its value has to be between 2 and 6 for optimum performance. Under the assumption that $\phi \approx \alpha_\infty \approx 1$, which is normally met in most acoustic materials, Equation 2.18 is abridged to:

$$800 < \sigma d < 2400\, Pa.s.m^{-1}\left(MKS\, rayl\right) \tag{2.19}$$

The dependence of the matching ratio on the material flow resistivity for different thicknesses of homogeneous passive absorber is shown in Figure 2-4. The vertical line at $\sigma > 7500\ Pa.s.m^{-2}(MKS\ rayl/m)$ represents the minimum flow resistivity value for most commercial sound absorbing materials.

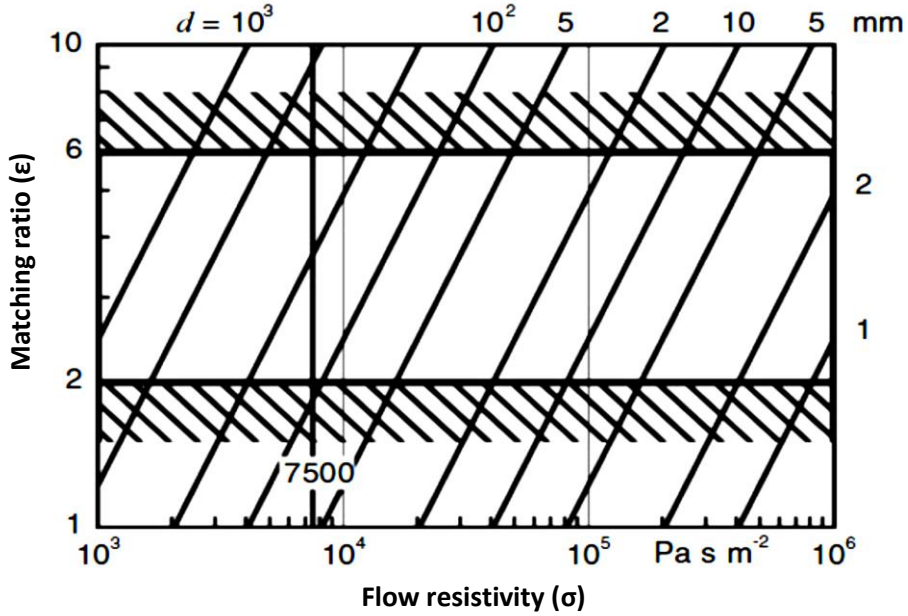

Figure 2-4: Matching ratio (ε) as function of (σ) for varying layer thickness (*d*)[4]

The design characteristics of homogeneous passive absorbers are also displayed in Figure 2-5. It is obvious from Figure 2-5(a) that it is not possible to absorb sound waves when the absorber thickness is much less than the wavelength of the incident sound wave. And to obtain sound absorption value of 0.8, the absorber thickness should be equivalent to one eights of the incident wavelength. Whilst for 90% or more sound absorption, the thickness of the acoustic treatment should be at least quarter of the incident wavelength. The underlying physics of the $\lambda/4$ rule is that sound has to meet the material at its maximum velocity for maximum sound dissipation by friction losses. This maximum velocity occurs at a distance away from the wall by $\lambda/4$. It is noteworthy that Figure 2-5(b) can be used as a benchmark, when evaluating the efficiency of a newly-developed material in sound absorption, on condition that the same thickness is utilized.

In conclusion, it is not possible to damp low frequency noise without using very large thick material. This not only excludes large volume of the space to be acoustically treated, but it also puts some constraints over other non-acoustic treatments. Even with such thickness, another issue still exists; by referring to Equation 2.19, it turns out that the air flow resistivity required to achieve optimum absorption has to be between 800 and 2400rayl/m. As said before, most passive absorbers have air flow resistivity values greater than 7500rayl/m. Technically, it is infeasible to use such loose soft material, as it does not maintain reasonable mechanical strength. As a result, it becomes more difficult for such material to be packed, and securely-protected. Also its usage is uneconomic, as they are not durable, and cannot survive for longer times.

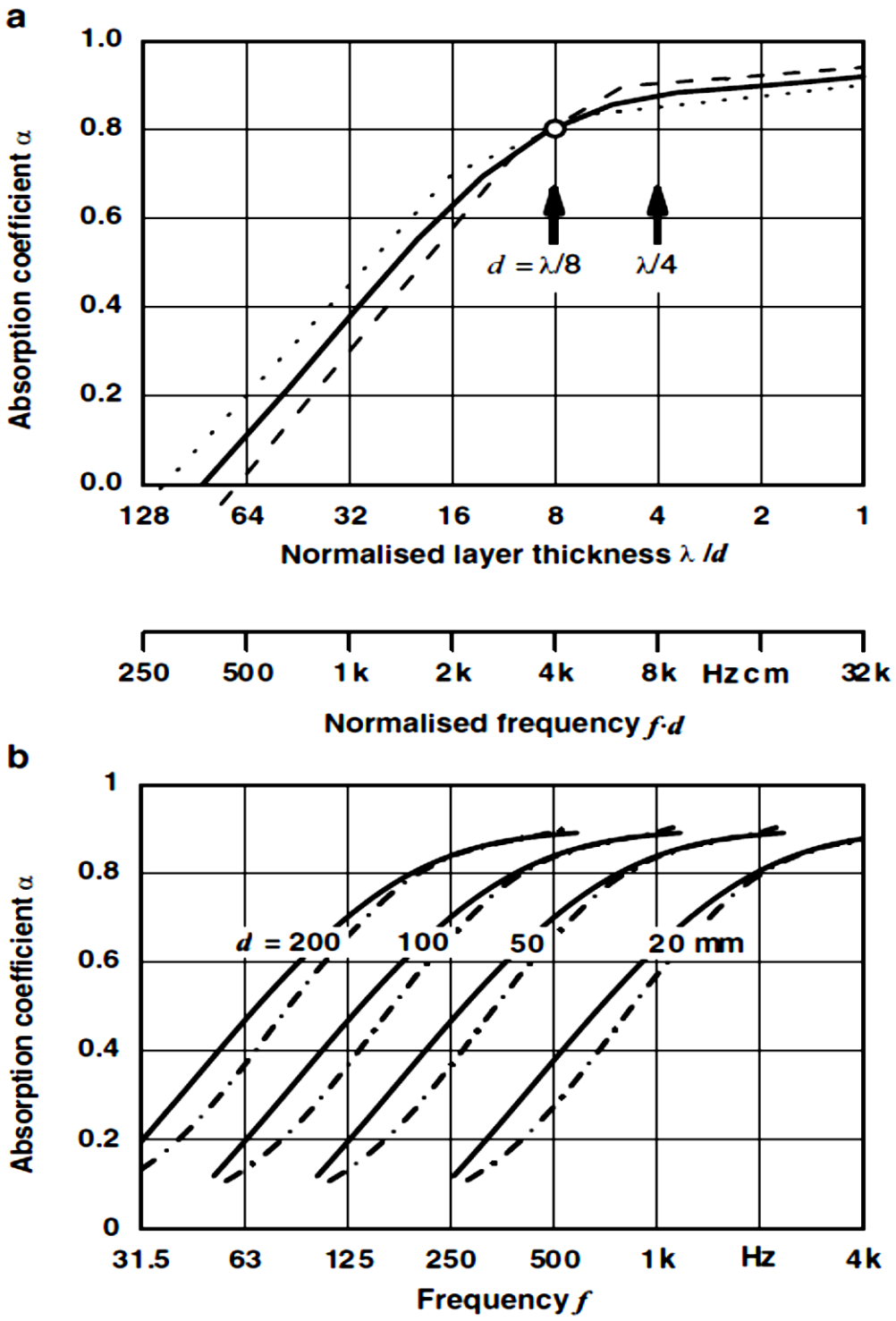

Figure 2-5: Design characteristics of porous/fibrous absorbers: (a) with optimum matching ratio $\varepsilon = 2$ (dashed line) and $\varepsilon = 6$ (dotted line); (b) for random (solid line) and normal (dashed dotted line) sound incidence [4]

2.3 The Low Frequency Problem

2.3.1 Problem background

The pressing demand to silence low frequency noise has driven many researches in the field of noise control engineering over the past two decades due to its vital importance to automotive, transportation, and building industries. The existence of these low frequencies in closed spaces such as auditoria, and transportation means produce uncomfortable noisy environment, in addition to their detrimental effect on the intelligibility of speech and clarity of played music, which subsequently causes difficulty in communication among people, and quality degradation of played music.

In closed space, low frequencies generate different types of sound fields (e.g. diffuse field and modal field). These sound fields basically depend on the dimensions, and the geometry of the closed space. The interference of such sound fields with the original sound results in degradation of speech intelligibility and music quality. The frequency range of each type of these fields is given as a function of closed space volume in Figure 2-6. The gray region in the figure is due to the uncertainty in computing the upper resonance frequency of the modal field.

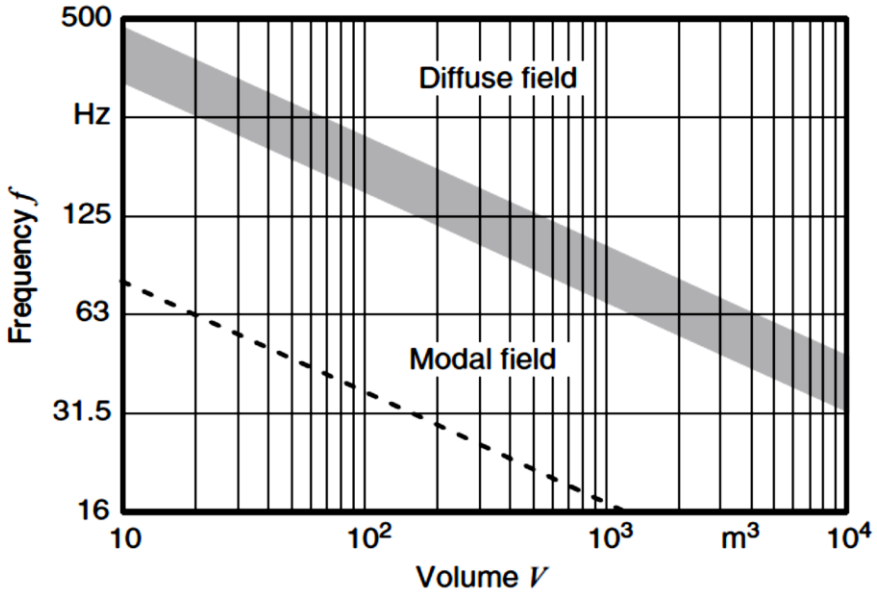

Figure 2-6: Frequency range for modal and diffuse sound field of a cubic room versus its volume [1]

In the first case, when the sound wavelength is comparable to one of dimensions of the closed space, a standing wave (i.e. modal field) is formed, and the room behaves like a cavity inducing resonance. This modal field is characterized by a sound pressure level varying from zero (at nodes) to maximum (at antinodes which normally occur at wall boundaries). This leads to uneven distribution of sound throughout the closed space, viz., sound cannot be heard at some locations, while it becomes very high at some other locations. For a cubic room with dimensions ($l_x \rangle l_y \rangle l_z$) and volume ($V$), the lowest resonance frequency is given by [4]:

$$f_l = \frac{c_o}{2\sqrt[3]{V}} \tag{2.20}$$

Below f_l, the room behaves like a pressure vessel, and only pressure perturbation occurs. The upper frequency limit of resonance is given by [4]:

$$f_u = \frac{3c_0}{\sqrt[3]{V}}; f_u = \frac{2c_0}{\sqrt[3]{V}} \tag{2.21}$$

Above f_u, the sound wavelength is very small compared to the dimensions of the room, and in that case sound waves behaves in a similar way to light rays experiencing multiple reflections at room boundaries, and forming the so-called 'diffuse field'. This diffuse field is characterized by reverberation phenomenon; the original sound is being heard along with multiple echoes that result from sound reflections. Reverberation phenomenon is pictorially illustrated in Figure 2-7.

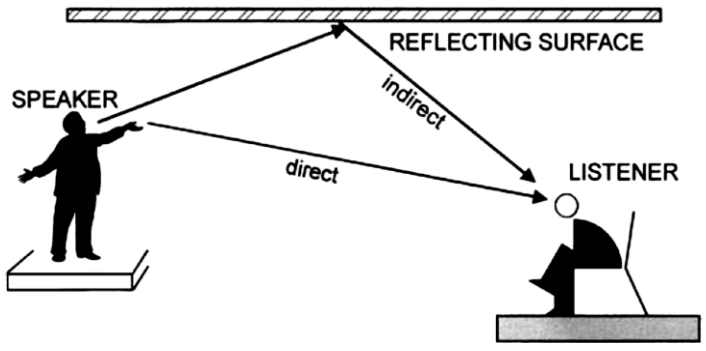

Figure 2-7: Reception of direct and indirect sound

Reverberation, if not properly controlled, adversely affects speech intelligibility and music clarity. Reverberation is quantitatively described by reverberation time (T_{60}), which is defined as the time required for a sound pressure level to drop by 60dB after the sound source has been turned off. Reverberation time is calculated by two different formulas, depending on the value of the average sound absorption coefficient of the room ($\bar{\alpha}$), which is given by [1]:

$$\bar{\alpha} = \frac{\sum \alpha_i S_i}{\sum S_i} \tag{2.22}$$

where S_i is the surface area (m^2) of a sound absorbing component inside the room, and α_i is the corresponding absorption coefficient. For the case when $\bar{\alpha}$ is less than 0.2 (i.e. the walls are mostly reflective), reverberation time can be calculated by Sabine equation [1]:

$$T_{60} = \frac{0.161V}{\sum S_i \alpha_i} \tag{2.23}$$

where V is the volume of the room (m^3). When $\bar{\alpha}$ exceeds 0.2 (i.e. the walls are more absorptive), the error in calculating reverberation time by Sabine equation exceeds 10%. And in that case, Eyeing equation is more accurate for calculating T_{60} [1]:

$$T_{60} = \frac{0.161V}{-S\ln(1-\bar{\alpha})} \tag{2.24}$$

where S is the total surface area (m^2) of all sound absorbing components within the room. It is worth mentioning that for large rooms, air remarkably contributes to sound absorption particularly at higher frequencies (i.e. above 1000Hz). As a result, reverberation time equation is modified, and a term (A_{air}) is added to the denominator of either Sabine or Eyeing equation to account for air absorption. Air absorption term (A_{air}) is given by [1]:

$$A_{air} = 4Vm \tag{2.25}$$

where V is the room volume (m^3), and m is the absorption of air.

The optimum reverberation time of an auditorium depends on its volume, plus the purpose for which it is being used. The variation of reverberation time with the volume of different types of auditoria is shown in Figure 2-8. It is obvious that reverberation time should be between 0.6 and 1.2 second in the case of speech in order not to affect its intelligibility. Reverberation times increase slightly for movie theaters, concert halls, worship places, and opera houses for the sake of adding more effects to played music or sound, making it three dimensional. Reverberation time can be controlled and tuned for an optimum value either by changing the absorption coefficient of the sound absorbing material used for acoustic treatment, or alternatively by decreasing or increasing its area.

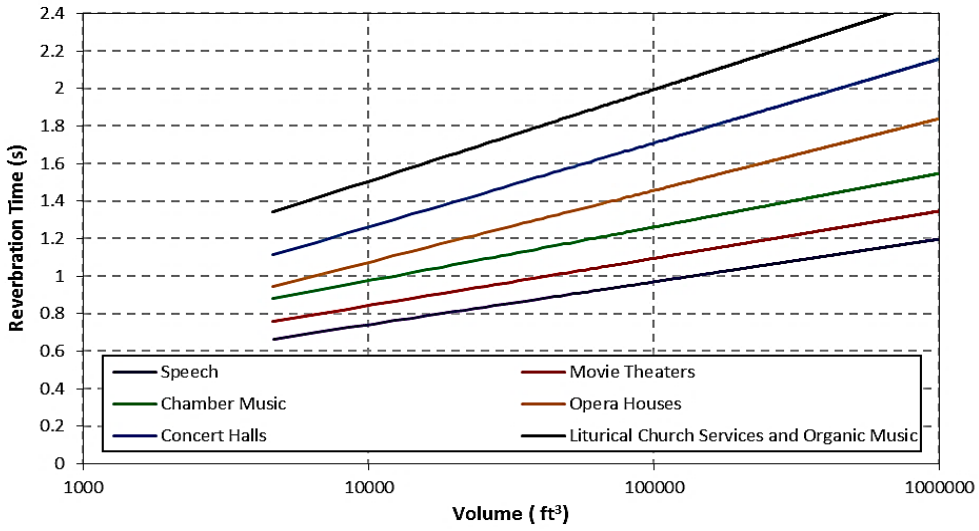

Figure 2-8: Typical reverberation times for different auditoria types [5]

2.3.2 Acoustic treatments for the low frequency noise

The efficiency of homogeneous sound absorbing materials can be enhanced by corrugating their outer surface [6, 7]. This design improves the impedance matching with air, and keeps the material away from the wall where sound velocity is zero allowing it to meet sound waves at higher velocities for maximum sound dissipation by viscous losses. The sound absorption curves of a commercial corrugated-surface absorber (Profoam^{TM}) with different thicknesses are shown in Figure 2-9. After all, fabrication and installation of corrugated-surface absorbers are more difficult than those of flat surface absorbers.

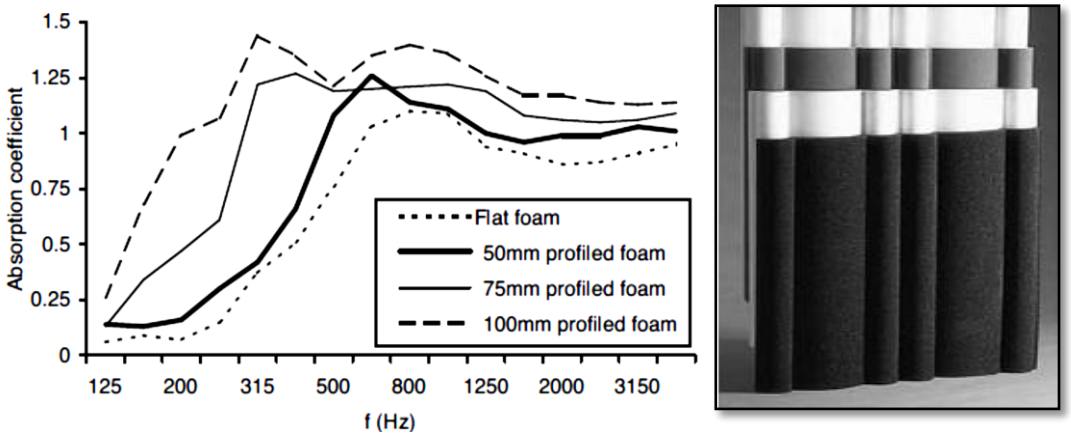

Figure 2-9: Random incidence absorption curves for a profiled acoustic foam on a rigid backing (left), sold as Profoam^{TM} (right) [8]

Laminated structures emerge as a second solution to the problem. Their design have to satisfy an acoustic impedance close to that of air at the material surface, and a gradually-increasing impedance across the successive built-up layers. The increase in impedance is important to increase sound dissipation along sound path, whereas its gradual occurrence guarantees that no or at least minimum sound reflection will take place when sound waves propagate from one layer to another [9]. Laminated structures undergo delamination, especially when they are used in a high temperature environment due to the thermal mismatch between the different constituting layers. The sound absorption curves of two different laminated structures are shown in Figure 2-10 and Figure 2-11.

Many researchers have investigated the feasibility of using resonating devices to damp low frequency noise [10]. These devices are also called bass traps, and they operate efficiently at room boundaries especially at the corners where sound pressure is maximum. Resonating devices are mass-spring systems that convert pressure perturbations at room boundaries into resonance. The induced resonance, in turn, has to be damped by means of a suitable passive absorber, such as mineral fibers or polymeric foams. Depending on design characteristics, resonating devices are divided into two main categories: Helmholtz resonators, and panel (membrane) resonators. The basic design elements of each type of these resonators are shown graphically in Figure 2-12.

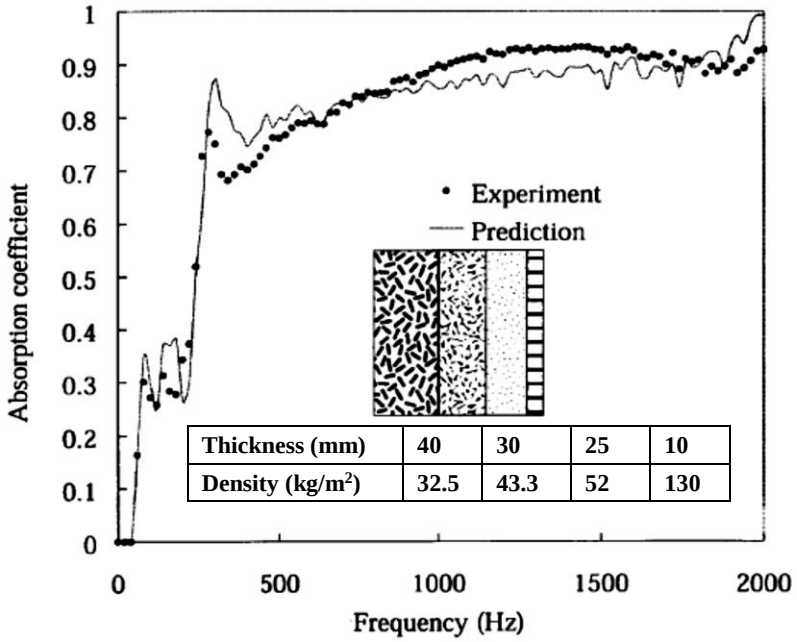

Figure 2-10: Experimental and prediction values of sound absorption coefficient for combining four porous laminated composite materials [9]

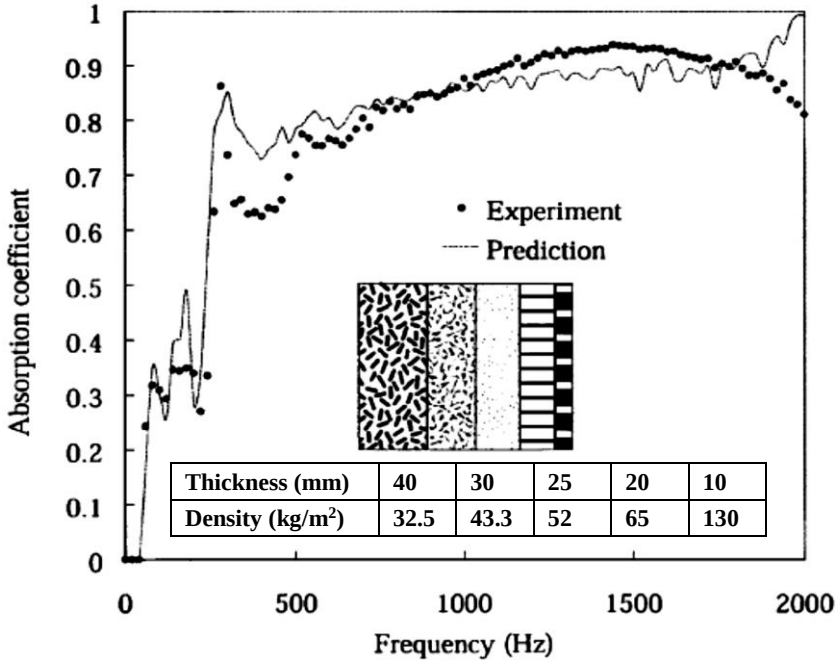

Figure 2-11: Experimental and prediction values of sound absorption coefficient for combining five porous laminated composite materials [9]

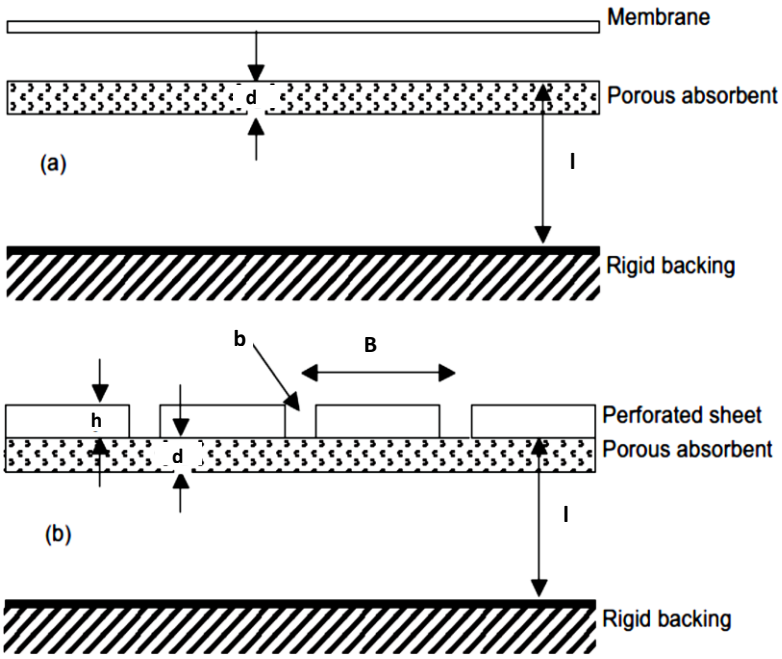

Figure 2-12: Typical constructions for (a) membrane, and (b) Helmholtz absorbers [8]

In Helmholtz resonator shown in Figure 2-12(b), the air plug within the holes of the plate, which is normally made of wood, constitutes the mass, whereas the air cavity behind the plate forms a spring. Both mass and spring stiffness can be adjusted, by designing the diameter of the holes and the depth of the air cavity to tune the device to absorb certain frequency [11]. For membrane resonator shown in Figure 2-12(a), the panel is made of pliable rubber and the membrane itself constitutes the vibrating mass, while the air confined behind the membrane acts as a spring. In both devices, a passive absorber has to be added to damp the generated resonance. The position of placing the absorber in the device is critical to device efficiency; it should be placed as near as possible to the position where maximum acoustic particle velocity occurs to achieve maximum dissipation. Based on this, passive absorbers are placed at the rear side of the perforated plate in the case of Helmholtz resonator where air has maximum particle velocity, while they are shifted a little bit away from the membrane, in the case of membrane resonator, so as not to hinder the membrane movement [12].

The effect of absorber air flow resistivity on the acoustic performance of Helmholtz resonator is illustrated in Figure 2-13, while the influence of the percentage of plate perforation on sound absorption is shown in Figure 2-14. It can be easily concluded that increasing the perforation percentage above 30% makes the plate acoustically transparent. Furthermore, increasing the damping effect, by increasing the absorber air flow resistance, broadens the absorption band, but at the cost of lowering sound absorption peak.

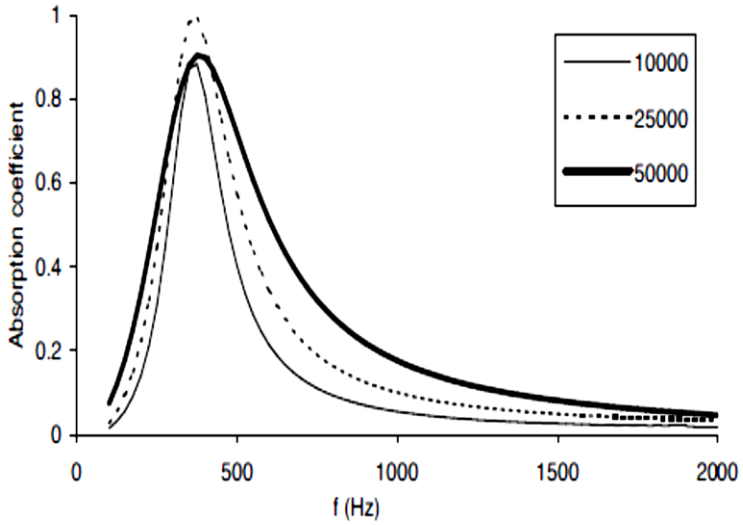

Figure 2-13: Effect of flow resistivity (rayl/m) on absorption of Helmholtz resonator [8]

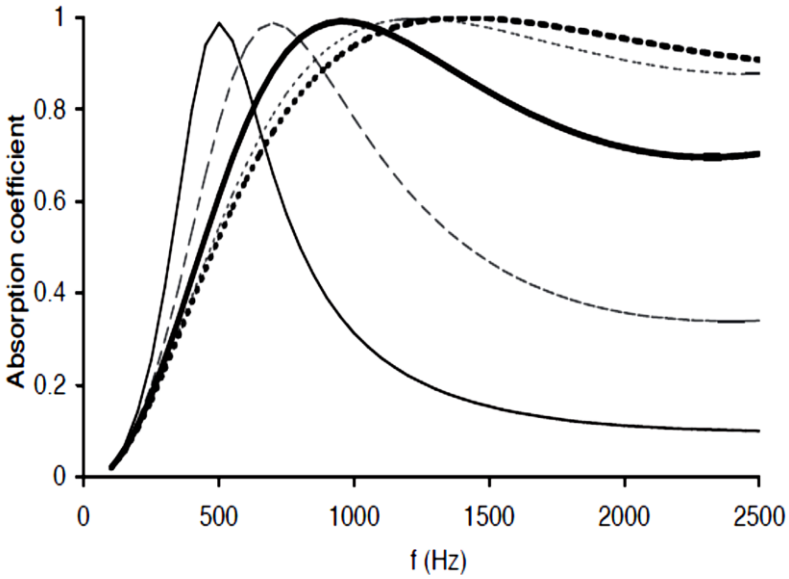

Figure 2-14: Absorption coefficient of a Helmholtz absorber showing effect of open area.
Hole radius 2.5mm; porous absorbent flow resistivity 20,000rayls/m; thickness 2.5cm; air layer thickness 2.5cm; and perforated sheet thickness 6.3mm. Open area: ——— 6%; — — — - 12.5%; ····· 25%; --------- 50%, ▬▬▬ 100% [8].

Micro-perforated panels (MMP) have also been reported in literature as new, simple, and cost-effective solution to the low frequency problem [13-16]. Micro-perforated panels are a special category of bass traps, and their development was based upon the pioneering work of Maa [17-19]. The panels are typically made of transparent polycarbonate polymer which is perforated in a certain pattern. The diameter of the holes should be close to the thickness of the viscous boundary layer to generate frictional losses. Also, the sheet thickness should be close to the diameter of the holes to maximize sound dissipation. Sheets with thicknesses between 0.1 and 0.2mm are normally used in designs. The acoustic performance of these devices can be increased by increasing the perforation density [19, 20]. The effect of different design parameters on sound absorption of micro-perforated panel is shown in Figure 2-15.

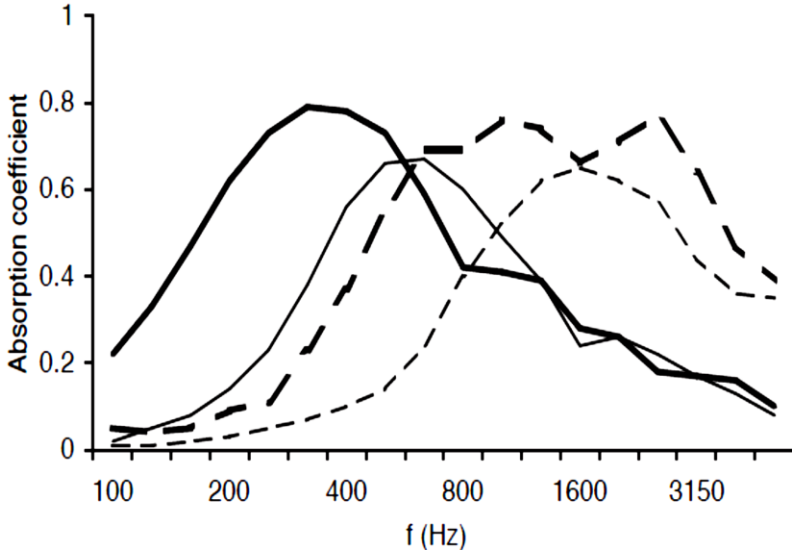

Figure 2-15: Measured random incidence absorption coefficient for four micro-perforated devices [8]
1mm sheet, 200mm backing depth, 0.5mm holes spaced at 5mm;
1mm sheet, 50mm backing depth, 0.5mm holes spaced at 5mm;
Two 0.1mm sheet, 50mm backing depth, 0.2mm holes spaced at 2mm; and
0.1mm sheet, 50mm backing depth, 0.2mm holes spaced at 2mm

Both resonating devices and micro-perforated panels experience narrow absorption band. And to extend their absorption bands, compound devices, which is an assembly of more than one device connected in series, have to be utilized. An example of such approach is shown in Figure 2-16. These compound designs increase the thickness, and the cost of the acoustic treatment.

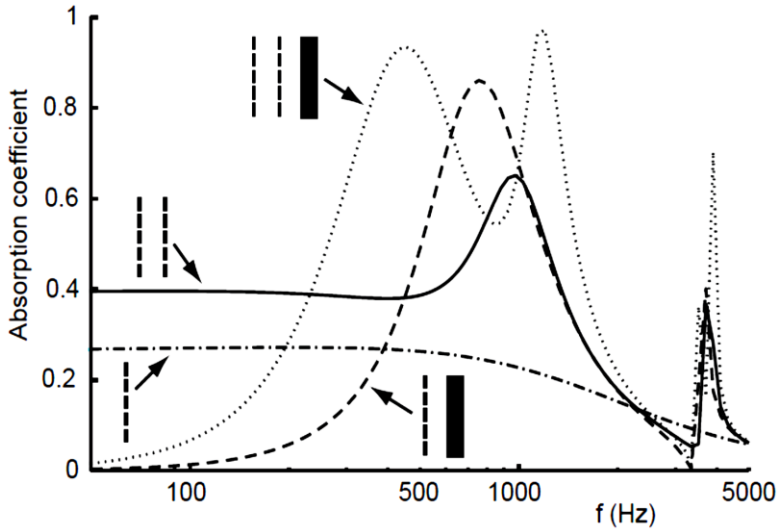

Figure 2-16: Predicted absorption coefficient for various micro-perforated devices [8]

- single micro-perforated sheet in free space;
- single micro-perforated sheet in front of rigid backing;
- double micro-perforated sheet in front of rigid backing; and
- double micro-perforated sheet in free space

Currently, heterogeneous porous foams, such as bimodal porosity and graded porosity foams, manifested themselves as an efficient candidate for tackling the problem of low frequency noise. Double porosity foams dissipate more sound energy by pressure diffusion mechanism. Double porosity materials were prepared by mechanically perforating (i.e. needle punching) microporous substrates with holes in the range of centimeters. The acoustic performance of these materials was also studied experimentally and theoretically by many authors [21-28].

Sgard et al. [26] studied the effect of different design parameters on the acoustic performance of meso-perforated fibrous materials. They concluded that the porous substrate should possess high porosity and high air flow resistivity to enhance absorption of low frequency noise. Also, the percentage of perforated area should be low, and the holes should be large in size. Comparison between sound absorption behavior of a double porosity fibrous material and that of a homogeneous material is displayed in Figure 2-17. Interestingly, the acoustic performance of these materials when coupled with impervious facing is higher than that of single porosity materials as shown in Figure 2-18.

The approach of mechanical perforation is more expensive as it requires additional post processing step. Moreover, the formation of straightforward channels across the porous substrate increases its sound transmission. The latter disadvantage makes the material unsuitable to be used as separating panels between adjacent compartments.

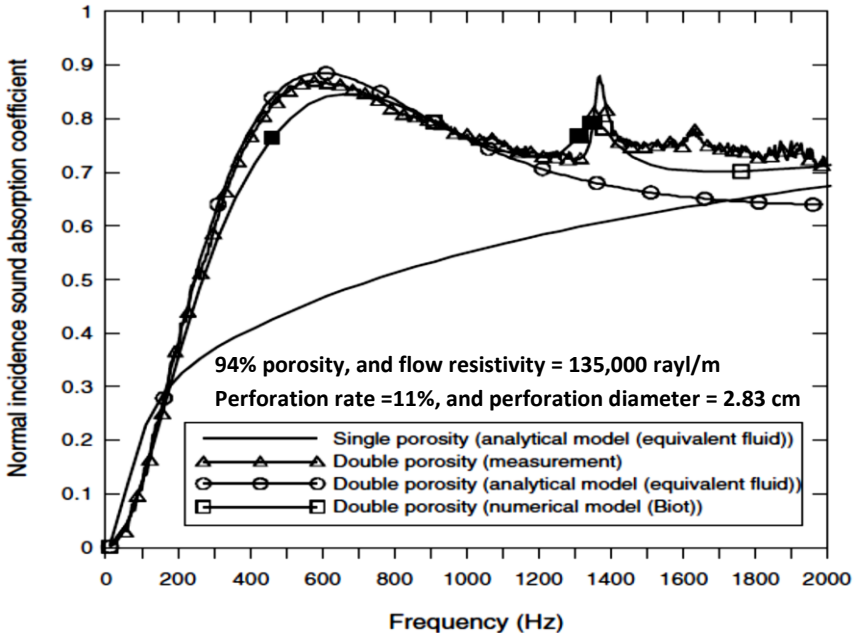

Figure 2-17: Sound absorption coefficient of 5.75 cm thick rock wool [26]

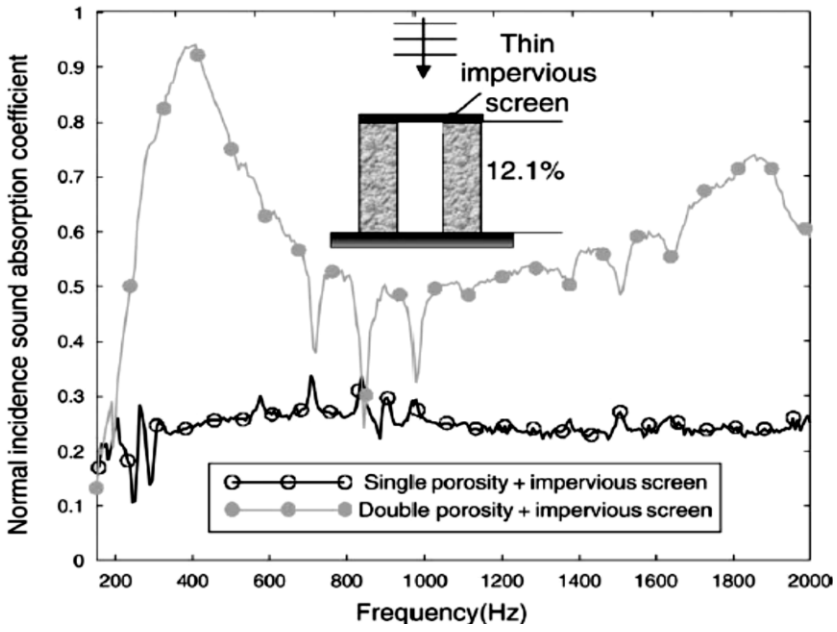

Figure 2-18: Effect of an impervious screen glued on a double porosity material [26]

Mosanenzadeh et al. [29] produced bimodal porous bio-foams by combining particulate leaching with compression molding method. They studied the effect of the developed bimodal cellular structure on sound absorption coefficient. The approach shown schematically in Figure 2-19 is based upon the hypothesis that leaching of two different types of particulate would generate cells with two different size domains. In their experiments, they mixed the base polymer, PLA, with salt having particle size between 250-500µm, and the water-leachable polymer, PEG, in weight ratios given in Table 2-1. They found that the salt was mainly responsible for both the average cell size, which was around 350µm, and the developed porosity, which ranged between 81.74% and 88.06%.

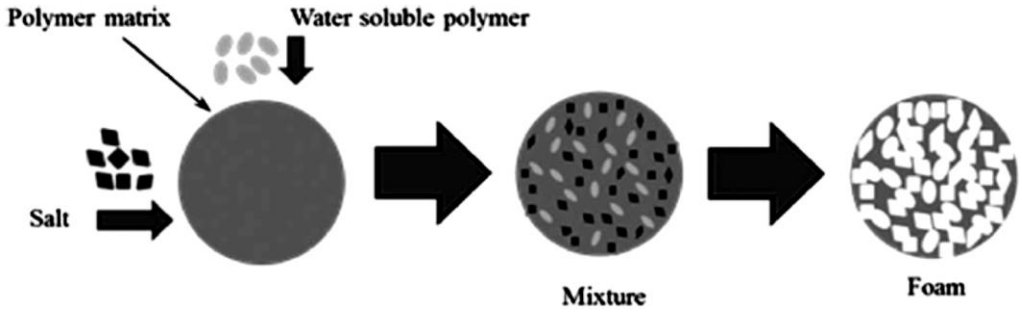

Figure 2-19: Schematic of particulate-leaching technique [29]

Table 2-1: Composition (%wt.) of foams with 10% and15% PLA [29]

Material composition (%wt.)								
	10% PLA				**15% PLA**			
PEG	0%	1%	2%	3%	0%	1.5%	3%	4.5%
Salt	90%	89%	88%	87%	85%	83.5%	82%	80.5%

They also found that leaching PEG introduced micro-cracks into foam cellular structure. Increasing the concentration of PEG did not change porosity, as indicated in Figure 2-20(a). However the air flow resistivity decreased when increasing the PEG content as shown in Figure 2-20(b). Sound absorption curves of the developed samples are shown in Figure 2-21. Increasing the concentration of PEG shifted the frequency of maximum absorption to higher values, as shown in and Figure 2-22(a). Whereas, the average absorption coefficient remained almost the same for all samples as shown in Figure 2-22(b).

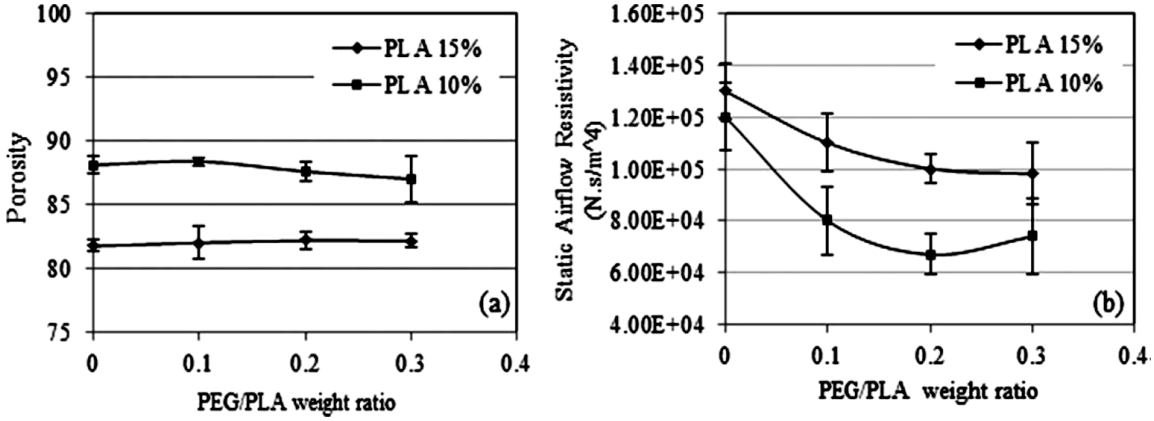

Figure 2-20 (a) Open porosity and (b) static airflow resistivity results for PLA foams with different PEG to PLA weight ratios [29]

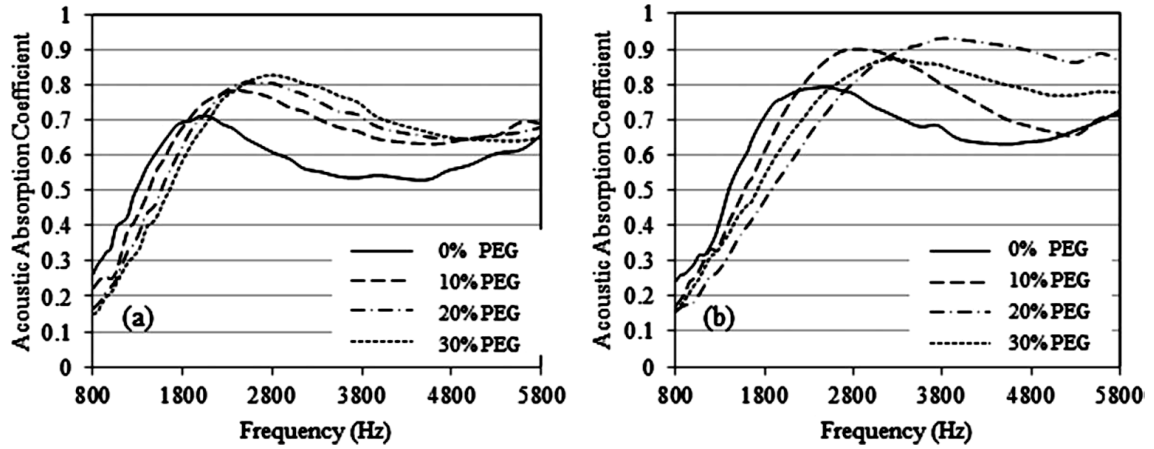

Figure 2-21: Sound absorption coefficient vs. frequency for foams with (a) 15% PLA and (b) 10% PLA.[29]

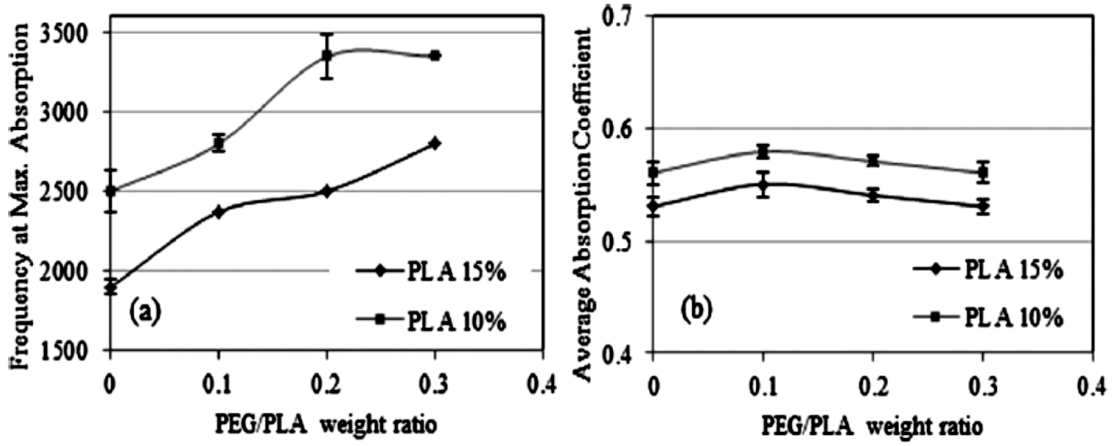

Figure 2-22: (a) Frequency at maximum absorption coefficient and (b) average absorption coefficient of PLA foams with different PEG to PLA weight ratios [29]

The previous approach has some limitations. For example, it used the particulate leaching method which is not convenient for large scale production as it takes very long time to leach the salt. Also the produced foams do not maintain structure integrity and experience crumbling. Last, the work tested the acoustic performance of the produced foams at frequencies larger than 800Hz; there is no information about the performance of these material over the low frequency range.

Graded porous polymer foams are also promising in the field of noise control engineering. Mahasaranon et al. [30] investigated the effect of graded porosity in PU foams on its sound absorption performance. Their findings are displayed in Figure 2-24. It was found that continuous stratification of porosity, achieving 5-6 fold variation in flow resistivity across the material, as shown in Figure 2-23, enhanced sound absorption over the low-mid frequency range by 10-20% compared with the non-stratified sample. They also found that the absorption coefficient measured at the sample front surface was higher than that measured at the sample rear surface by 20-30%. The difference in absorption coefficient between the front and the rear surface manifested the presence of graded porosity. The reduction in flow resistivity at the front surface minimized sound reflection, and allowed sound waves to access the foam easily, whereas the gradual increase in flow resistivity enhanced sound dissipation within the material.

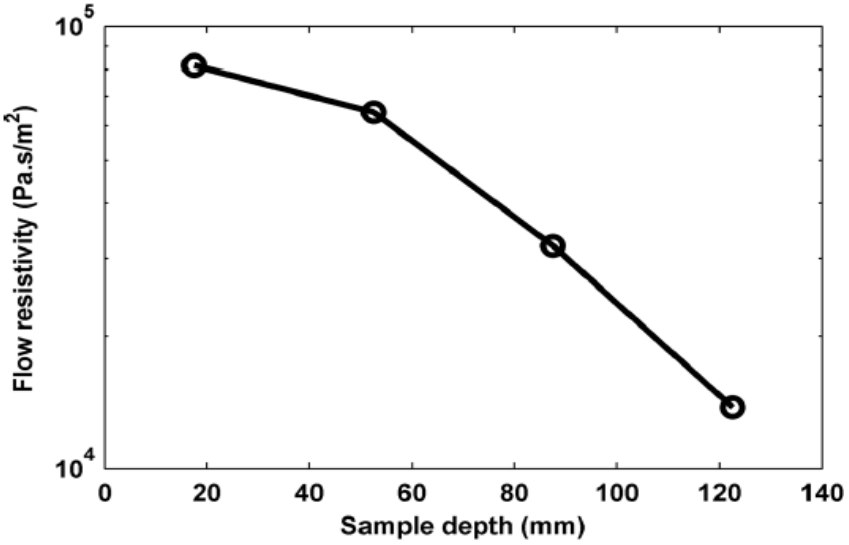

Figure 2-23: The dependence of the flow resistivity on the sample depth [30]

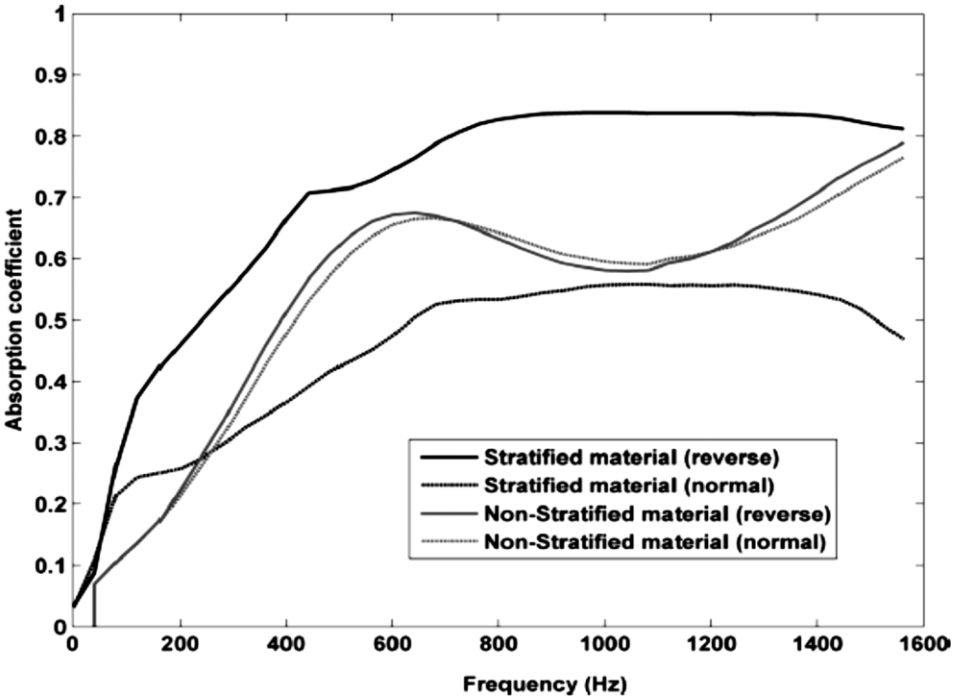

Figure 2-24: Comparison graph of stratified material with non-stratified material in normal and reverse orientation [30]

The only limitation associated with the previous work is the use of PU foam, which is not recyclable. Most researches nowadays focus on manufacture of biodegradable and recyclable materials for environmental considerations. Non-recyclable polymer foams are therefore not favored for use. Additionally, the bill of their disposal is more expensive than that of unfoamed non-recyclable polymers as their volume is huge. This requires reducing their size before dumping them in landfills.

Mosanenzadeh [31] used the salt leaching method to produce graded porous foam by stacking three different layers having different cell sizes as shown in Figure 2-25. The samples were prepared by mixing PLA with salts having particle sizes between 200 and 600µm in a weight ratio of 10/90. The thickness of all samples was the same. Figure 2-26 shows the SEM image of the developed porosity graded foam prepared by this method. It was found that the developed graded cellular structure improved sound absorption coefficient at higher frequencies (i.e. above 3000Hz) in comparison with that of homogeneous samples, as shown in Figure 2-27.

The salt leaching method used in the previous work is time consuming plus the produced foam does not maintain structure integrity. Also, the efficiency of the material in absorbing low frequency noise (i.e. below 800Hz) was not investigated.

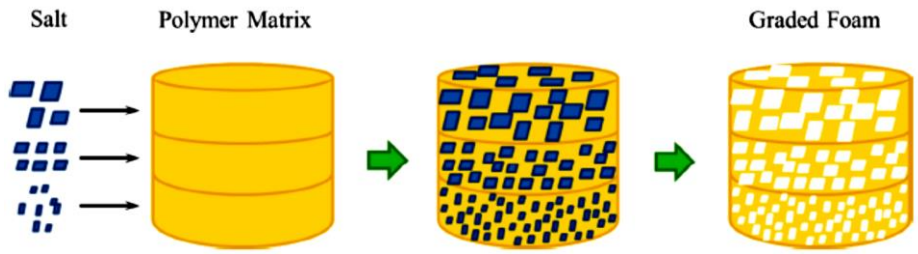

Figure 2-25: Schematic of particulate leaching technique to fabricate porous structures [31]

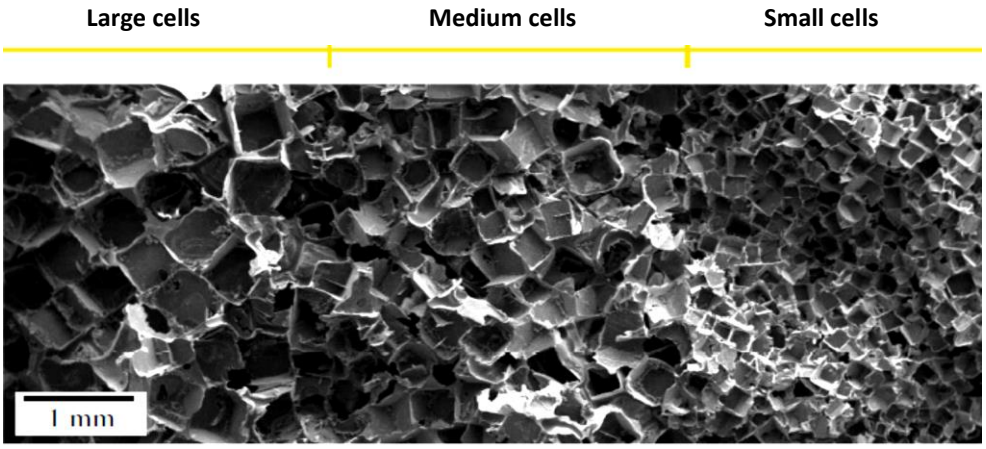

Figure 2-26: SEM micrographs of functionally graded PLA open cell foam [31]

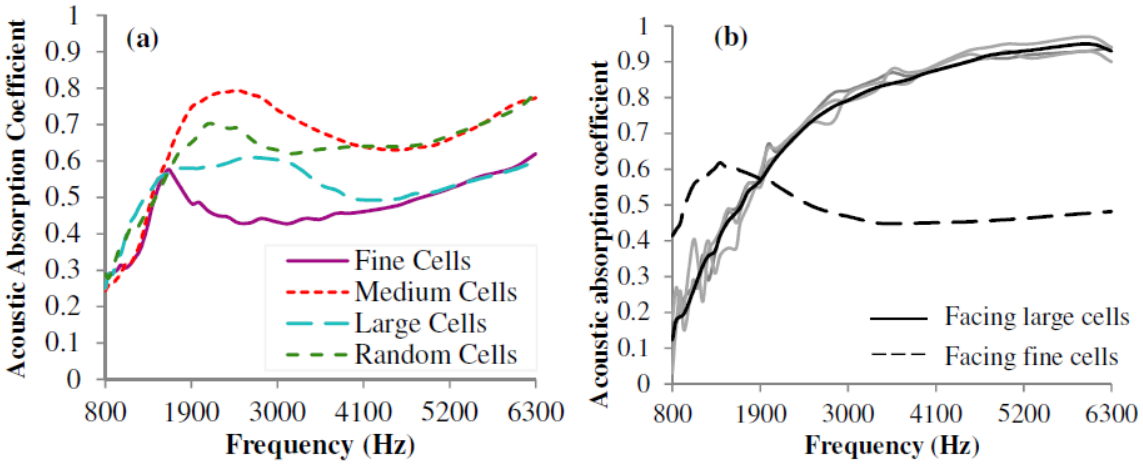

Figure 2-27: Sound absorption coefficient versus frequency for (a) PLA open cell foams and (b) functionally graded PLA foams [31]

2.4 Thermoplastic Foams

2.4.1 Introduction

Thermoplastic foams are manufactured by inflating thermoplastic polymers by gases, primarily for the purpose of reducing the weight and the cost of the products. Polymers can be expanded from 1.5 up to 50 fold, giving rise to foamed products with a broad density spectrum extending from 15kg/m^3 up to 750kg/m^3. Most importantly, the cellular structure of the produced foams can be tailored in accordance with cell size, cell geometry, cell orientation, cell density, degree of cell interconnectivity, cell wall thickness, and degree of anisotropy. All these variations in the architecture of foam internal structure result in a massive number of foam products with diversified properties. Polymeric foams are nowadays used in everyday life in such products/applications as footwear products, leisure equipment, decorative products, toys, pharmaceutical and cosmetic products, diapers, separators and pillars for batteries, upholstery, packaging, buoyancy, filters and membranes for separation processes, catalytic surfaces, impact mitigation, thermal insulation, sound absorption, and scaffolds in tissue engineering. Table 2-2 lists some of polymeric foams attributes and some relevant applications [32].

Open cell polymer foams with cell size in the submillimeter range possess acoustic absorption performance similar to that of mineral and glass fibers, such as glass wool and rock wool. They dissipate sound energy mainly by means of viscous friction during air passage through their tiny cellular network. Additional possible dissipation mechanisms include exchanging heat with the saturating fluid (which occurs at low frequencies), and structure damping (which is effective when they are flexible and highly porous). Acoustic foams have more privileges over mineral and glass fibers as they are easily and safely manufactured, flexible, durable, and compatible with different varieties of construction materials. Durable glues for bonding such foams with construction components are also available. Unlike fibers, they maintain structure integrity so that they can be easily packed [1, 4, 8, 33]. Moreover, the probability of their being swept with the flow when used in silencers for ducts and ventilation systems is less. The only limitation to be taken into

consideration when selecting them as acoustic treatment in building industry is their fire rating.

Table 2-2: Foam properties and application attributes [34]

Property	Attributes	Application
Physical	Density reduction	Save material, reduce cycle time
Mechanical	Compressive strength	Floating device, toys, surfboards
	High modulus	Coring component
	Rigid-open cell	Trays, liquid retention
	Flexible-high strength	Seat cushions, matrices, shoe soles, seals, gaskets
Energy	Soft-energy absorption	Packaging
	Rigid-energy absorption	Car bumpers
Thermal	High heat retention	Insulation boards, trays, cups, thermo-containers
	Rigid-high heat retention	Appliance panels, doors
	Thermoforming	Trays, dashboards
Acoustics	Rigid- sound blocking	Sound barrier panels
	Soft- sound absorptive	Studio panels, ear phones
	Semi rigid-sound absorptive	Floor assembly

2.4.2 Foam Definition and Classifications

Polymer foams are a special category of composite materials where one of the constituting phases is a gas dispersed, in the form of tiny bubbles, throughout a polymeric matrix [35]. Foams are classified in many different ways: by cell size and cell density, by foam density, and by morphology of the developed cellular structure. Depending on the cell size and the cell density achieved during foaming, foams are classified into conventional, fine-celled, and microcellular foams. The basis for such classification is given in Table 2-3. It is worth mentioning that microcellular foams are well-known for their superiority over their unfoamed analogues in some properties namely impact strength, toughness, fatigue life, and insulation properties [36-40].

Table 2-3: Foam classification by their cell size and their cell density [41]

Foam type	Cell size (μm)	Cell density (cells/cm^3)
Conventional	>300	$<10^6$
Fine-celled	10-300	10^6 -10^9
Microcellular	<10	$>10^9$

Foams are also divided into high density, medium density, low density, and very low density. The volume expansion ratio is the metric for such classification, and the limits for each of these types are listed in Table 2-4. Typically, high density grades are characterized by high strength and are therefore suitable for usage as structural components, in transportation/automotive and building industries. Low density grades are mainly used for speciality applications that do not require high strength. These applications comprise acoustic insulation, thermal insulation, separation and filtration, cushioning, buoyancy, and packaging. Medium density grades lay between these two extremes, and they provide products with intermediate strength [42, 43].

Table 2-4: Foams classification by their density [44]

Foam type	Expansion ratio (-)	Density (Kg/m^3)
High density	<4	>250
Medium density	4-10	100-250
Low density	10-40	25-100
Very low density	> 40	<25

Lastly, foams are classified according to structure morphology as open cell, and closed cell. In closed cell foams, adjacent cells are completely isolated from each other by polymeric walls or membranes, and the cells are filled up with the expanding gases which in turn are replaced later by air in a process called aging [45]. Closed cell foams are suitable for such applications as energy absorption (vibration/impact/shock), thermal insulation, buoyancy, and packaging [42, 46].

The structure of open cell foams differs from that of closed cell foams in that the walls between neighboring cells no longer exist, and the cells consist only of a network of polymeric edges (i.e. struts) which maintain the structure integrity of the foam. Open cell foams are principally used as filters, separation membranes in chemical industry and for water purification, as biological scaffolds in medicine, and as sound-absorbing materials in noise control engineering [47, 48]. Figure 2-28 displays [32]two SEM images showing the cellular structure of open cell foam (left) compared with that of closed cell foam (right).

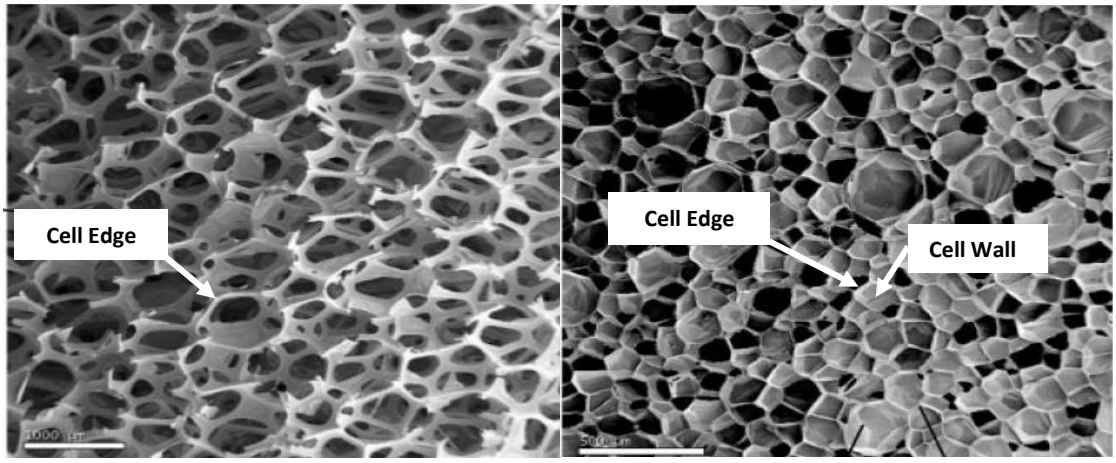

Figure 2-28: SEM images of open cell foam (left) versus closed cell foam (right) [49]

2.5 Thermoplastic Foam Production

2.5.1 Thermoplastic polymers

Thermoplastic polymers are made up of linear or branched polymer chains linked together by weak intermolecular physical forces. They soften and melt when heated, while they set when cooled. The curing process is completely reversible as no chemical bonding takes place. This characteristic allows thermoplastics to be remolded and recycled without negatively affecting the material's physical properties. Thermoplastics are divided into amorphous, semi-crystalline and crystalline polymers, depending on the extent of intermolecular interaction between chains. Thermoplastic polymers are normally processed by extrusion, injection molding, and thermoforming. Among thermoplastics polymers that have been successfully foamed are PE [50-52], PP [53-55], PS [56-59], PVC [60, 61], PC [37, 62-64], PMMA [65-67], PET [68, 69], and EVA [70, 71].

Ethylene vinyl acetate (EVA) is a random copolymer of ethylene and vinyl acetate monomers with vinyl acetate content (VA) ranging between 2 and 50% by weight. Figure 2-29 shows the molecular structure of EVA, whereas Figure 2-30 shows the relationship between vinyl acetate content and maximum molecular weight (left image), and density (right image) for EVA copolymers. All polymer properties are mainly function of VA content, which in turn influences the polymer in two different ways. First increasing VA content reduces the degree of crystallinity making the polymer more flexible and transparent. The polymer has a low softening temperature which is normally between 60-100^{o}C. Moreover, the increase in VA content results in an increase in polymer polarity, which is imparted by the acetoxy side group. Such polarity makes the polymer possess excellent resistance to aging, weathering, and color change in addition to having good mechanical properties [72]. Table 2-5 displays the effect of increasing VA content on some of the physical properties of EVA polymer.

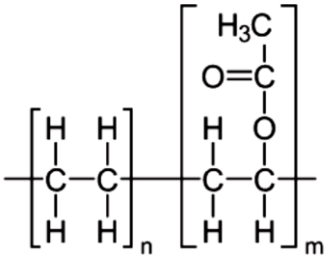

Figure 2-29: EVA molecular formula [73]

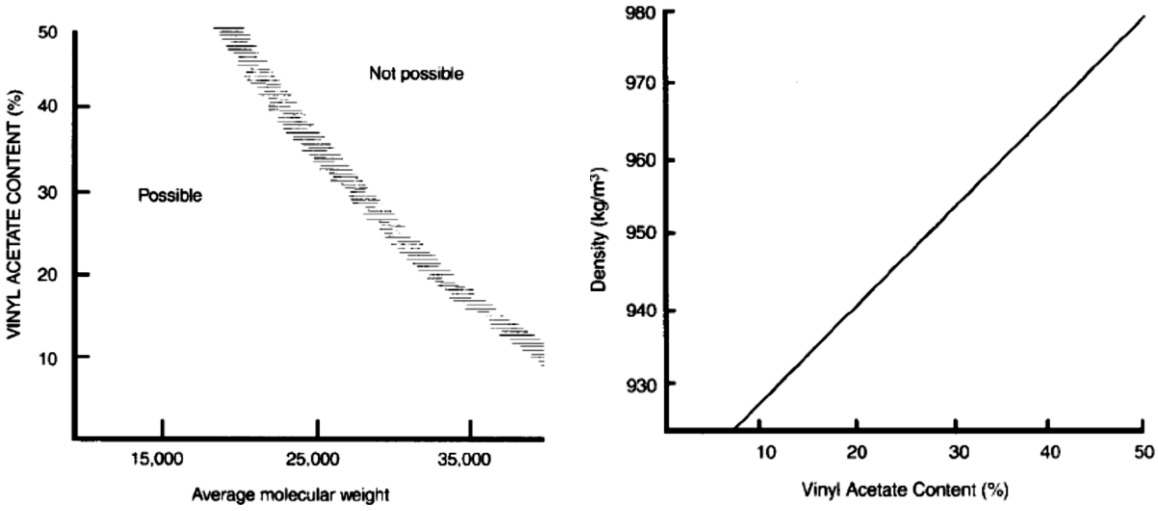

Figure 2-30: Influence of vinyl acetate content on EVA molecular weight (left image), and density (right image) [73]

The main disadvantage of EVA copolymers is their vulnerability to heat and solvents. The polymer is mainly used in applications including wire/cable insulation, sound damping sheets, packaging film, drug delivery device, adhesives/coatings, carpet backing, sports leisure, sports shoe soles, flexible shrink wrap, agricultural films, coatings, paints, semi-permeable film, flexible toys and tubing [74, 75].

Table 2-5: Change in physical properties of EVA as a function of decreased crystallinity due to increasing vinyl acetate content [73]

Stiffness modulus	Decreases
Surface hardness	Decreases
Crystalline melting point / softening point	Decreases
Tensile yield strength	Decreases
Chemical resistance	Decreases (generally)
Impact strength (especially at low temperature)	Increases
Optical clarity	Increases
Gas permeability	Increases
Environmental stress crack resistance	Increases
Coefficient of friction	Increases
Retention of mechanical strength at high fiber loadings	Increases
Compatibility with other polymers, resins, etc.	Variable

EVA is commonly added to polyolefins to improve their transparency, flexibility, thermal resistivity, stress cracking resistance, electrical resistance, and to increase their capacity to filler loadings. In addition, their blends are characterized by thermo-shrinkage and high resistance to aging, weathering, and corrosive media. These blends are strong candidates for such applications as high voltage cable systems, medical tubes, multi-layered packaging films and sheets, agricultural films, and automobile [76].

2.5.2 Blowing agents

- **Physical blowing agent**

Physical blowing agents (PBAs) are gases or volatile liquids, which after dissolution in the polymer melt, evaporate to expand polymers. Table 2-6 gives some physical properties, the ozone depletion potential (ODP), and global warming potential (GWP) of some PBAs. Chlorofluorocarbons (CFCs) and hydrochlorofluorocarbons (HCFCs) have been phased out due to their harmful environmental impacts (ODP-GWP) [77]. The second generation of physical blowing agents includes hydrofluorocarbons (HFCs) and hydrocarbons (HCs). HFCs are not commonly used because of their existing GWP [78].

Table 2-6: Commonly used physical blowing agents [3]

Blowing agent	**Chemical formula**	**Molar weight (g/mol)**	**Boiling temperature (ºC)**	**Flammable**	**ODP**	**GWP**
Isobutane	C_4H_{10}	58.1	-11.7	Yes	-	-
Cylclopentane	C_5H_{10}	70.1	49.3	Yes	-	0.00275
Isopentane	C_5H_{12}	72.1	29.0	Yes	-	-
CFC-11	$CFCl_3$	137.4	23.8	No	1.0	1.0
HCFC-22	CHF_2Cl	86.5	-40.8	No	0.05	0.35
HCFC-142b	CF_2ClCH_3	100.5	-9.2	Yes	0.05	0.38
HFC-134a	CH_2FCF_3	102.0	-26.5	No	-	0.27
Nitrogen	N_2	28.0	-195.7	No	-	-
Carbon dioxide	CO_2	44.0	-56.5	No	-	0.00025

Although organic hydrocarbons are excellent candidates for producing low density foams, due to their high solubility and low diffusivity in polymeric matrices [79, 80], they have some limitations on their utilization; they are flammable, toxic, and can form explosive mixture with air. Additionally, special equipment is needed for handling them, and the manufactured products need to be stored for a period of time, for aging, before launching to markets. Nitrogen and carbon dioxide are nowadays being used extensively as PBAs in plastic foam industry for a good number of reasons. They are environmentally-

friendly, non-toxic, non-flammable, inert, cheap, and available. The only issues associated with their usage are their low solubility and their high diffusivity in polymeric matrices. Carbon dioxide is more soluble than nitrogen, while the latter has less diffusivity. Normally they are fed in the supercritical state to facilitate and increase their sorption into the polymer melt. The enhancement in gas dissolution in the molten polymer is due to the fact that supercritical fluids are characterized by density similar to liquids and viscosity resembling gases [81-86].

- **Chemical blowing agent**

Chemical blowing agents (CBAs) are organic or inorganic solid compounds that decompose upon heating, and generate gaseous products plus some solid residues. The generated gases are responsible for inflating the polymer melt and developing the cellular structure. CBAs are mainly used to produce medium and high density foamed plastic and rubber commodities. Typical densities realized cover the range from 400 up to 800kg/m^3 which equivalently corresponds to a reduction in density by 20-45%. CBAs are not commonly used to produce densities below 400kg/m^3 for economic consideration, as their cost is nearly 10 fold that of N_2 or CO_2 gases obtained from cylinders. CBAs can also be used in conjunction with PBAs in extrusion and injection molding processes, to serve as nucleating agents [87].

After all, CBAs possess some merits which make them still competitive to physical blowing agents in some cases. First of all, they can be used to produce plastic foams by conventional plastic techniques, such as extrusion and injection molding, without the need to modify the production line. Second, they do not require any additional costly equipment for storage or for dosing like in the case of PBAs. Third, they can be used in plastic processes that operate under low/atmospheric pressure, like in rotational molding foaming, and oven heat foaming. Last, foams with fine-celled structure can be easily produced by using CBAs, as they are easily dispersed within the polymer matrix in addition to their self-nucleating nature [40, 87]. CBAs are divided into exothermic and endothermic depending on whether their decomposition is accompanied by heat release or heat absorption. Exothermic CBAs are organic solids that liberate large amount of heat during

decomposition. Consequently, their reaction is autocatalytic and occurs very rapidly. The main constituent of the decomposition gases is nitrogen. Examples of exothermic CBAs are azodicarbonamide (ADC) which is sold under trade names Celogen AZ and Genitron, and p,p´ oxybis(benezene sulfonyl hydrazine) (OBSH), which is sold under trade names Celogen OT and Neocellborn.

OBSH is characterized by a low decomposition temperature, which is compatible with the processing temperature of most polymers. Its decomposition temperature ranges between 158 and 167^{o}C. ADC, on the other hand, has higher decomposition temperature range (starting from 200^{o}C). Even though, the decomposition temperature of ADC can be lowered down to 140^{o}C by using some additives called activators (or kickers) like zinc oxide and zinc stearate. Foam products produced by exothermic It is worth mentioning that CBAs are not suitable for usage in toys, food and pharmaceutical industries as they contain hazardous residues of the CBA and its decomposition products [34, 88, 89]. The decomposition mechanism of OBSH is shown in Figure 2-31.

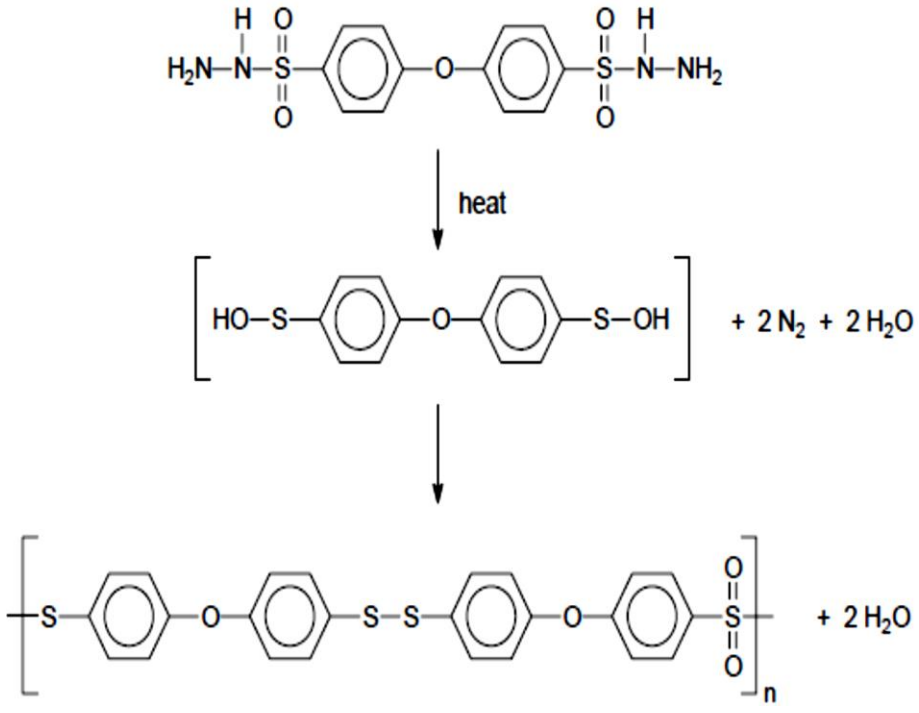

Figure 2-31: Decomposition mechanism of OBSH

Endothermic CBAs, on the other hand, are mostly inorganic solids. They absorb heat during their decomposition, and because of that, their decomposition reaction is slow leading to broader decomposition temperature ranges and longer decomposition times compared to exothermic CBAs. The main gaseous constituent of their decomposition is carbon dioxide. Examples of endothermic CBAs are sodium bicarbonate, oxalic acid, and hydrocel, which is an equimolar mixture of sodium bicarbonate and oxalic acid.

Unlike exothermic CBAs, endothermic CBAs conform to food and pharmaceutical industries, since they are food additives [34] . The main characteristics of some chemical blowing agents are listed in Table 2-7, while a comparison summary between endothermic, exothermic, and enexothermic CBAs are displayed in Table 2-8.

Table 2-7: Major properties of chemical blowing agents [87]

Product	**Decomposition range (°C)**	**Gas evolution (ml/g)**	**Main gases**
ADC (ADCA)	200-215	200	CO , CO_2 , NH_3
ADC (ADCA) activated	140-215	130-220	N_2 , CO , CO_2 , NH_3
DNPT	190-200	190-200	N_2 , NH_3, CH_2O
THT	245-285	180-210	N_2 , NH_3
TSH	105-110	115	N_2 , H_2O
OBSH	155-165	110-125	N_2 , H_2O
TSSC	225-235	120-240	N_2 , CO_2 , NH_3
5-PT	240-250	190-210	N_2
$NaHCO_3$	110-150	160-190	CO_2 , H_2O
$NaHCO_3$/Citric comp.	130-230	110-180	CO_2 , H_2O

When selecting between CBAs for foaming thermoplastics, there are three important criteria to be taken in consideration. Most importantly, the decomposition temperature should be higher than the polymer processing temperature, but not by much. A decomposition temperature lower than the polymer processing temperature led to losing the decomposition gases because of the high stiffness of the polymeric matrix. Higher decomposition temperature weakens the polymer melt strength and causes occurrence of

cell coalescence and collapse leading to the formation of foams with inferior mechanical properties. The second criterion for CBA selection is the amount of gas evolved during decomposition, as it is a measure of foaming efficiency (i.e. maximum expansion that can be achieved). Last but not least, the gaseous products and solid residues resulting from the decomposition reaction must be benign to the polymer matrix, and meanwhile, do not cause corrosion of the used equipment [87, 90].

Table 2-8: Comparative summary between exothermals, endothermals, and their blends in the injection molding process [3]

Properties	**Exothermals**	**Enexothermals**	**Endothermals**
Weight/density reduction	Excellent	Very good	Good
Surface roughness	Poor	Reasonable	Excellent
Fine cell structure	Coarse	Reasonable	Excellent
Sink mark reduction	Good to excellent	Good to excellent	Excellent
Cycle time reduction	0%	10-30%	20-40%
Food grade status	Limited	Limited	No problem
Color	Yellow	White to yellowish	White
Discoloration tendency	Yes	Reasonable	No
Smell	Pungent (NH_3)	Reasonable	Little
Gas evolution	Nitrogen	Nitrogen, CO_2	CO_2
Gas pressure	High	Medium	Medium/low
Environmental aspect	Limited impact	Limited impact	Little/no impact

2.5.3 Foaming Mechanism

Figure 2-32 shows the basic steps included in foaming mechanism.When an appropriate amount of PBAs, depending on the solubility, is fed into a polymer melt, it completely dissolves in it, forming a metastable solution. Reducing the pressure and/or decreasing the temperature induce thermodynamic instability promoting phase separation. The dissolved gas/liquid molecules start to form clusters, to minimize the system free energy, and as a result, tiny nuclei (embryos) are formed throughout the polymer melt in a process called ‘nucleation’ [41, 80, 91].

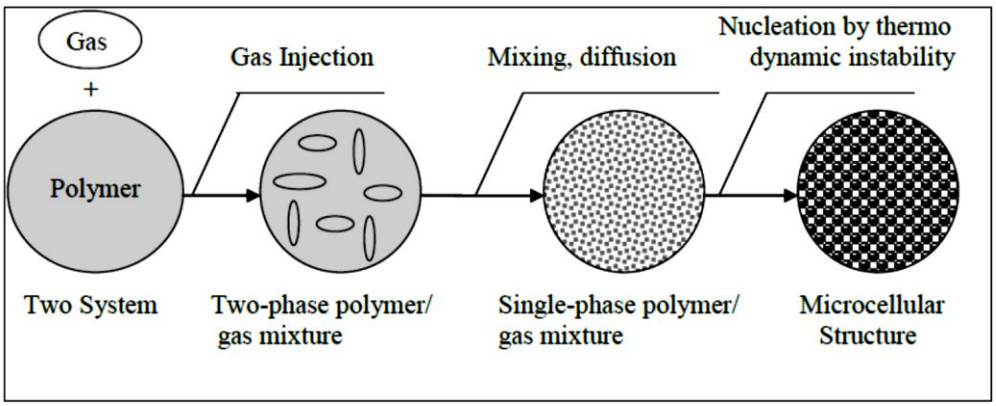

Figure 2-32: Phase changes in polymeric foaming process [92]

Nucleation can take place either homogeneously or heterogeneously. In homogeneous nucleation, a number of gas molecules start to cluster together, forming an embryo, within the molten polymer phase without using any additives. The activation energy required to initiate homogeneous nucleation (ΔG^*_{homo}) is given by:

$$\Delta G^*_{\text{homo}} = \frac{16\pi\gamma^3}{3(P_{sat} - P_s)^2} \tag{2.26}$$

The critical radius (r^*), which is the minimum nucleus that can survive, is given by:

$$r^* = \frac{2\gamma}{P_{sat} - P_s} \tag{2.27}$$

And the nucleation rate (N^*_{homo}) is given by:

$$N^*_{\text{homo}} = f_0 C_0 \exp\left(\frac{-\Delta G^*_{\text{homo}}}{kT}\right) \tag{2.28}$$

Where σ is the polymer surface tension, P_{sat} is the saturation pressure, and P_s is the surrounding pressure, $(P_{sat} - P_s)$ is the degree of supersaturation, f_0 is a frequency factor representing the rate at which gas molecules combine with the critical nucleus; and C_0 is the concentration of gas molecules, T is the absolute temperature, and k is Boltzmann's constant. It is clear, in light of the above equations, that increasing the degree of supersaturation reduces the critical radius, and increases the nucleation rate. Generally, the nucleation rate in homogeneous process is low and the developed cellular structure is not

uniform. Fillers act as catalysts by providing surfaces on which nucleation can take place easily. This reduces the activation energy required for nucleation as shown in Figure 2-33 by a factor $f(\theta)$ [51, 93]:

$$\Delta G^*_{hetero} = \Delta G^*_{homo} f(\theta) \tag{2.29}$$

The heterogeneity factor $f(\theta)$ is given by:

$$f(\theta) = \frac{(2+\cos\theta)(1-\cos\theta)^2}{4} \tag{2.30}$$

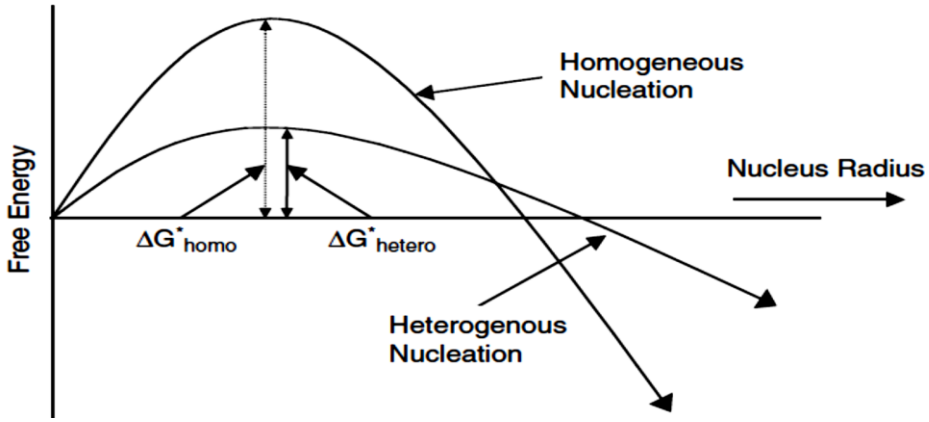

Figure 2-33: Heterogeneous bubble nucleation [93]

where θ is the wetting angle shown in Figure 2-34, and it depends on the nature and geometry of the particle. The addition of fillers results therefore, in increasing the nucleation rate, reducing the critical radius, and improving uniformity of foam cellular structure.

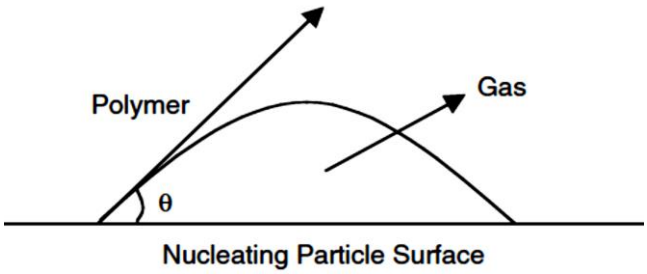

Figure 2-34: Schematic of nucleating particle interaction with gas and polymer [93]

In the third step of foaming, the formed embryos continue to grow in size to equilibrate their pressure with the surrounding pressure, which is less than the bubble internal pressure. This is accomplished by diffusion of more gas/liquid vapors into the formed nuclei in a process called 'growth'. And in the last step of foaming, a stabilization procedure is required to preserve the developed cellular structure otherwise the growth step continues until the developed cellular structure undergoes coalescence and/or collapse. Since the growth step is principally controlled by the polymer melt viscosity, stabilization can be achieved by increasing the polymer melt viscosity either by cooling, or by crosslinking the polymer melt [34, 51, 80].

There are two foaming mechanisms when using CBAs, as foaming can take place under either high pressure or atmospheric condition. In case of applying pressure, the decomposition gases, which mainly consists of N_2, completely dissolve in the polymer melt. In a similar way to PBAs foaming, reducing the pressure induces thermodynamic instability, and causes the dissolved gas to diffuse out of the polymer melt, promoting cell nucleation and growth [34]. The decomposition residues also act as nuclei leading to heterogeneous nucleation. This reduces the requirement for high homogeneous nucleation, which in turn reduces the requirement of generating a high thermodynamic instability [94]. Countering that, N_2 is negligibly soluble in the polymer melt under atmospheric condition [95], and foaming process in that case is mainly governed by diffusion-controlled cell growth [96]. The generated gases have to be trapped within the molten polymer otherwise they will eventually escape to the ambient atmosphere. This can be done by adding fillers which act as trapping sites. The decomposition gases diffuse to these sites, cluster together forming nuclei. Crosslinking can also do the job by reducing the diffusivity of N_2, and decreasing its tendency to escape.

2.5.4 Foam manufacturing processes

No single foaming process predominates thermoplastic foam manufacture. Currently both continuous and batch processes can operate with either chemical or physical blowing agents for production of thermoplastic foams. Among the most commonly used

processes for foam production are extrusion [97, 98], injection molding [44], rotational molding foaming [40, 99, 100], compression molding foaming [101-104], bead foaming [41], oven heat foaming [105], and gas dissolution in a batch process [106-108]. Salt leaching method can also be used to produce foam samples with tailored cellular structure, but for small scale production (i.e. for laboratory scale production of biodegradable scaffolds in tissue engineering) [101, 109-111].

- **Compression molding**

Compression molding is considered one of the oldest techniques used for processing thermoset polymers. It can be used to produce thermoplastic polymers and composite thermoplastics as well. The process is handy with a few number of processing parameters, and its machinery is simple, inexpensive, and easy to maintain.

The machinery used in the process is a simple press consisting of two hydraulically-operated platens with sizes from $6in^2$ up to $8ft^2$. The platens can exert forces ranging from 6 up to 10,000tons. The hydraulic press is normally fitted with pressure gauges for pressure monitoring, thermocouples, and temperature controllers to monitor and control the temperature of the upper and lower platens. Though the technique throughput is small compared to these of injection molding and extrusion techniques, it has some advantages that allow it to survive among such productive techniques. The technique is versatile and suitable for processing a wide variety of thermoplastic polymeric matrices. The process is also characterized by lower cost of investment; short operating cycles, capability of producing large size parts, good surface finish, and relatively little material wastes [112].

Compression molding can be utilized in producing thermoplastic foams [50, 113-118]. The basic steps of foam production using compression molding are shown schematically in Figure 2-35. Thermoplastic foams can be manufactured using compression molding in either a single-stage or a two-stage foaming process.

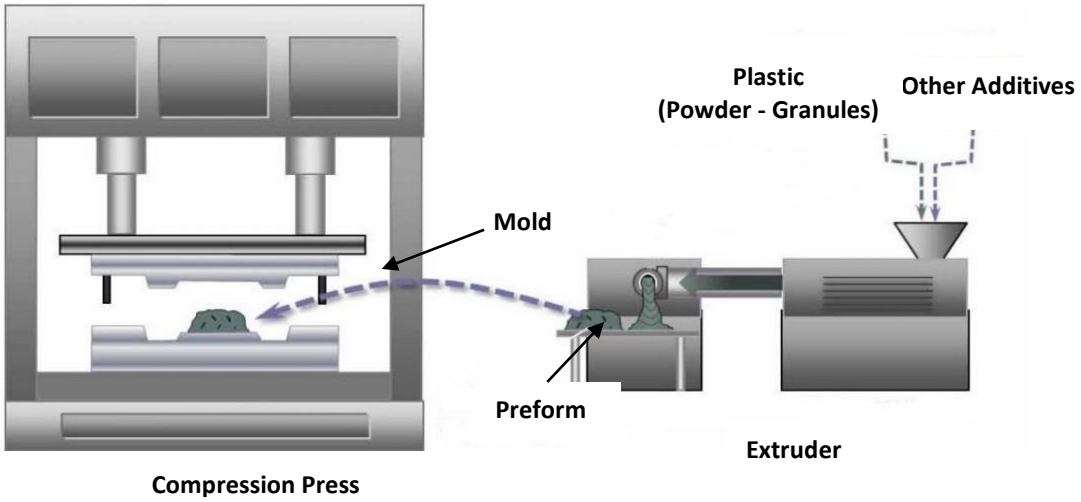

Figure 2-35: Production of polymeric foams using compression molding technique [112]

In the single-stage process, the polymer, CBA, and other additives are melt mixed using an extruder. The foamable mix (preform) is then placed inside a mold kept under high pressure, and at a temperature higher than the decomposition temperature of CBA. Once the CBA completely decomposes, the pressure is instantaneously released inducing foaming. Last the cellular structure is stabilized by passing water though the mold channels. Although the method is simple, it is difficult to control the final foam density and developed cellular structure as nucleation and growth are coupled in the process. In the two-stage process, nucleation and growth are performed in two separate steps which make it easier to control the developed cellular structure and final foam density. Also densities down to $20kg/m^3$ can be achieved through crosslinking in the process. In the first step of the two-stage process, nucleation and crosslinking take place, while expansion is conducted in the second stage which is carried out in a larger mold, and under atmospheric pressure [118].

- **Salt leaching method**

Preparing highly porous scaffold by means of salt leaching is commonly used in tissue engineering for production of biodegradable scaffolds. The cell size obtained by this method depends on the particle size of the used salt, while porosity is a function of the amount of salt added. The principle of salt leaching can be applied in two different ways. In the first method, which is called solution casting/particulate leaching, the polymer is

initially dissolved in a suitable solvent, and then specified amount of a porogen (i.e. pore generating material) is added to the solution to form a paste-like mixture. This mixture is casted into a mold, and placed under vacuum to get rid of the solvent, and to form a solid salt-embedded polymer disc. The formed disc is then immersed in distilled water for 3 days to dissolve the salt, and to develop cellular structure. Last, the prepared foam samples are dried in an oven. This method requires long times to evaporate the solvent, and uses large amounts of solvent which is not favored from the point of view of toxicity, flammability, and other environmental considerations. Also, residues of this hazardous solvent may remain in the produced scaffold [111, 119, 120].

For the above-mentioned reasons, a new solvent-free method, called melt molding/particulate leaching, was developed to replace the solvent-based one. In the new method, specified amounts of the polymer and the porogen are dry mixed. After that, the mixture is inserted into a mold kept between two hot plates, and heated for few minutes without applying pressure until the polymer starts to soften. The mold is then closed, and pressure is applied for a certain period of time to mold the sample. By the end of the molding time, the mold is cooled to harden the sample, and the sample is removed and immersed in water bath to leach the salt, and develop the cellular structure. Last, the leached sample is dried in an oven [101, 121].

2.6 Polymer Foams with Heterogeneous Cellular Structures

Polymer foams with heterogeneous cellular structures manifested their usefulness in many different engineering applications due to their capability of maximizing the material performance by compromising two or more contradicting properties. Most importantly, heterogeneous cellular structures are promising for tackling the problem of low frequency noise, which constitutes a big challenge to automotive, transportation and building industries. There are two different useful types of heterogeneous cellular foams: double porosity, and graded porosity foams.

2.6.1 Double porosity foams

The cellular structure of double porous foams consists of a combination of two different cell size domains (small cells/large cells). Small cells are characterized by large specific surface area, which is important for heat/mass exchange and cell implantation processes. Large cells, on the other hand, constitute the access paths to such sites. These cells help accelerate the diffusion process, and reduce the pressure drop developed across the porous material. Double porous foams are important for applications such as tissue/bone implantation, catalysis, filtration, and sound absorption [122].

Some researchers investigated the feasibility of developing dual porosity polymer foams during the foaming process. For instance, Taki et al. [123] found that foams produced by gas foaming of polyethylene glycol (PEG) and polystyrene (PS) blends exhibit excellent dual cellular structure. In their experiments, PEG and PS were first blended in different weight ratios (10/90, 25/75, and 40/60 PEG/PS), and the prepared blends were then molded in the form of discs. These discs were thereafter inserted in a high pressure vessel, which was pressurized with CO_2 gas under a pressure of 10MPa and at a temperature of 110°C. After saturation, the vessel was rapidly depressurized at a rate of 5MPa/s to induce nucleation, and to start foaming. The produced foams were characterized by a combination of smaller cells with average size of 30μm along with larger cells with average size of 400μm. Larger cells was formed in PEO phase due to the higher solubility and diffusivity of CO_2 in it, and occurrence of cell coalescence in the low melt strength PEO phase.

A scanning electron microscope image showing the dual porous structure of a foam sample prepared from PEG/PS blend in weight ratio 10/90 is shown in Figure 2-36. The limitation of the previous work is associated with the use a lab-scale batch foaming process which is not convenient for large scale foam production due to the long processing times and the limited sample sizes.

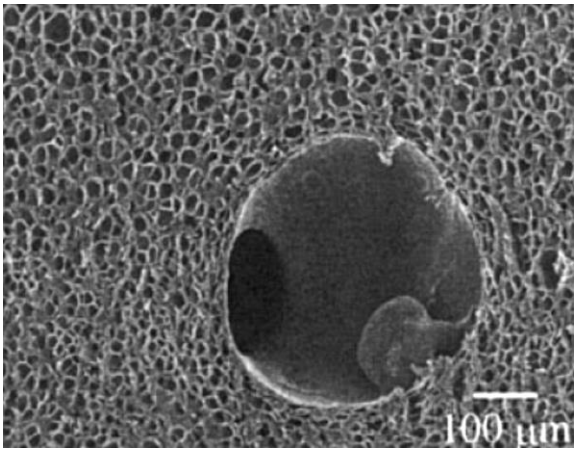

Figure 2-36: Cellular structure of the PEG10/PS90 blend foam prepared at 110°C and 10 MPa [123]

Salerno et al. [122] prepared dual porosity foams from poly (ε-caprolactone) (PCL) by combining gas foaming process with selective leaching method. They first blended PCL with thermoplastic gelatin (TG) in weight ratios of 40/60-60/40 PCL/TG to produce blends with co-continuous morphology. These blends were then gas foamed by means of N_2-CO_2 mixtures (volume ratios ranging between 0/100 and 80/20). The foaming temperature varied in the experiments from 38 to 110^{o}C. After completing the foaming step, TG was extracted by rinsing the produced foams in distilled water. Highly interconnected PCL bimodal porous foams could be produced when foaming was performed at 44^{o}C. The size of the small cells was in the range of 10-30µm (Figure 2-37-b), while the larger cells size was around 200-300 µm (Figure 2-37-a). Similarly, this work used a lab-scale batch foaming process, and the produced foams were characterized by open porosity of less than 50% making it inappropriate for sound absorption application.

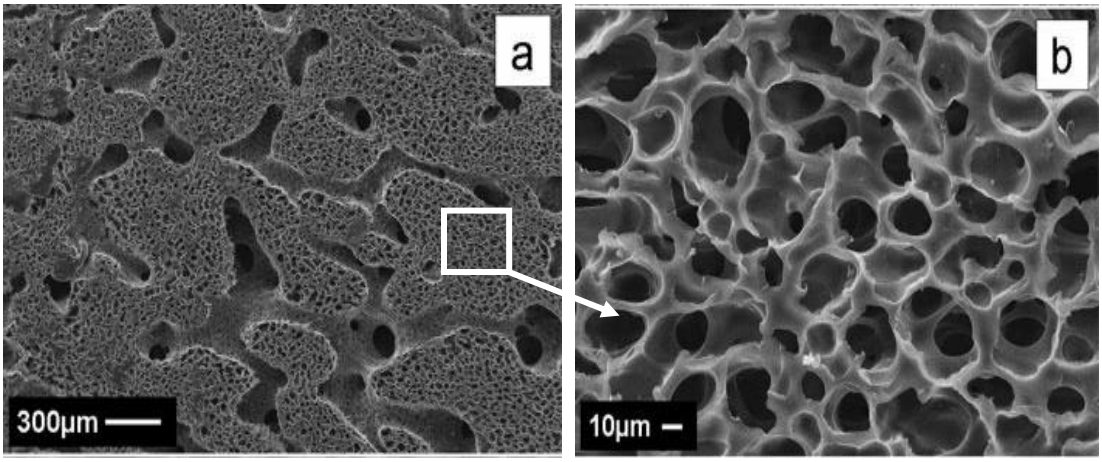

Figure 2-37: SEM micrographs of dual PCL scaffold prepared by GF/PE technique from PCL/TG (60/40) [122]

2.6.2 Graded porosity foams

Functionally graded materials (FGMs) are characterized by composition and/or structure that change continuously from one position to another throughout the material [124]. This implicitly means that all of the material properties, such as physical, electrical, thermal, mechanical, and acoustic, etc., will be dependent upon the position within the material. Due to this continuous change in properties, these materials do not experience the stress jumps and delamination issues that occur in composite materials. Graded porosity foams are a subcategory of FGMs where the cell size and/or cell density change gradually across the material either axially or radially. Bones, and wood are natural examples of graded porous materials. This graded structure maximizes the performance of the material by achieving a compromise between different contradicting properties. For example, birds eggshell is characterized by graded porous structure; the pore size varies from 100nm (inside) to a couple of microns (outside) .This structure guarantees the transfer of matter across the eggshell, while maintaining good mechanical properties to protect the shell from being damaged by external impacts [125, 126]. Graded porous foams also provide a significant weight reduction, along with a reasonable strength making them possess excellent weight/strength, and weight/stiffness ratios. All these advantages rendered these uniquely-structured materials strong candidate for applications such as biomaterials, sound absorption, energy conversion, and coatings [127, 128].

Zhang [129] produced graded porous foam by controllable growth of co-continuous polymer blends. In his experiments, polylactic acid (PLA) and polystyrene (PS) in a weight ratio of 50/50 were melt blended to form a co-continuous morphology. Afterwards, the blend was quenched in cold water to trap the developed morphology. The blend was then annealed between two hot plates. The lower plate was kept at room temperature, while the upper plate was set at 200°C as shown in Figure 2-38. After annealing for 30 min followed by selective extraction of PLA, large pores with size around 200μm were formed on the hot platen side (Figure 2-39-d), whereas the pore size on the cold platen side remained unchanged with size of several microns, which was primarily formed during the mixing step (Figure 2-39-b).

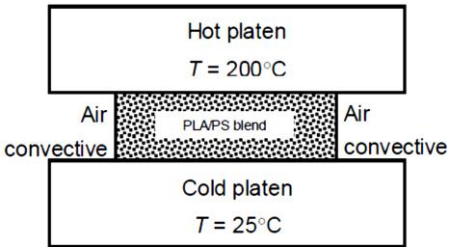

Figure 2-38: Thermal boundary condition for graded porosity formation [77]

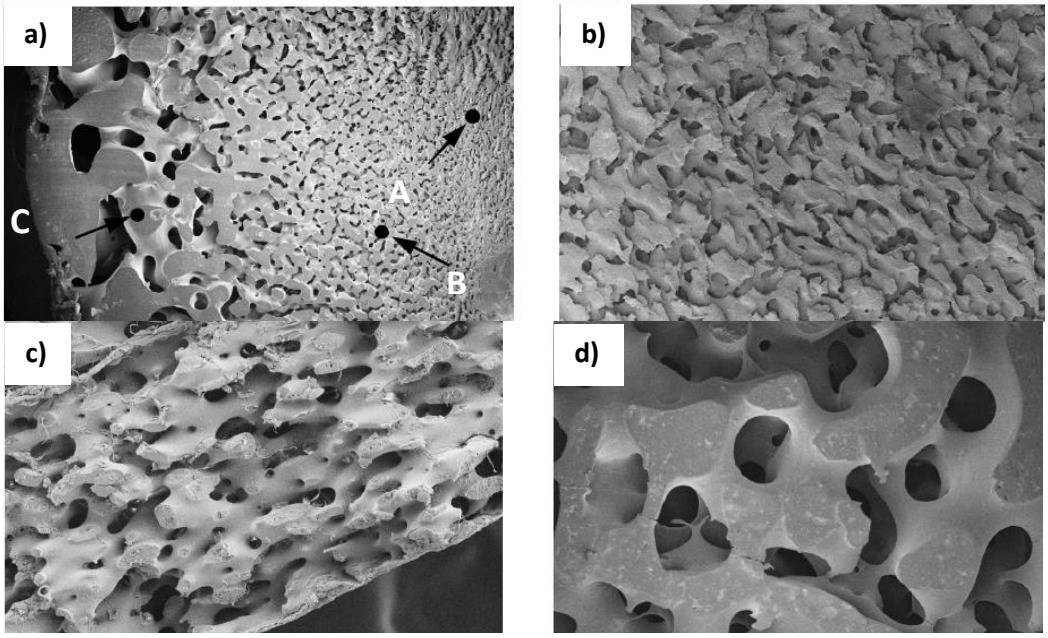

Figure 2-39: Gradient porous structure from 1-D thermal gradient: (a) overall structure, (b) cross-sectional structure at location A, (c) cross-sectional structure at location B, and (d) cross-sectional structure at location C [77]

The limitation of this approach is that the maximum porosity achieved, which depends on the percentage of the PLA phase, was less than 50%. The open porosity have to be more than 75% to serve as sound absorbing material.

Yao and Rodrigue [115] managed to produce closed cell foams with graded porosity by applying temperature gradient during compression molding foaming process. In their experiments, the polymer and CBA in powder form were mixed in a high shear mixer, and then compression molded to form molded solid discs. These discs were foamed symmetrically and asymmetrically by controlling the temperatures of the upper (T_H) and lower (T_L) plates of the press. Experimental results showed that the foam density did not change across the sample thickness when the upper and the lower plates were set to the same temperatures. However, the foam density decreased with increasing the foaming temperature. These two conclusions are shown in Figure 2-40.

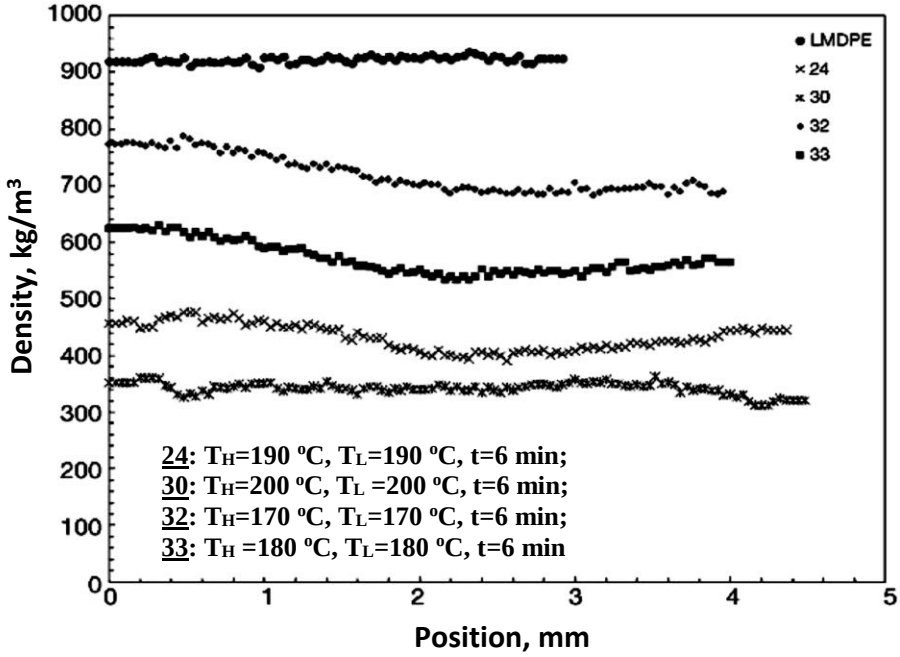

Figure 2-40: Density profiles of structural foams produced with 0.5% (32 and 33) and 1% (24 and 30) blowing agent at different molding temperatures [115]

They also found that closed cell foams with graded density, as shown in Figure 2-41, were developed when the upper and lower plates were set to two different temperatures. Additionally, the density gradient increased when the temperature difference between the

two plates was increased, and when increasing the concentration of the chemical blowing agent as well. Though this approach managed to produce graded porous structure, it is limited by achieving very small expansion ratio (less than 3). The produced foams are characterized by closed cell structure, and not suitable for sound absorption applications.

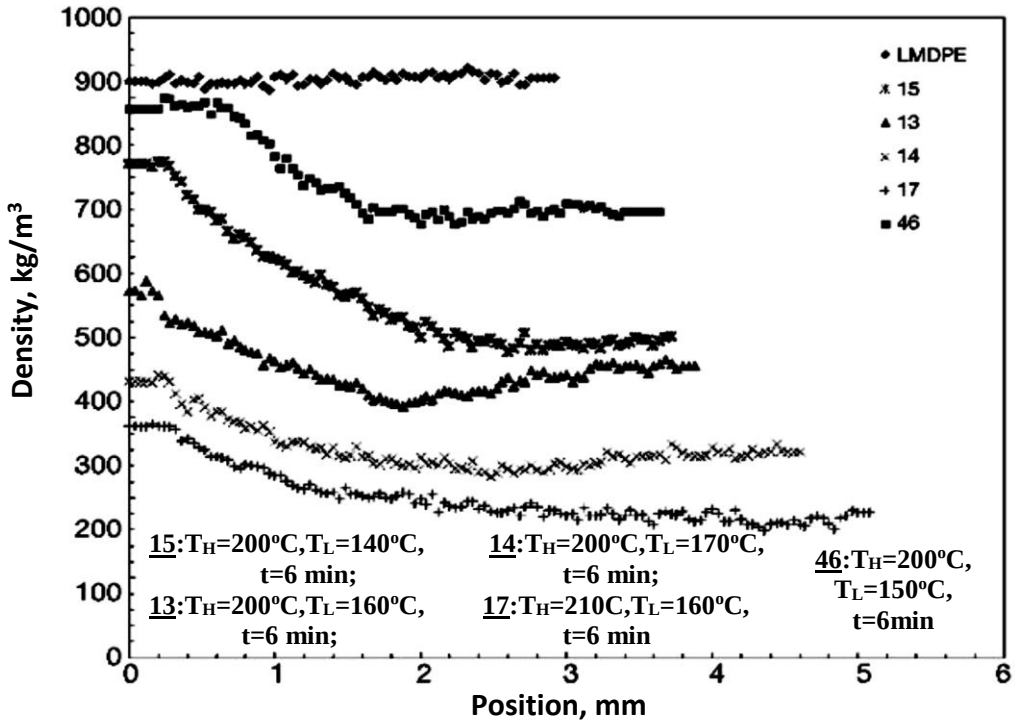

Figure 2-41: Density profiles for structural foams produced with 0.5% (46) and 1% (13, 14, 15, and 17) blowing agent at different molding temperatures [115]

Al Jahwari et al. [130] also managed to produce closed celled foams with graded porosity from acrylonitrile-butadiene-styrene trepolymer (ABS) by combining solid state batch foaming with compression molding. In the first step of their experiment, ABS sample was saturated with CO_2 gas by inserting it in a CO_2-pressurized container. Three different temperatures, $1/2T_g$, $2/3T_g$, and $3/4T_g$, were examined for foaming. After saturation, the vessel was rapidly depressurized to induce nucleation in the solid state. Heterogeneous foam expansion was conducted in a second separate step, by heating the pre-foamed samples between two hot plates set at two different temperatures for different time periods (1, 2, 5, and 10 min). The imposed temperature difference was intended to decompose the chemical blowing agent at different rates, producing different amount of expanding gases.

As a consequence, the preformed nuclei in the first step expanded non-uniformly across the material thickness. The SEM image of the developed structure, showing the variation of cell size and porosity with position, is shown in Figure 2-42. The limitation of this work is the use of the lab-scale batch foaming process, plus the produced heterogeneous polymer foams had closed cell structure making it unsuitable for sound absorption application.

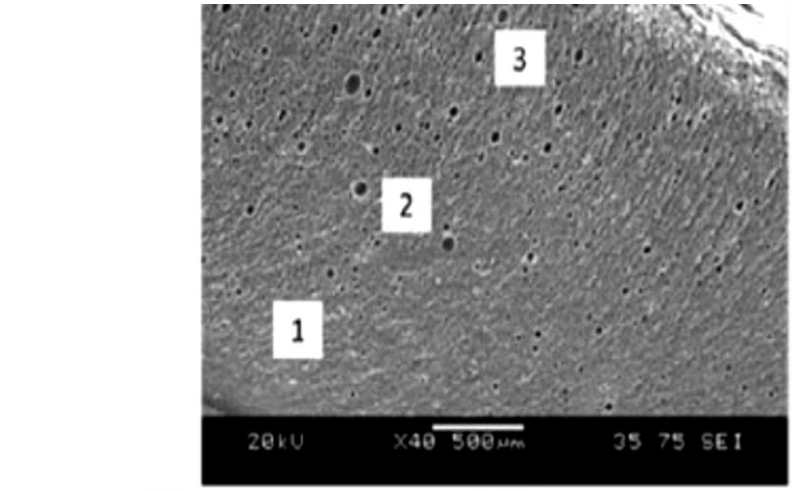

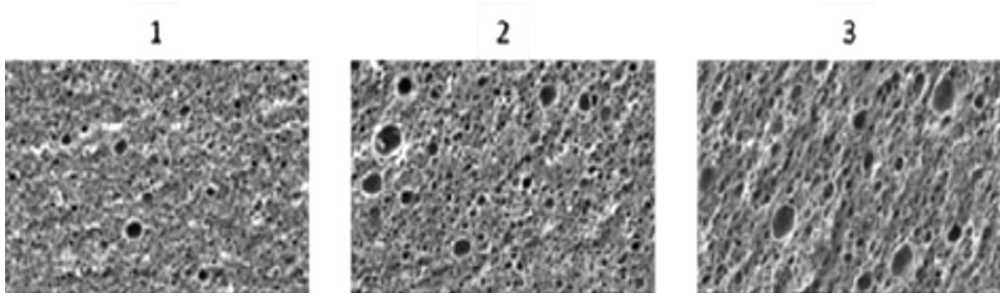

Porosity	**50.422**	**54.337**	**55.848**
Cell size (µm)	**3.537**	**4.428**	**4.443**

Figure 2-42: The cellular distribution of a functionally graded ABS: T_H=125 ^oC, T_L=52.5^oC, $t_{annealing}$=5 min, P_f =13.8MPa, and T(Stage-1)=52.5^oC [130]

2.7 Summary of Literature Review and Research Needs

It turns out from litertaure that the unique cellular structure of heterogeneous porous foams, such as double porosity and graded porosity foams, makes them very important for many engineering application especially the damping of low frequency noise which consitutes a big challenge to automotive, transportation and building industries.

The mechanical perforation method used to produce double porosity foams requires additional post processing step which increases the production cost, besides the produced foams experience high sound tranmision. Particulate leaching and batch gas foaming methods used to produce double porosity foams have some disadvantages including long processing times, small sample sizes, and poor structure integrity of the produced foam. There is a need to produce double porosity open cell thermoplastic foams by an economic process that can be scaled up for mass production. It is also required to test the efficiency of the produced foams in sound absorption over the low-mid frequency range.

Furthermore, methods reported in literature for fabrication of graded porous foams produced foams that experience some shortcomings such as non-recylability, decreased porosity, and closed cell structure. Such foams are not favored for enviromnetal considerations, in addition to their inadequacy to sound absorption applications. The salt leaching-layer stacking method reported in literature exhibits long processing times, and the produced foams do not maintain structure integrity. There is a need to produce open cell graded porous thermoplastic foams by an economic process that can be scaled up for mass production. It is also required to test the efficiency of the produced foams in sound absorption over the low-mid frequency range.

Chapter 3 Experimental Methods

3.1 Materials

3.1.1 Polymers

Two grades of EVA (Lyondellbasell, USA) with different vinyl acetate contents (9 and 18%) were used in the study. The properties of each of these grades are displayed in Table 3-1. The polymers were provided in powder form, and they were further sieved through the 35mesh sieve (250μm) before use. Differential scanning calorimetry test (DSC) was conducted on the polymers using Q20 (TA Instruments, USA) to measure the melting point (T_m), crystallization temperature (T_c), and degree of crystallinity of each polymer. A heat-cool-heat cycle was performed with a nitrogen flow rate of 50ml/min and at a heating and cooling rates of 5^{o}C/min. The resulting thermograms of the two polymers are shown in Figure 3-1 and Figure 3-2, while Table 3-2 lists the DSC analysis results. It is clear that EVA with 18%VA has lower degree of crystallinity, which is 5.15% compared to 9.37% for the 9%VA grade, and lower melting point which is less than that of the 9%VA grade by about 10^{o}C. Furthermore its crystallization is more delayed, and it takes place at lower temperature (68.23^{o}C compared to 81.88^{o}C for the 9%VA grade). These variations in properties are mainly attributed to the difference in VA content.

Table 3-1: Properties of two different EVA grades

Property	**EVA grade**	
	MU76000	**MU76300**
Vinyl Acetate Content (%wt.)	18	9
Density (g/cm^3) (ASTM D1505)	0.941	0.927
Melt flow index (g/10 min) (ASTM D1238)	32	10
Vicat softening point (^{o}C) (ASTM D1525)	54	72

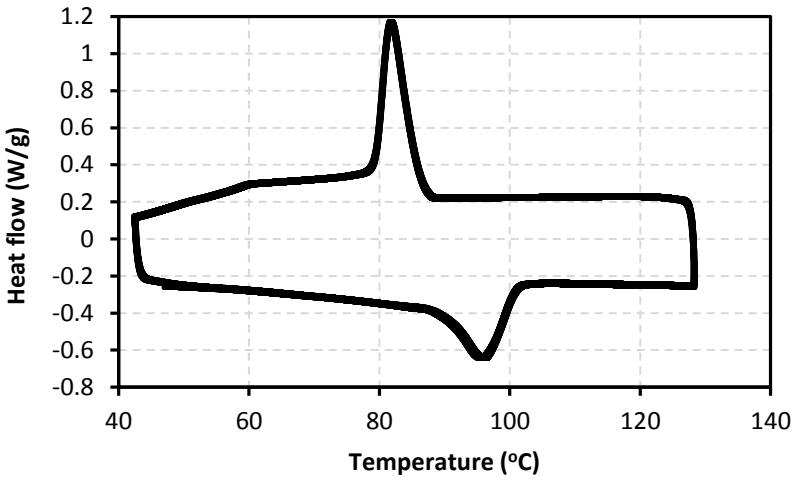

Figure 3-1: DSC thermogram of EVA with 9%VA

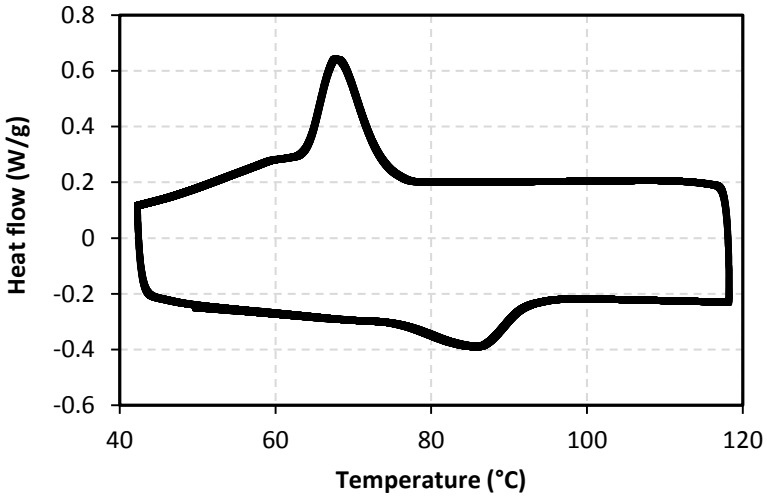

Figure 3-2: DSC thermogram of EVA with 18%VA

Table 3-2: DSC analysis results of EVA grades

VA (%)	Melting Peak		Crystallization Peak		Degree of Crystallinity (%)
	Temp. (°C)	Enthalpy (J/g)	Temp. (°C)	Enthalpy (J/g)	
18	86.64	14.93	68.23	29.23	5.15
9	96.36	27.18	81.88	43.62	9.37

Thermogravimetric test (TGA) was also conducted on the raw polymers using Q50 (TA Instruments, USA) to study their thermal stability. A simple heating ramp test was carried out with a nitrogen flow rate of 40ml/min for the sample, and 60ml/min for the balance, and at a heating rate of 10°C/min. The resulting thermograms of the two polymers are shown in Figure 3-3 and Figure 3-4. It is obvious that both polymers are thermally stable up to 300°C, and they undergo decomposition over the temperature range 325-500°C, with a maximum decomposition rate occurring at 475°C for the 9% VA grade, and 500°C for the 18% VA grade.

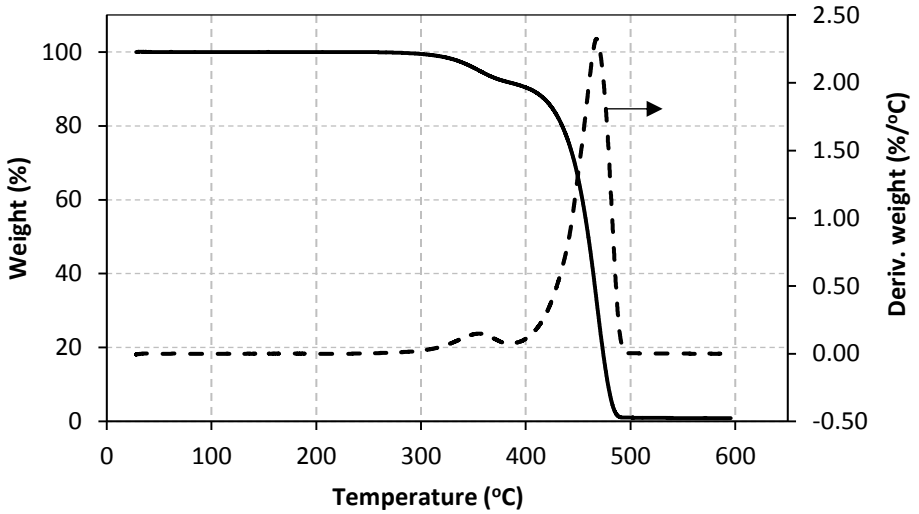

Figure 3-3: TGA thermogram of EVA with 9%VA

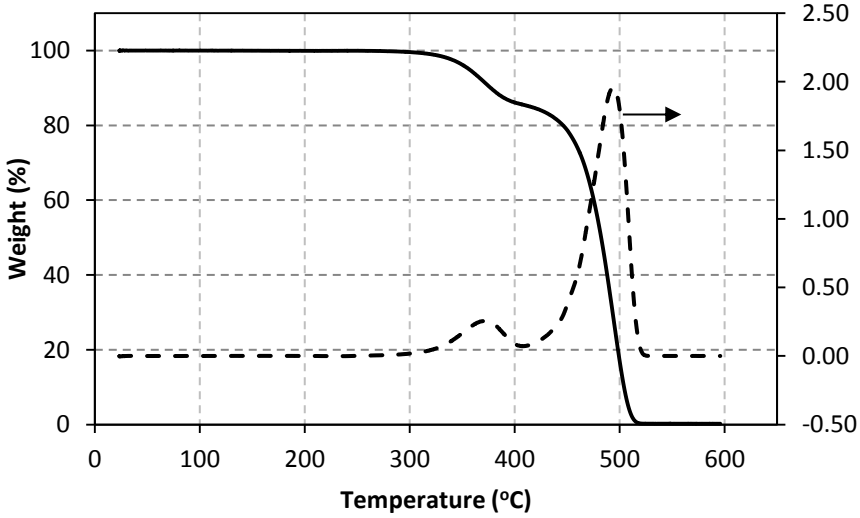

Figure 3-4: TGA thermogram of EVA with 18%VA

The rheological properties of the polymers were tested using ARES rheometer (TA Instruments, USA). Before running the frequency sweep test, a strain sweep test was conducted at a fixed frequency of 1Hz to obtain the linear viscoelastic region (LVR) for the two polymers. A strain of 5% was found to be within the LVR for both of them, and this value was selected for the subsequent dynamic frequency sweep tests. The frequency sweep test was conducted at four different temperatures, 120, 140, 160, and 180^{o}C.

Figure 3-5 and Figure 3-6 show the variation of complex viscosity with frequency at different temperatures for these two polymers. The resulting curves were extrapolated using Carreau model to get the zero shear viscosity of the polymers. The zero shear viscosities of the two polymers are listed in Table 3-3.

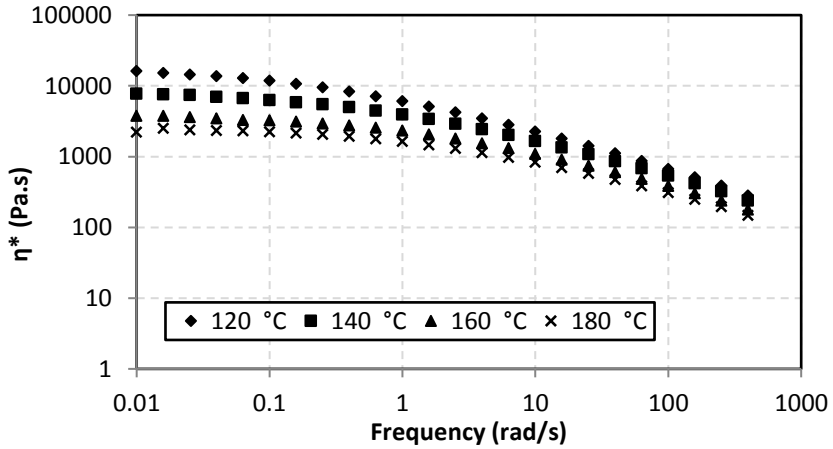

Figure 3-5: Frequency sweep test of EVA (9%VA) at different temperatures

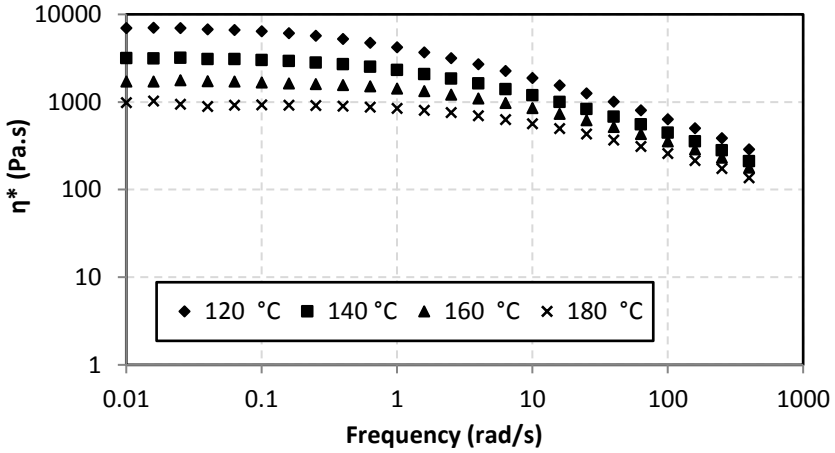

Figure 3-6: Frequency sweep test of EVA (18%VA) at different temperatures

Table 3-3: Comparison between zero shear viscosity of EVA grades

Temperature (°C)	Zero Shear Viscosity [η_0 (Pa.s)]	
	MU76000	MU76300
120	7527.8	20711.3
140	3307.7	8773.8
160	1642.6	3993.7
180	963.6	2501.7

Last, Figure 3-7 shows the variation of zero shear viscosity (η_0) with ($1/T$) for both polymers. Two conclusions can be made out of this figure. First, it is clear that the zero shear viscosity of the 18%VA grade is lower than that of the 9%VA grade. However, this difference decreases as the temperature increases. Also, the EVA grade with 9%VA is more sensitive to temperature variations than the 18%VA grade.

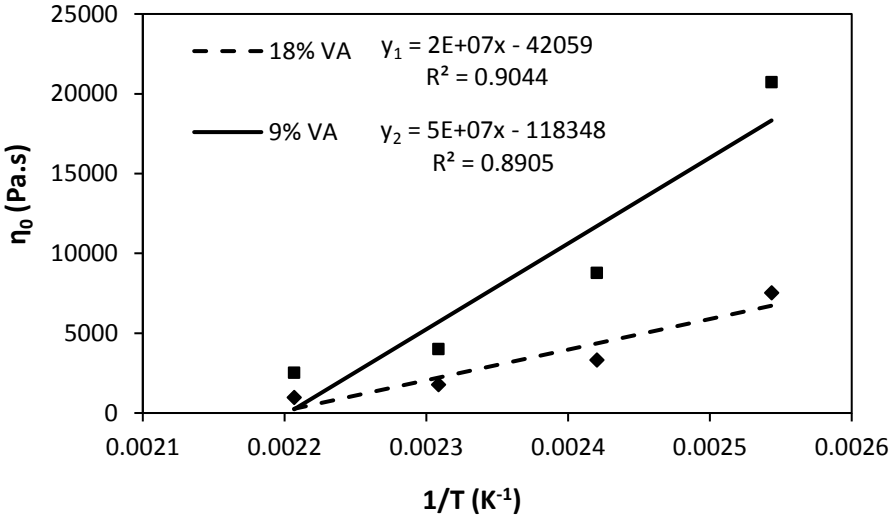

Figure 3-7: Variation of zero shear viscosity with temperature for different EVA grades

Poly(ethylene oxide) (PEO) was also purchased from Sigma Aldrich (Canada). It is a fine white powder with a viscosity average molecular weight ($\bar{M}_v$) of 192,000g/mol. The DSC and the TGA thermograms for PEO are shown in Figure 3-8 and Figure 3-9. The polymer has a melting point of 65.89°C, and it is thermally stable up to 200°C. Maximum decomposition rate occurs at 397.41°C, and almost no residues remain at 600°C.

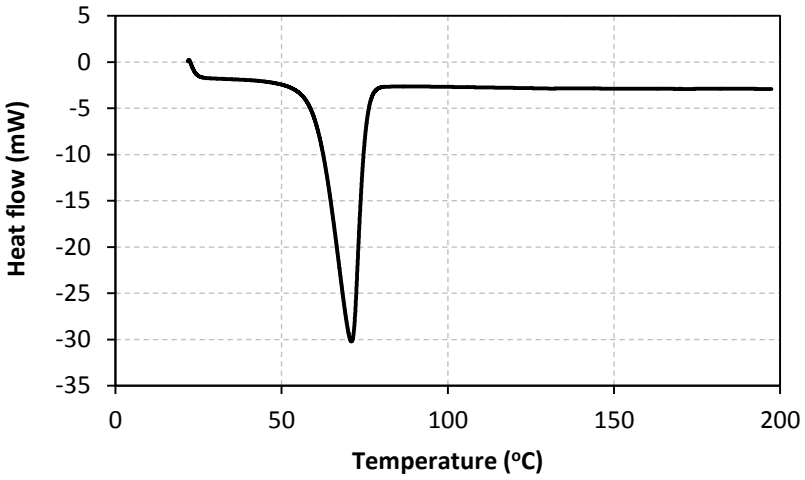

Figure 3-8: DSC thermogram of poly (ethylene oxide) polymer

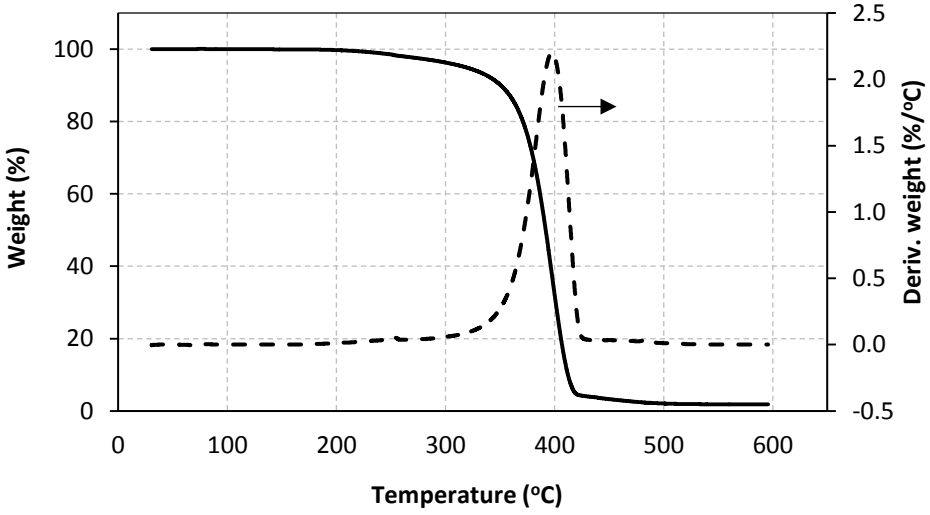

Figure 3-9: TGA thermogram of poly(ethylene oxide)

3.1.2 Chemical Blowing Agents:

4,4´-oxy bis(benzene sulfonyl hydrazide) (OBSH) purchased from CelChem LLC (USA) was utilized as chemical blowing agent. It is a white powder with density 1.53g/cm^3, and it liberates 125ml of gases per each gram of the solid material. The gaseous decomposition products consist of 91% N_2, and 9% H_2O. The thermgrams of the DSC and TGA tests conducted on the material are shown in Figure 3-10 and Figure 3-11, respectively. It is clear from these figures that Celogen OT undergoes rapid decomposition reaction over a narrow temperature range (150-175^{o}C).

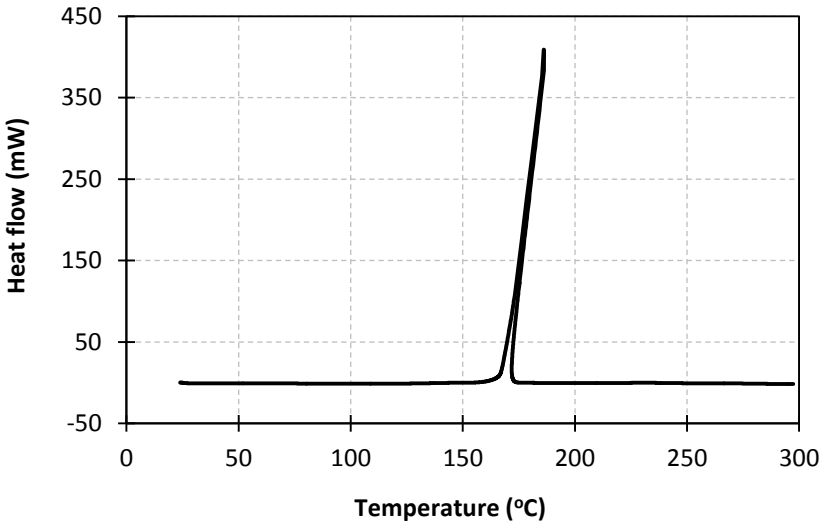

Figure 3-10: DSC thermogram of Celogen OT

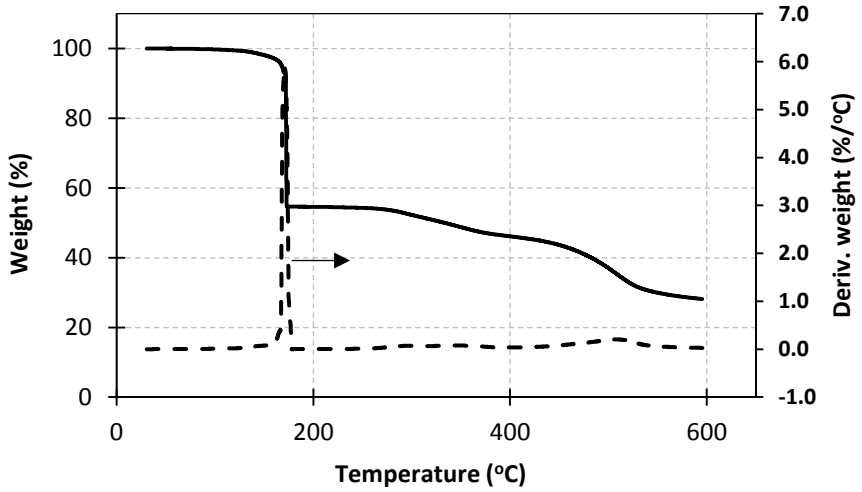

Figure 3-11: TGA thermogram of Celogen OT

3.1.3 Other Additives

Dioctyl phthalate (Sigma Aldrich, Canada) was used for the purpose of improving the dispersion of CBA, and to minimize dusting that occurs during mixing. It is a transparent viscous liquid with density of 0.985g/cm^3 at 20°C, and a boiling point of 384°C. Commercial salt (Windsor, Canada) was used in the experiments. The salt was further sieved, and separated into three different portions depending on the particle size: 106-250, 250-500, and 500-850µm.

3.2 Equipment Specifications

A bench-top manual press (Carver Inc., USA), shown in Figure 3-12, was used to mold and prefoam the polymer samples. The press has a clamping force of 12tons, and it has two 6″×6″ electrically-heated steel platens which are heated at a rate of 700watts. Each platen is fitted with a digital temperature controller that can manage temperatures up to 343ºC. The press also has a 0-24,000lb analog pressure gauge for pressure monitoring.

Figure 3-12: Carver hydraulic press

A custom-made forced convection oven, shown in Figure 3-13, was used to dry the raw materials and water-leached samples. The oven was also used to expand the molded samples under atmospheric pressure. The oven operates at temperatures up to 200ºC.

Figure 3-13: Forced convection heating oven

Four sieving trays with stainless steel mesh, shown in Figure 3-14, were used to sieve the salt and powdered polymers. The sieves have US size numbers 20, 35, 60, and 140 which are equivalent to 850, 500, 250, and 106μm, respectively.

Figure 3-14: A set of sieving trays

A set of simple molds were used in the experiments. The mold consists of two aluminum square sheets with dimensions 12×12cm^2, and a cylindrical die frame with 10.1cm diameter as shown in Figure 3-15. Four die frames with different depths were used: 3, 18, 24, and 36mm. The 3mm thick die frame was used to prepare the molded samples, while the other die frames were used to expand the molded samples in the heating oven. The selection between these die frames depends on the expansion ratio required. The 36mm thick die frame corresponds to an expansion ratio of 12, while the 18mm thick die frame is used to achieve expansion ratio of 6.

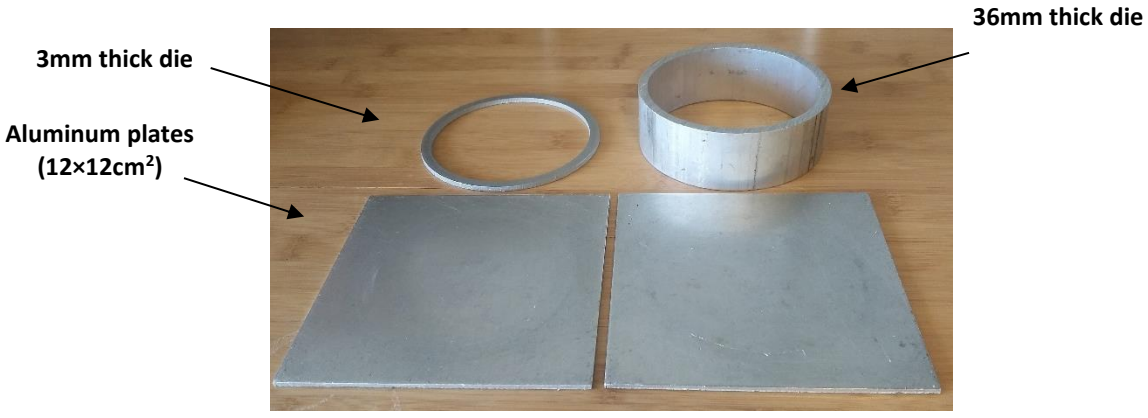

Figure 3-15: Die frames and aluminum sheets used in the experiments

3.3 Cellular Structure Characterization Using X-ray Computed Tomography

3.3.1 Introduction

X-ray microcomputed tomography (micro-CT) is a non-destructive technique with the capability of capturing the 3D view of the internal structure of materials [131]. The advent of the technique was originally for medical diagnosis purposes but recently it is being employed in diverse fields for the sake of characterizing the 3D internal structure of different materials. Among these are composites [132-136], food products [137-139], metal foams [140-144], biological tissues/bones [145-149], rocks [150-153], and ceramic foams [140, 154, 155].

The cellular structure of foams is typically analyzed by 2D imaging techniques such as scanning electron microscopy and optical microscopy [156-158]. Conclusion about 3D structure cannot be made based upon 2D imaging techniques for a good number of reasons. First, object size in 2D is not equivalent to its actual size. This is because 2D size results from the intersection of a sectioning plane with the object. According to this statement, the 2D size of a spherical object will vary from a maximum value at the equator to a minimum value at the poles as shown in Figure 3-16.

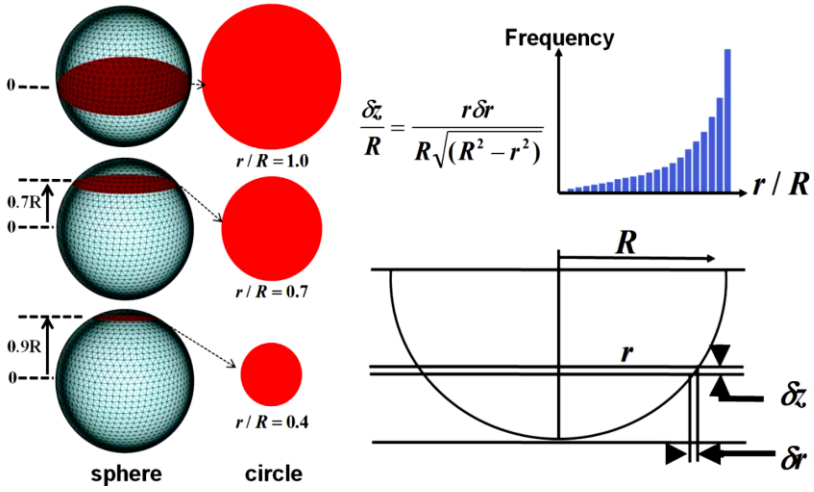

Figure 3-16: Random sectioning of a sphere produces a distribution of circle sizes, which can be calculated from analytical geometry [159]

Moreover, the object size distribution obtained from 2D imaging is not realistic, as it contains more of larger objects and less of smaller objects compared to the true distribution. This occurs because the frequency of intersection with the cutting plane is higher for larger objects than for smaller ones. Last, despite total porosity remains almost unchanged between 2D and 3D analysis, open and closed porosity in 2D are always different from these extracted by 3D analysis. This can be visualized with the aid of Figure 3-17; the cylindrical cell that is viewed as closed in 2D view is connected at the top and at the bottom to other neighboring cells in 3D view. Consequently, 2D closed porosity results are always overestimated at the cost of open porosity, which in turn becomes underestimated.

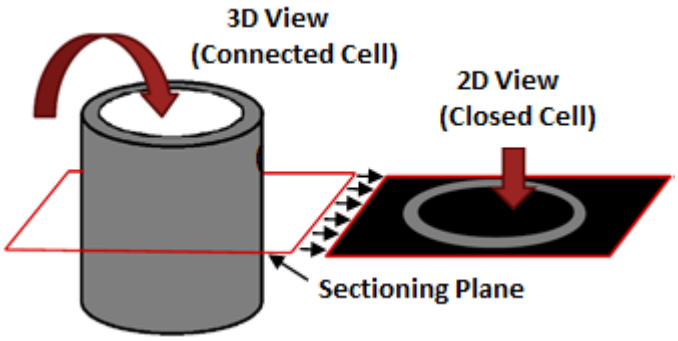

Figure 3-17: Visualization of opened cylindrical pore in 2D and 3D [160]

3.3.2 Fundamentals of microtomography

When an X-ray beam passes through an object, it undergoes attenuation, by scattering and absorption, according to Beer's law [161]:

$$X = X_0 \exp\left[-\beta L\right] \tag{3.1}$$

where X_0 and X are the intensities of the incident and transmitted X-ray beams respectively, β is the linear attenuation coefficient of the material, and L is the length of the optical path. If the scanned object consists of a number of different materials, the equation becomes:

$$X = X_0 \exp\left[\sum_i (-\beta_i L_i)\right] \tag{3.2}$$

Where β_i is the attenuation coefficient of material i, and L_i is the length of light path across material i. When an object is irradiated by an X-ray source, a two-dimensional shadow image (radiograph) is formed as shown in Figure 3-18. For a parallel X-ray illumination, each line in the shadow image contains the integration of all attenuation information of an equivalent cross-section. To obtain the attenuation information for each point within each cross-section, a back projection algorithm is used. To this end, a sufficient number of radiographs is needed to compute the 3D attenuation map for the scanned object. Normally, a 180° scan is adequate to obtain a large number of radiographs that can be used by the back projection algorithm to reconstruct the cross-sections precisely [162].

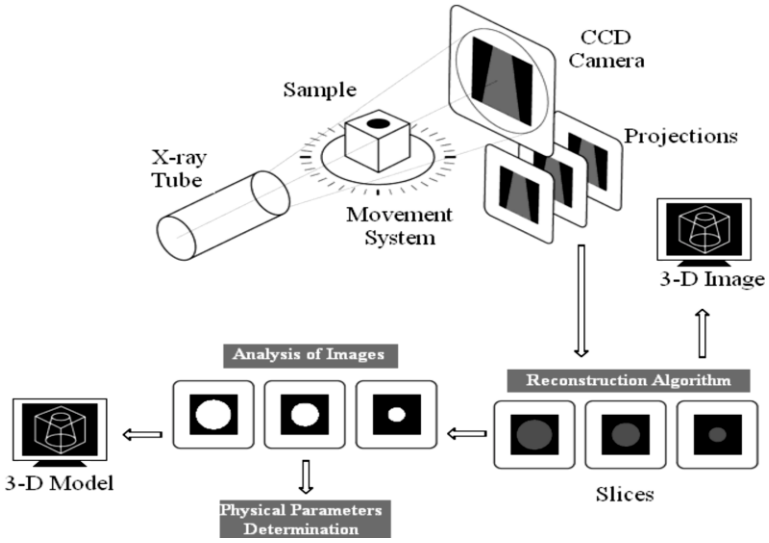

Figure 3-18: Illustrative scheme of the acquisition, reconstruction, analysis and 3D model generation [163]

3.3.3 Equipment specifications

The high resolution X-ray scanner model 1172 from Bruker (Belgium) shown in Figure 3-19 was utilized in the study to analyze the cellular structure of the developed foams. The specifications of the instrument are given in Table 3-4. The equipment is provided with NRecon software for reconstructing cross-sectional images, CTan software for characterizing cellular structure and creating 3D models. The equipment is also fitted with CTvol software which is used to manipulate the generated 3D models. In addition to

CTan software, an open source image processing platform ‘Imorph’ was utilized to compute tortuosity, and the average diameter of the throats that connect adjacent cells.

Figure 3-19: Desktop SkyScan 1172 micro-CT

Table 3-4: Specifications of micro-CT scanner model 1172

X-ray source	20-100kV,10W,<5 µm spot size
X-ray detector	11Mp, 12-bit cooled CCD fiber-optically coupled to scintillator
Detectability	0.5µm at highest resolution
Reconstruction	hierarchical (InstaRecon®) and GPU-accelerated FDK reconstruction as standard

3.3.4 Sample preparation and mounting

Unless stated elsewhere in the thesis, three cylindrical specimens with 12mm diameter×14mm height were cut from each one of the sample replicates using a sharp circular cutting tool shown in Figure 3-20. Each specimen was then firmly fixed on the sample holder shown in Figure 3-21 using a super glue.

Figure 3-20: Circular cutting tools set with different diameters

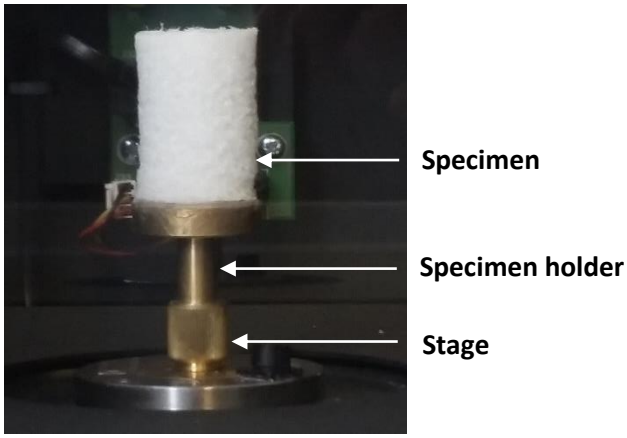

Figure 3-21: Image showing a specimen fixed on the sample holder

3.3.5 Scanning procedure

Alignment procedure was carried out before running the scan to make sure that the X-ray source, X-ray camera, and stage are aligned along the optical axis. After that, the sample was tightly fixed to the center of the sample holder. This step is very important to obtain good images; loose fixation, and/or off-center positioning will result in image artifacts, which in turn deteriorate the quality of the image. The voltage was adjusted in such a way that good contrast between the sample and the background is achieved. The sample was then removed, and the background was updated, by acquiring a new flat-field correction for the new settings. Last, the sample was inserted again and the scan was started. A 180° scan was performed at 104μA and 20kV, with a rotational step of 0.25° and frame averaging of 5. The pixel size was set to 10.41μm unless stated elsewhere in the thesis.

3.3.6 Image reconstruction, image processing and structure analysis

After completion of scanning process, the shadow images shown in Figure 3-22(a) were opened in NRecon software to convert them into gray scale cross-sectional images which are shown in Figure 3-22(b). After that, the gray scale reconstructed images were opened in CTan Software, and a cylindrical volume of interest with dimensions 16mm diameter × 8.33mm height, was selected inside each specimen producing 800 images each with a resolution of 1536×1536 pixels. Afterwards, a thresholding range was carefully

selected (between 4 and 255) to convert these gray scale images into binarized images, shown in Figure 3-22(c). The thresholding range was selected in such a way that the original images details remained captured. The binarized images were further processed to improve their quality producing the post-processed images, shown in Figure 3-22(d).

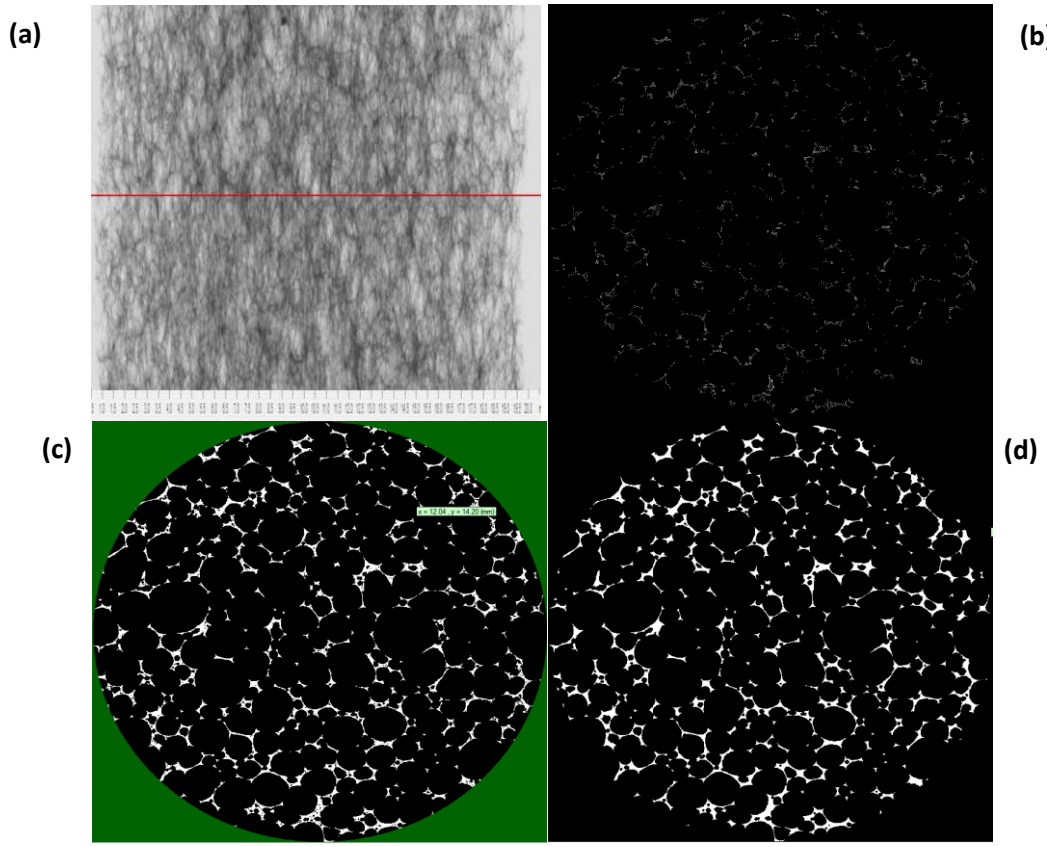

Figure 3-22: Sequence of image processing: (a) shadow image, (b) gray scale image, (c) binarized image, and (d) processed image

A sequence of custom-process operations were performed in 3D space to extract the morphological properties of the developed foam samples. The sequence of steps used are listed in Table 3-5. The thickness size distribution of the cell walls were calculated using the sphere-fitting algorithm provided by CTan software, and the results were reported as volume percentage [164-166]. The same algorithm was used to calculate the volume-weighted average cell size and cell size distribution of the developed foams. Last, the processed images were saved, and exported to the open source, Imorph software, to

calculate the number-weighted average cell size, cell size distribution, tortuosity and average diameter of the throats, by applying some built-in modules [167-170].

Table 3-5: A list of processes used to analyse the cellular structure of the developed foams

Process group	Sub-process	Function
Thresholding	Global (4-255)	Binarize images
Despecle	Sweep all except the largest object (3D)	Clean the solid skeleton by removing isolated objects
Despecle	Remove pores (3D)	Remove closed pores
Save bitmap	Save bitmap	Save processed images
3D Analysis	3D Analysis	Analyze open porosity, closed porosity, total porosity, number of closed cells, strut thickness (based on volume) in 3D
3D model	3D model	Create 3D model for the solid skeleton
Bitwise Operations	Image=not image	Invert images
Bitwise Operations	Image=image and ROI	Limit the image to ROI
3D Analysis	3D Analysis	Calculate the average cell size and cell size distribution (based on volume) in 3D
Morphological Operations	Watershed (3D)	Segment the open porosity volume
Individual object Analysis	Individual object Analysis (3D)	Calculate the number of cells, the average cell size, and the cell size distribution (based on number) in 3D

3.3.7 Verification study

Some of the images details, especially at the boundaries where the color depth is close to that of the background noise, may be lost if thresholding, and subsequent image processing steps were not selected properly. This will eventually result in an overestimation of the measured open porosity. So it is very important to verify that thresholding and image processing steps were done properly. To this end, the open porosity of two different foam samples, prepared with two different EVA grades, 9%VA and 18%VA, was measured using a gas pycnometer (Ultra pycnometer 1000, Quantachrome Instrument) shown in Figure 3-23 in accordance with the ASTM D6226 standard, and the results were compared with these obtained from the micro-CT method [171]. In gas pycnometer experiments, the samples were pressurized with nitrogen gas at 6psi and the instrument measured the closed

volume that cannot be accessed by the gas. Open porosity was then calculated according to the following equation:

Figure 3-23: Image of Ultra Pycnometer 1000

$$\%open\ porosity = \left[1 - \left(\frac{V_c}{V_g}\right)\right] * 100 \tag{3.3}$$

where V_c is the inaccessible volume, and V_g is the geometric volume of the sample. The measurements were conducted on five different replicates of each sample, and the average of the results is listed in Table 3-6. It is clear that the open porosity values measured by the gas pycnometer for both samples were in good agreement with those obtained from micro-CT method. This manifested that the thresholding range was correctly selected, and no image details have been lost after performing image post processing.

Table 3-6: Porosity results obtained by different measuring methods

Sample Type	**Method**	**Open Porosity**	
		Mean (%)	**Std. Dev. (%)**
MU76000	Micro-CT technique	91.18	1.13
	Gas pycnometer	90.66	0.64
MU76300	Micro-CT technique	90.58	1.18
	Gas pycnometer	89.14	0.47

3.4 Measurement of Static Air Flow Resistivity

An in-house setup was constructed in accordance with ASTM C522 to measure the static air flow resistivity of the developed foams. The basic components of the measuring setup is shown schematically in Figure 3-24. In this test, the volumetric flow rate (Q) was measured by air rotameter (model FL-3404G, OMEGA), while the pressure difference across the sample (ΔP) was measured by a portable digital manometer (model HT-1890).

Given the surface area (S) and the thickness (d) of the sample, static air flow resistivity was calculated by the following equation [172]:

$$\sigma = \frac{\Delta P \times S}{Q \times d} \tag{3.4}$$

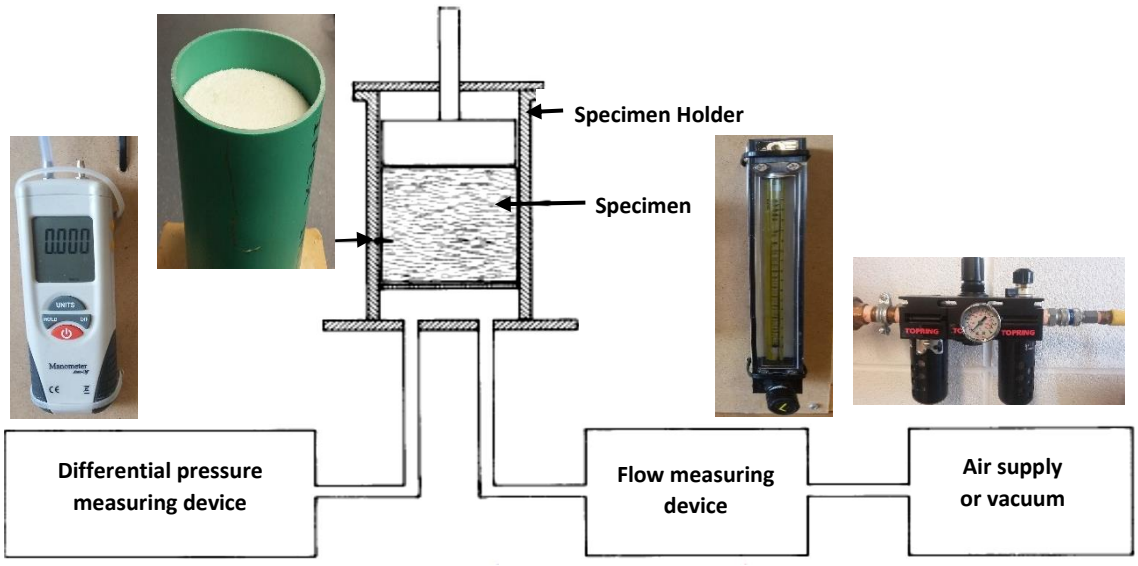

Figure 3-24: Schematic diagram of air flow resistivity apparatus

3.5 Acoustic Characterization of Foams

3.5.1 Introduction

From the perspective of acoustic engineers, absorption coefficient is the most important properties of any acoustic material. According to it, acoustic materials are classified as absorptive or reflective [173]. There are three standardized measurement methods which can be used to measure absorption coefficient: reverberation chamber (ISO

354) [174], standing wave ratio (ISO 10534-1) [175], and transfer-function method (ISO 10534-2) [176]. Unlike impedance tube methods (ISO 10534-1 and ISO 10534-2), which measure absorption coefficient at normal incidence angles, reverberation chamber can measure absorption coefficient at random incidence angles accurately. Nevertheless, the method requires a special installation and a considerable space to locate it (room volume is at least $300m^3$). Also the tested samples are large, having an area of $12m^2$ [177].

3.5.2 The transfer function method (ISO 10534-2)

The transfer function method is simple, and its setup is small and portable. Most importantly, it uses small size samples for the tests. The apparatus, shown in Figure 3-25 consists of a rigid-walled straight tube with a sound source at one end and a sample holder to place the tested material at the other tube end. The method is more time-saving than the standing wave ratio method, as it uses two microphones and white noise to measure the absorption coefficient at all frequency simultaneously instead of sweeping the frequency range, using a sine wave noise, and measuring the absorption coefficient at each frequency one by one [178, 179].

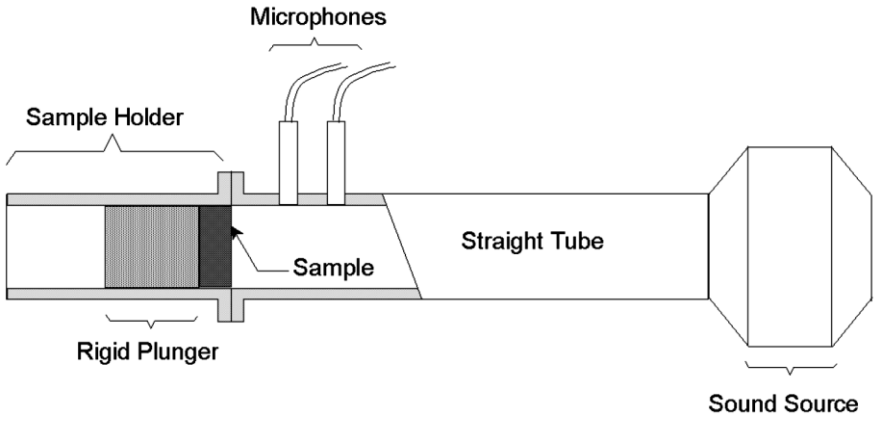

Figure 3-25: The Two-Microphone Method [180]

The set-up for the transfer function method is shown schematically in Figure 3-26. A loudspeaker at one end of the tube is connected to a signal generator, through an amplifier, to produce random noise in the desired frequency range. The test sample is mounted at the other end of the tube inside the specimen holder. Plane sound waves are

generated in the tube by the loudspeaker and the sound pressures (magnitude and phase) are measured at the locations of the two microphone. The microphones are connected to a data acquisition system, which in turn is connected to a digital frequency analyzer. The complex transfer function of the two microphones is determined and used to compute the reflection coefficient using the following equation:

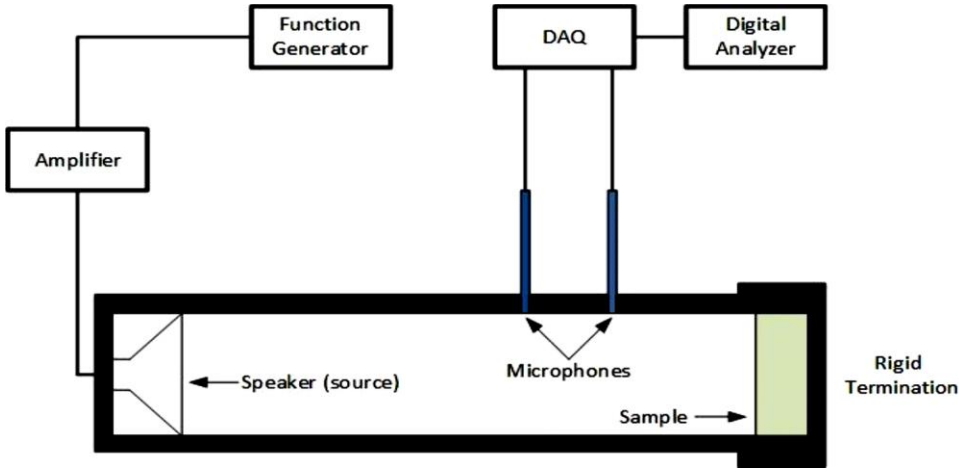

Figure 3-26: Schematic of the impedance tube set up for acoustic absorption [181]

$$R = \frac{H_i - H_{12}}{H_{12} - H_r} e^{2j\bar{k}M} \tag{3.5}$$

And the absorption coefficient can be obtained from the following equation:

$$\alpha = 1 - |R|^2$$

where H_{12} is the transfer function from microphone 1 to microphone 2, H_r and H_i are the real and imaginary parts of H_{12} respectively, M is the distance between the sample surface and the farther microphone, $j = \sqrt{-1}$, and $\bar{k}$ is the wavenumber.

3.5.3 Impedance tube design

A custom-made impedance tube shown in Figure 3-27 was constructed to measure the normal sound absorption coefficient (α) in accordance with ASTM E1050. The tube is made from PVC and it has a diameter of 10.06cm. The upper cut-off frequency of the tube is given by [181]:

$$f_u < \frac{0.58c_0}{D} \tag{3.6}$$

According to the above equation, the upper cut-off frequency of the tube was 2000Hz. The length of the tube should be greater than three times its diameter, to allow developing plane sound waves. Therefore the tube length was set sufficiently long (130cm) to meet this condition. A speaker, supporting frequencies down to 100Hz, was firmly attached to the tube from one side, and a rubber gasket was placed between the speaker and the tube to prevent any leakage, and to dampen any vibrations that may be transmitted from the speaker. The speaker was also enclosed by a wooden enclosure lined with an absorptive material to prevent airborne flanking transmission to the microphones. Three holes were drilled in the tube to accommodate three flush mount 1/4" microphones. Three holes were drilled to give three different two-microphone configurations. Each configuration can measure accurately over a specified frequency range. The measuring frequency range of each configuration depends on the spacing between the two microphones (q), and its limits are given by [178]:

$$f_l > \frac{0.05c_0}{q} \tag{3.7}$$

$$f_u < \frac{0.45c_0}{q} \tag{3.8}$$

The spacing of each configuration and the corresponding measuring frequency range are given in Table 3-7. It is noteworthy that the hole labelled (1) was set at a distance larger than three times the diameter of the tube, to dissipate any cross modes that may arise from the speaker. Furthermore, the hole labelled (3) was set at a distance roughly equal to the tube diameter to dissipate any cross modes that may arise after reflection of sound at the surface of the sample.

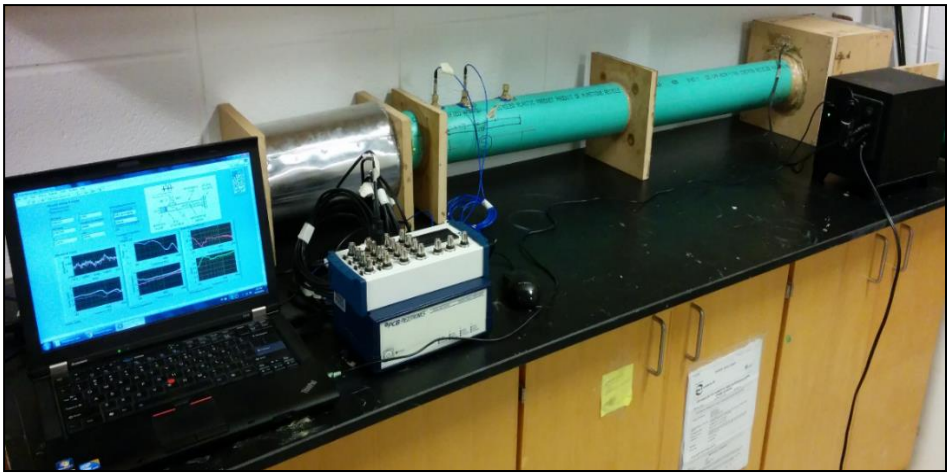

Figure 3-27: An image of the setup used to measure the normal sound absorption coefficient

The sample holder was made from stainless steel and it consists of a cylinder and a moving piston. The thickness of the piston was set to 5cm to provide infinite acoustic impedance. The sample holder was coupled to the impedance tube by interference, with the aid of Teflon tape, to prevent any leakage. The schematic diagram of the impedance tube is shown in Figure 3-28, whereas, the tube dimensions, the microphones spacing, and the corresponding measuring frequency ranges are given in Table 3-7.

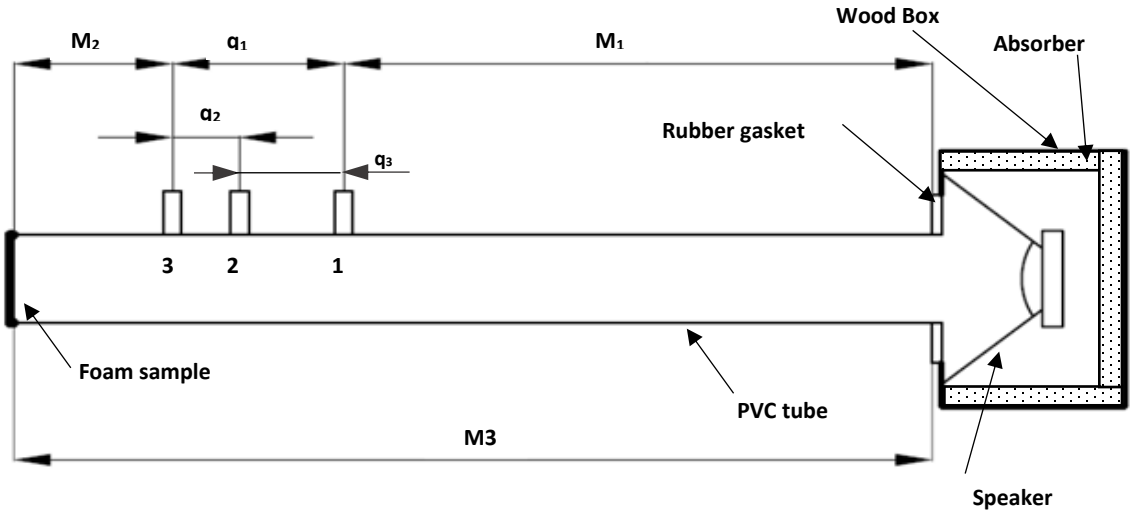

Figure 3-28: Schematic diagram showing the characteristic dimensions of the impedance tube

Table 3-7: Impedance tube dimensions and its measuring frequency ranges

Impedance Tube Dimensions			
Designation	**Dimension Definition**		**Length (cm)**
D	Tube diameter		10.06
M_3	Tube length		130.0
M_1	Distance between speaker and position 1		103.5
M_2	Distance between sample and position 3		10.3
Microphones Spacing and the corresponding Frequency Range			
Configuration	**Microphones Positions**	**Spacing (cm)**	**Frequency (Hz)**
q_1	1&3	17.2	100-892.7
q_2	2&3	7.2	244-2000
q_3	1&2	10.0	171.5-1543.5

A LabVIEW VI shown in Figure 3-29 was developed to operate the impedance tube, and to measure the acoustic parameters of the developed foams samples including sound absorption coefficient, sound reflection coefficient, and normalized surface impedance. Microphones calibration and microphone phase mismatch correction were conducted before running the measurements, and the speaker were turned on for 10 minutes before running the test to make sure that the temperature inside the tube has leveled off [182, 183].

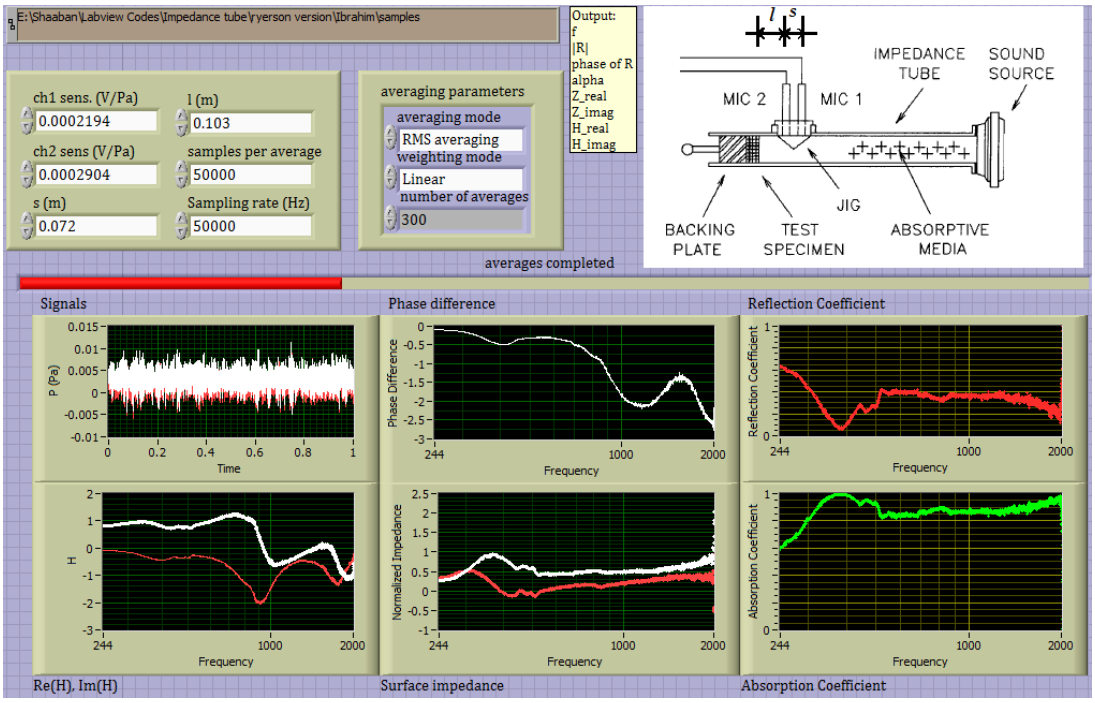

Figure 3-29: The LabVIEW User Interface used for Acoustic Measurements

3.5.4 Validation study

To validate the design, the impedance tube has been used to measure the reflection coefficient of unflanged open end circular tube, and the measurements were compared with the theoretical values. Theoretically, the reflection coefficient of unflanged open end circular tube is given by the following polynomial [184]:

$$R = 1 + 0.01336(\bar{k}a) - 0.59079(\bar{k}a)^2 + 0.33576(\bar{k}a)^3 - 0.06432(\bar{k}a)^4 \qquad (3.9)$$

where R is the magnitude of the reflection coefficient, a is the radius of the tube, and $\bar{k}$ is the wave number ($= 2\pi f/c$). As indicated in Figure 3-30, the measurements are in good agreement with the theoretical values over the measuring frequency range.

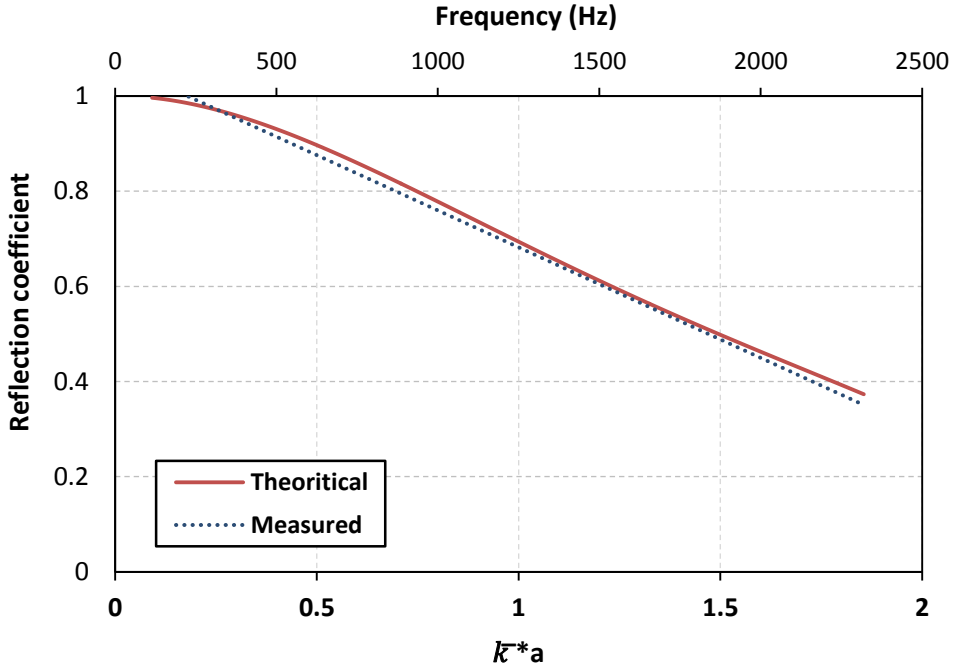

Figure 3-30: Measured reflection coefficient of open end circular tube compared to the theortical values

Chapter 4 Investigating the Effect of Cell Size on Sound Absorption Over the Measuring Frequency Range

4.1 Introduction

The aim of this set of experiments is to study the effect of cell size on sound absorption over the frequency range 100-2000Hz. The effects of adding air gap and foil facing on the acoustic performance of the developed foam samples were investigated as well. The melt molding/particulate leaching method was employed to prepare thick foam samples (2 and 3cm) with different cell sizes. The commercial salt, Windsor (Canada), was used in the experiments. The salt was sieved, according to the particle size, into three different portions: 106-250, 250-500, and 500-850μm. The nomenclature of the developed foam samples is given in Table 4-1.

Table 4-1: Nomenclature of samples prepared by salt leaching method

Sample code	Salt size range (μm)
SS	106-250
MS	250-500
LS	500-850

4.2 Experimental Work

An EVA grade with VA content of 9% was first sieved through the 250μm sieve. Afterwards, specified amounts of the polymer and the salt, as given in Table 4-2, were gently mixed to prevent fracturing the salt granules. The mixture was then transferred into a circular aluminum mold consisting of a circular die with 10.1cm diameter frame and two aluminum plates with 3mm thickness. The salt-polymer mixture was compression molded for 20 min using carver hydraulic press. The heating cycle applied was as follows: first heating the mixture at 160^{o}C without applying any pressure for 10 min followed by heating at the same temperature under a pressure of 2000 psi for 10 min. In the last step, the mold was removed from the press and air cooled. The molded sample was carefully removed

from the mold and immersed in water for 2 days to dissolve the salt. Last, the leached foam samples were dried in a heating oven at 60^{o}C for 6 hrs.

Table 4-2: Compositions used to prepare foam samples by salt leaching method

Die frame depth (cm)	2	3
Polymer Amount (g)	18.9	28.3
Salt Amount (g)	188.8	283.2
Total Amount (g)	209.7	314.5

Figure 4-1: Image of foam sample designated as MS; sample thickness: 2 and 3cm

4.3 Results and Discussion

4.3.1 Cellular structure characterization

The characteristics of the developed cellular structures are given in Table 4-3, while Figure 4-2 shows the 3D models of the cellular structures developed after leaching the salt. It is clear that open porosity did not change between samples, and it was around 88%. This is attributed to the fact that porosity achieved by this method depends on the amount of salt, which was the same for all samples. Moreover tortuosity, which is a measure of the complexity of the cellular structure, did not change from one sample to another, and it had values around 1 (i.e. between 1.15 and 1.23).

Table 4-3: Results of structure analysis for samples prepared by salt leaching method

Property	Foam sample		
	SS	MS	LS
Open porosity (%)	88.07±0.37	88.75±0.49	87.08±0.83
Cell density (cell/cm^3)	1.07×10^5 (±1200)	2.53×10^4 (±1350)	2.04×10^4 (±1356)
Cell size (μm)	251±20	433±25	462±23
Throat diameter (μm)	60.78±9	84.89±7	97.64±8
Tortuosity (-)	1.15 ± 0.05	1.19 ± 0.07	1.23 ± 0.08

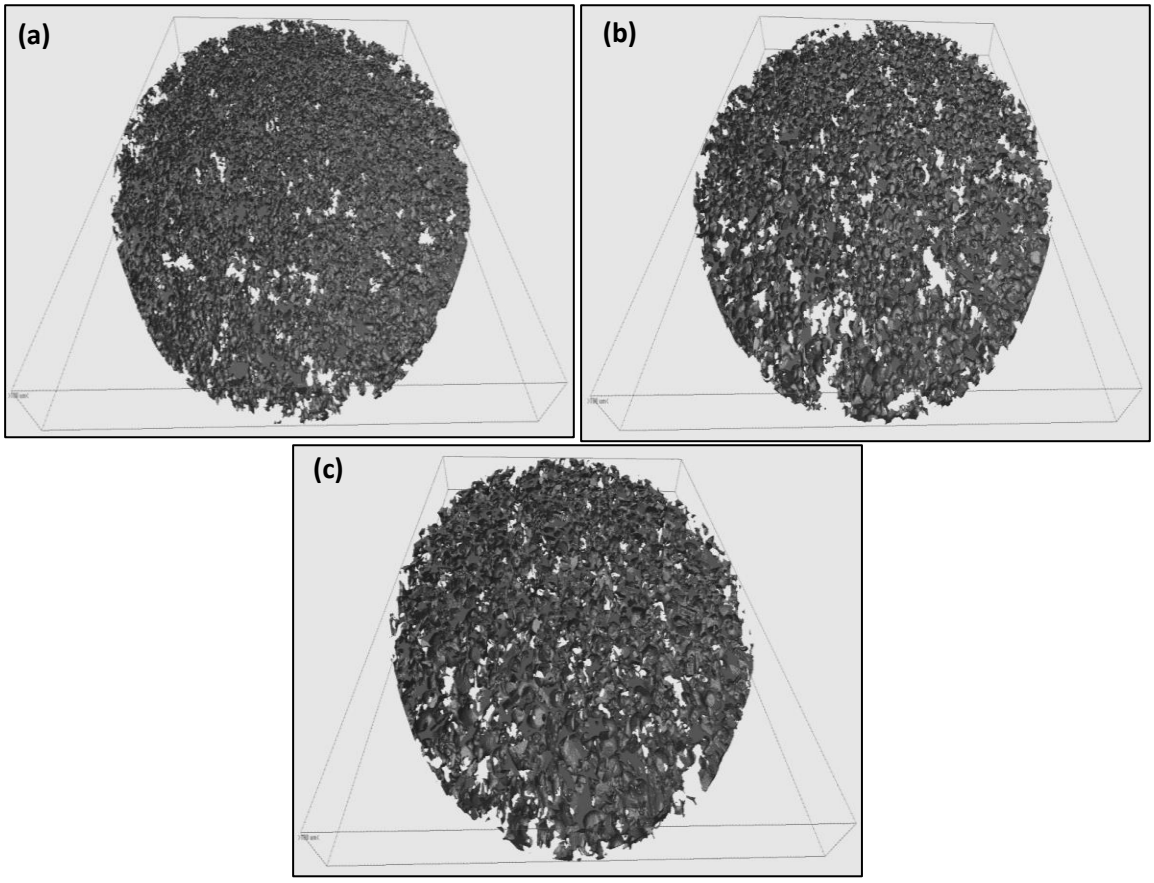

Figure 4-2: 3D models of the foam samples designated as: (a) SS, (b) MS, and (c) LS

The volume-weighted cell size distributions of the foam samples are shown in Figure 4-3, Figure 4-4, and Figure 4-5. It is clear that the distribution shifted to the right as the salt size increased. However, the cell size distribution of the foam sample designated as LS did not change significantly from that of the sample designated as MS. In fact, the cell size distribution of all foam samples did not match the size range of the salt particles due to the occurrence of breakage and agglomeration. Since salt granules are fragile, they undergo inevitable fracturing during the mixing and the compression steps leading to the formation of smaller cell sizes. On the other hand, when the number of salt particles is very large, the salt particles tend to agglomerate leading to the formation of larger cell sizes.

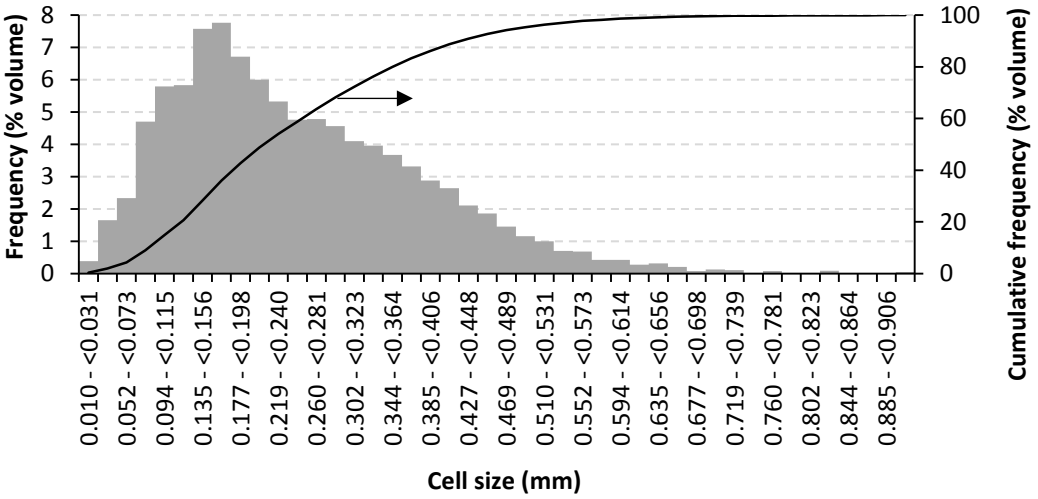

Figure 4-3: Volume-weighted cell size distribution of the foam sample designated as SS

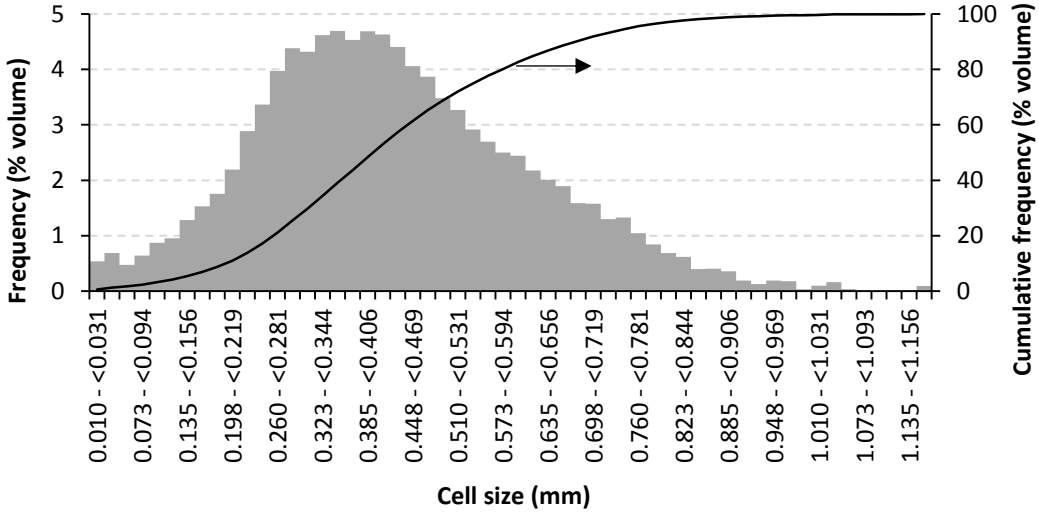

Figure 4-4: Volume-weighted cell size distribution of the foam sample designated as MS

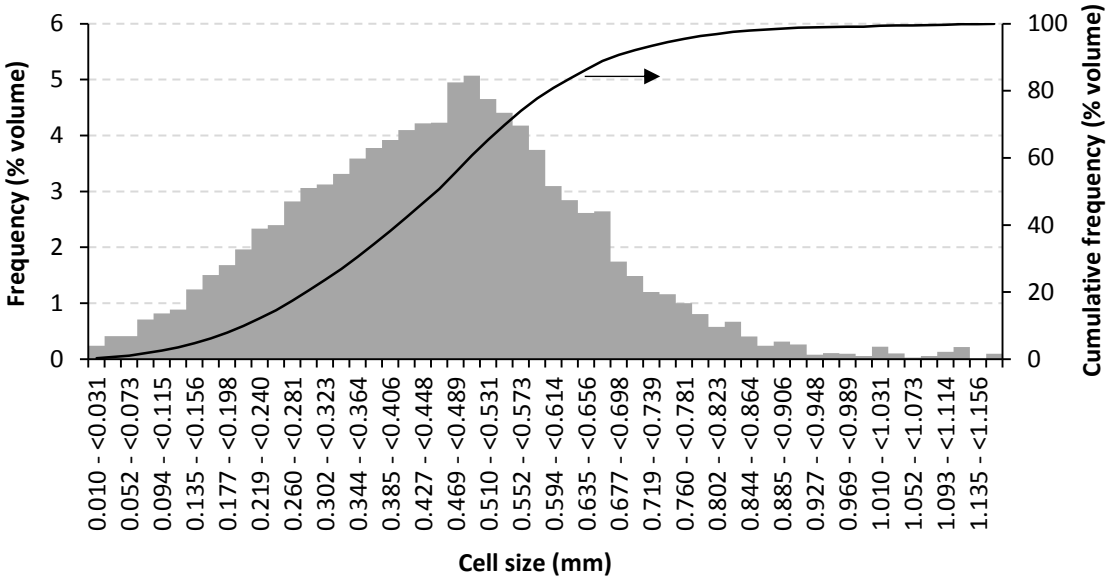

Figure 4-5: Volume-weighted cell size distribution of the foam sample designated as LS

It turns out from Table 4-4 that salt agglomeration is more dominant in the sample designated as SS where 41% of the volume has cells with sizes greater than the salt size range. On the contrary, salt breakage is more dominant for the sample designated as LS where almost 60% of the volume has cells with sizes smaller than the salt size range. For the sample designated as MS, 31% of the volume has cells with sizes greater than salt size range and 17% of the volume has cells with sizes smaller than the salt size range.

Table 4-4: Percentage volume of each cell size range

Cell size range	**Cumulative frequency (%volume)**		
	SS	**MS**	**LS**
<250µm	58.84	17.17	14.60
250-500µm	36.51	51.64	46.17
500-850µm	4.58	29.28	37.23
>850µm	0.07	1.92	2.00

As shown in Figure 4-6, the average cell sizes of the samples designated as MS and LS were very close (433µm and 462µm respectively). Whereas, the average cell size of the sample designated as SS was smaller, and it had the value of 251µm.

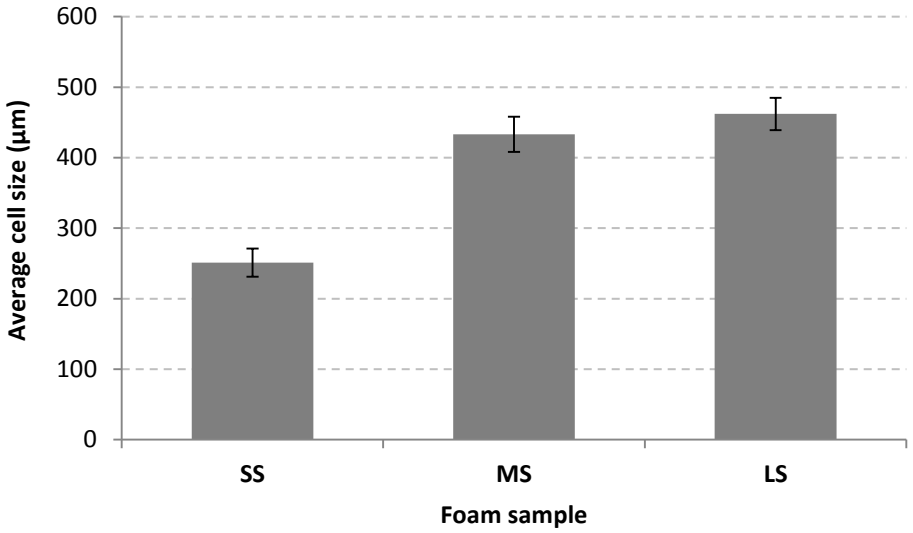

Figure 4-6: Effect of salt size on the distribution width and average cell size of the developed foam samples

Figure 4-7 shows that the cell density of the sample designated as SS was an order of magnitude higher than these of the samples designated as MS and LS, which had very close values. This is mainly related to the inverse relationship between the size of the salt particles and their number. Therefore, the sample designated as SS, which was prepared by the smallest salt size, had the highest cell density. The occurrence of salt breakage and salt agglomeration in the samples designated as MS and LS outweighed the cell density difference between them leading to similar results.

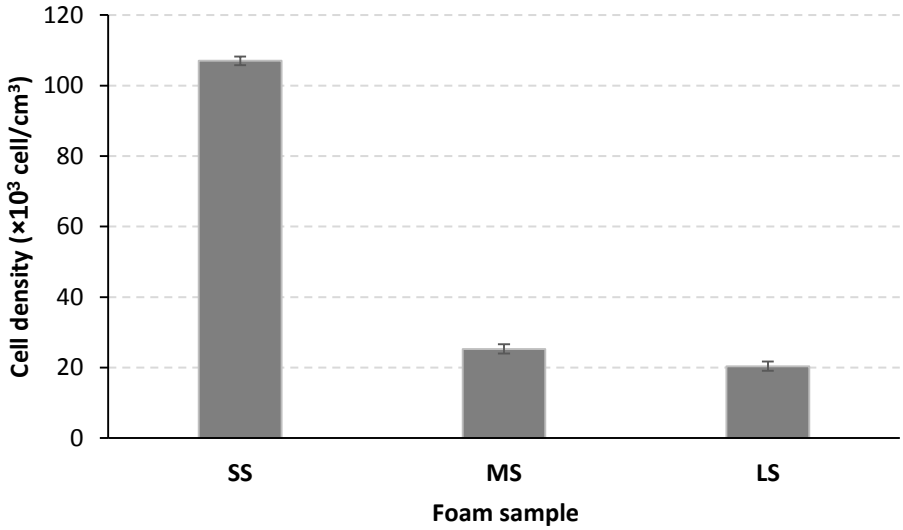

Figure 4-7: Effect of salt size on the cell density of the developed foam samples

The results shown in Figure 4-8 indicate that the average throat size decreased as the salt size decreased. The average throat size was 60.78µm for sample designated as SS compared to 84.89µm for the sample designated as MS, and 97.64 µm for the sample designated as LS.

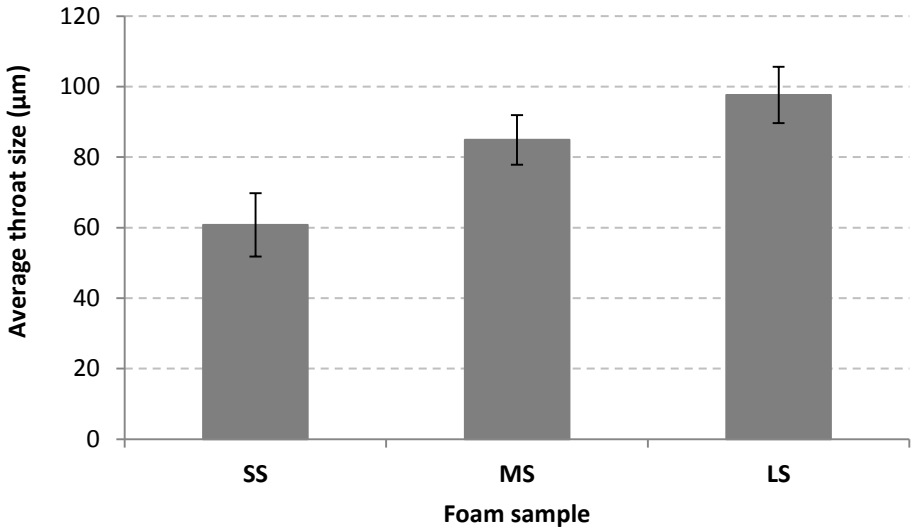

Figure 4-8: Effect of salt size on the distribution width and average throat diameter of the developed foam samples

4.3.2 Acoustic measurements

The sound absorption curves of the developed foam samples over the frequency range 100-2000Hz are displayed in Figure 4-9. Each curve represents the average of five different measurements with a standard deviation of ±0.05. It is clear that all the curves have the shape of high pass filter, which is a characteristic of homogeneous passive absorbers. For all samples, the absorption coefficient was less than 0.4 below 500Hz, whereas it was greater than 0.8 over the frequency range 900-2000Hz. The sound absorption coefficient was almost the same for all samples for frequencies up to 1000Hz, but the sample designated as SS had higher absorption coefficient than that of the other two samples above 1000Hz.

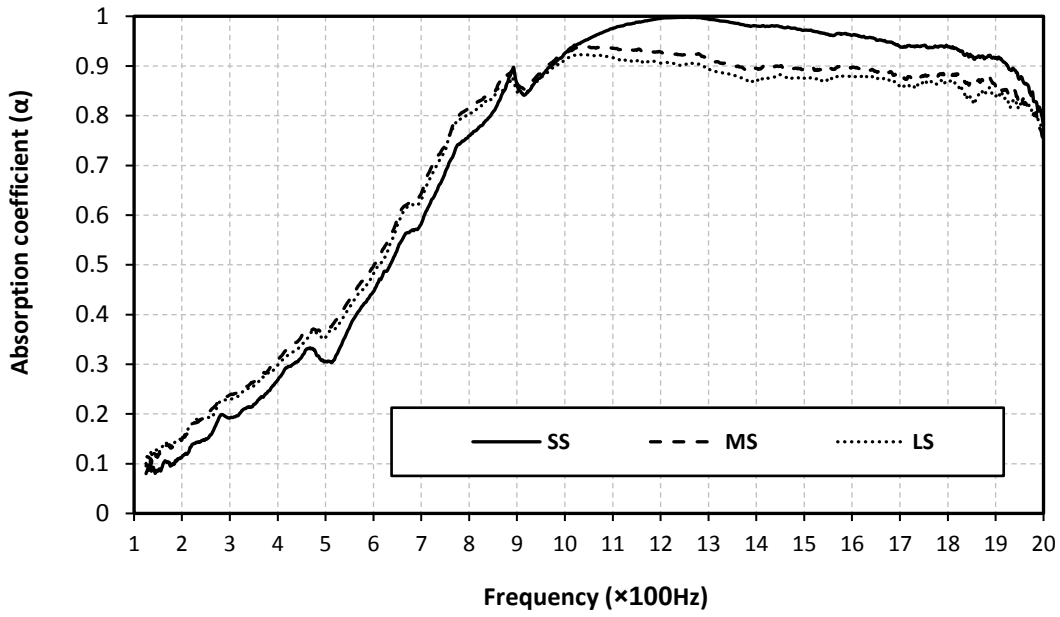

Figure 4-9: Sound absorption curves of the developed foam samples; sample thickness=5cm

The acoustic performance of the developed foam samples is mainly governed by the cellular structure and the air flow resistivity of the developed samples. Figure 4-10 shows the air flow resistivity of the developed foam samples. Since the porosity, the cell size, and the throat size were almost the same for the two samples designated as MS and LS, the air flow resistivity did not change and their absorption curves were almost the same. The decrease in cell size and throat size of the foam sample designated as SS increased the air flow resistivity and improved sound absorption for frequencies above 1000Hz.

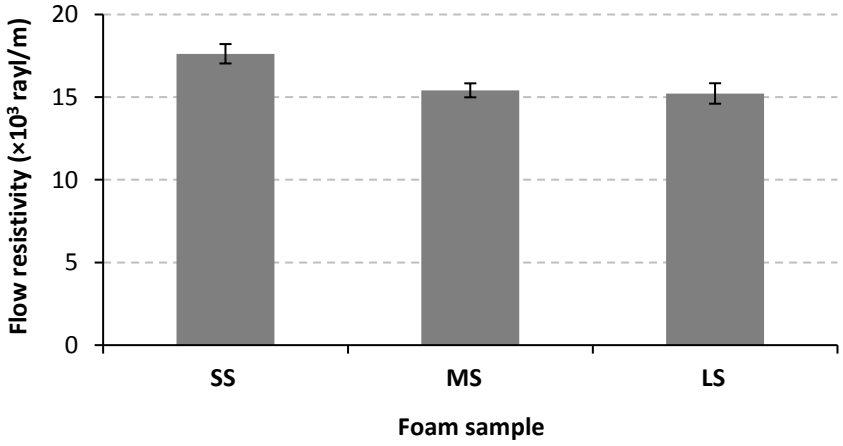

Figure 4-10: Effect of salt size on the air flow resistivity of the prepared foam samples

The acoustic performance of the foam sample designated as MS was evaluated after combining it with 6cm air gap and/or impervious aluminum foil facing. Household aluminum foil, with 0.01mm thickness and 0.027kg/cm^2 mass surface density, was utilized in the experiment. The results of these experiments are shown in Figure 4-11. It is obvious that these modifications increased the absorption peaks and shifted the absorption curves to lower frequencies leading to improvement of sound absorption over the low frequency range. Aluminum foil facing acted as membrane resonator, and it moderately improved sound absorption for frequencies below 1000Hz. Moreover, the absorption curve was characterized by a flat absorption peak around 850Hz. Adding an air gap with 6cm thickness significantly increased sound absorption coefficient by more than 3 times for frequencies below 800Hz, and the absorption peak appeared at 550Hz. The simultaneous addition of the foil membrane and the air gap shifted the absorption peak to 500Hz. Moreover, the coupling of the foil membrane and the air gap introduced a second flat peak centered around 1600Hz.

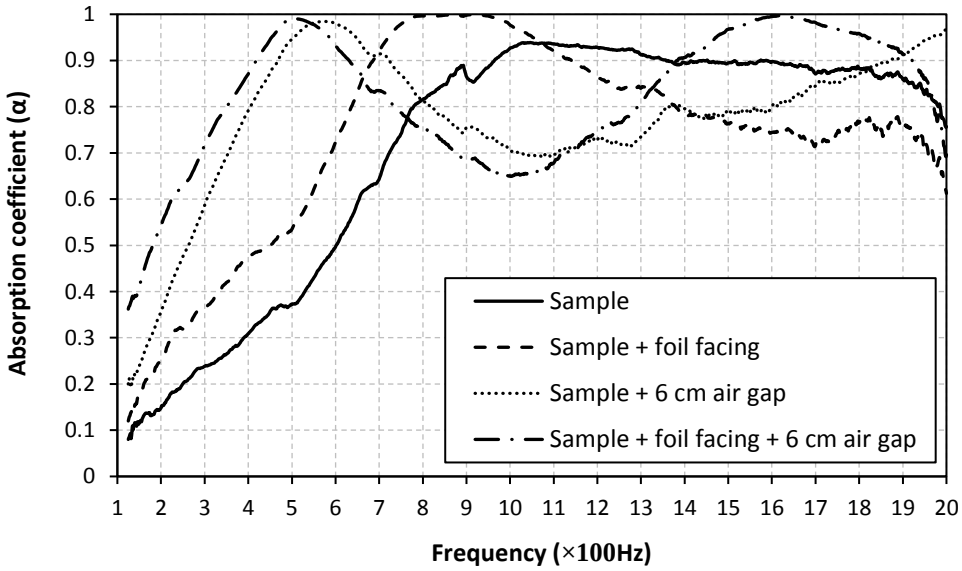

Figure 4-11: Effect of adding air gap and foil membrane on the acoustic performance of the foam sample designated as MS; sample thickness=5cm

4.4 Summary and Conclusion

In order to study the influence of cell size on sound absorption over the frequency range 100-2000Hz, the melt molding/particulate leaching method has been used to develop foam samples with different cell sizes. Three different salt sizes, i.e. 106-250, 250-500, and 500-850μm, were utilized to prepare the foam samples. The feasibility of using air gap and impervious membrane facing to improve sound absorption coefficient of the developed foam samples was examined as well.

Experimental results showed that open porosity were almost the same for all samples (around 88%). The cell size of the sample designated as SS was less than these of the other two samples, which had similar values. Also, the cell density of the sample designated as SS was one order of magnitude higher than these of the two samples, which had comparable values. The average throat size decreased as the salt size decreased.

The sound absorption curves of all of the foam samples were quite similar except for that of the sample designated as SS, which had higher absorption coefficient above 1000Hz. All samples were characterized by sound absorption coefficient less than 0.4 below 500Hz and sound absorption coefficient greater than 0.8 above 900Hz. The addition of foil membrane to the foam sample moderately improved absorption coefficient over the low frequency range, whereas adding air gap with 6cm thickness significantly increased sound absorption over the low frequency range.

Chapter 5 Development of Bimodal Thermoplastic Foams by Using Additives

5.1 Introduction

The proposed mechanism of developing double porosity foams by using additives is shown in Figure 5-1. The EVA grade with 18% VA content is characterized by inherent low melt strength. Upon foaming, cell coalescence occurs resulting in the formation of cells with sizes greater than 1mm. Sodium bicarbonate is an endothermic CBA characterized by a slow decomposition rate. Besides, it helps minimize the cell coalescence by increasing the melt strength of the polymer through absorbing heat during its decomposition. The characteristics of sodium bicarbonate support the formation of small cells. Similarly, wollastonite is an inorganic nucleating agent capable of reducing the cell size. Hence, the addition of these two additives would probably increase the population of small cells, which in conjunction with the existing large cells, will form foams with double porosity.

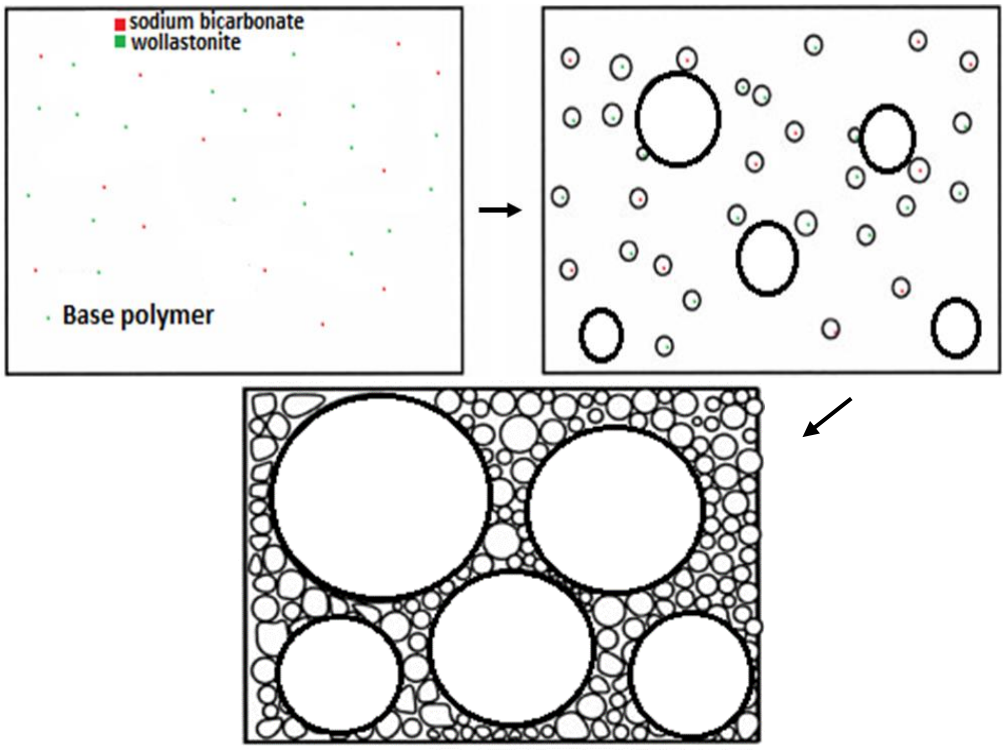

Figure 5-1: Mechanism of developing double porosity thermoplastic foams by using additives

5.2 Experimental Work

5.2.1 Materials

Sodium bicarbonate was purchased from Sigma Aldrich (Canada). It is anhydrous free-flowing white powder with purity of 99.7%. Wollastonite 520U was provided from FIBERTECH (Canada). The material is a naturally-occurring needle-like mineral with 55μm length, and 5μm diameter. All materials were used as provided.

5.2.2 Sample preparation

A two-stage foaming process 'compression molding-oven foaming' was utilized to produce chemically-blown foam samples. Celogen OT was employed at a concentration of 7.5% to achieve an expansion ratio of 8. The concentration of the additives was varied from 0 to 1%wt. The maximum concentration of these additives was fixed to 1% as extra amount did not introduce any significant change to the population of small cells. In the first stage of the experiment, 23g the polymer, which was coated with 0.5%wt. DOP, was dry mixed with 7.5% wt. Celogen OT and specified amounts of wollastonite and/or sodium bicarbonate according to the compositions given in Table 5-1. The mixture was then transferred into a mold consisting of a 3mm depth×101mm diameter circular die frame and two aluminum sheets with 3mm thickness. The sample was compression molded at 115^{o}C for 20 min. The mold was heated first without applying any pressure for 10 min to soften and sinter the polymer powder. After that, a pressure of 1000psi was applied for 10 min. The mold was finally removed and air cooled for 5 min. In the second stage, the molded sample was expanded in a heating oven. To this end, the sample was inserted in a larger mold with the same diameter, but with 24mm depth, and the mold was closed by using two 2″ C-clamps and placed in a forced convection heating oven working at 156^{o}C for 25 min. Finally, the mold was removed from the oven and cooled in a water bath maintained at 25^{o}C for 5 min before dismantling it. A homogeneous reference sample was prepared by foaming the EVA grade with 9% VA content using 7.5% Celogen OT in presence of 1% wollastonite. The same procedure was followed to prepare the reference foam sample. Three replicates were prepared from each samples.

Table 5-1: Compositions used to prepare the foam samples

Sample Code	EVA grade	Variable factors		Fixed factors	
		Amount of wollastonite (%wt.)	Amount of bicarbonate (%wt.)	Amount of Celogen OT (%wt.)	Amount of DOP (%wt.)
0W0B	Microthene MU76000	-	-	7.5	0.5
0W1B		-	1	7.5	0.5
1W0B		1	-	7.5	0.5
1W1B		1	1	7.5	0.5
HS	Microthene MU76300	1	-	7.5	0.5

5.3 Results and Discussion

5.3.1 Cellular structure characterization

Since the developed foam samples contained cells larger than 1mm, the analysis was conducted on a large volume of interest (i.e. a cylindrical region with 16mm diameter×8.4mm height) in order for the results to be statistically significant. The volume-weighted thickness distribution of the cell walls, extracted by the sphere-fitting algorithm, is shown in Figure 5-2. The average values of the cell wall thicknesses are listed in Table 5-2. It is apparent that all foam samples prepared from the low melt strength EVA grade (i.e. 0W0B, 0W1B, 1W0B, and 1W1B) were characterized by a large cell wall thickness (around 100μm). The cell wall thickness of the reference sample, designated as HS, was less than those of the other four samples by about 30μm. This difference can be attributed to the occurrence of cell coalescence in the samples prepared from the low melt strength polymer, resulting in fewer number of cells with larger cell walls.

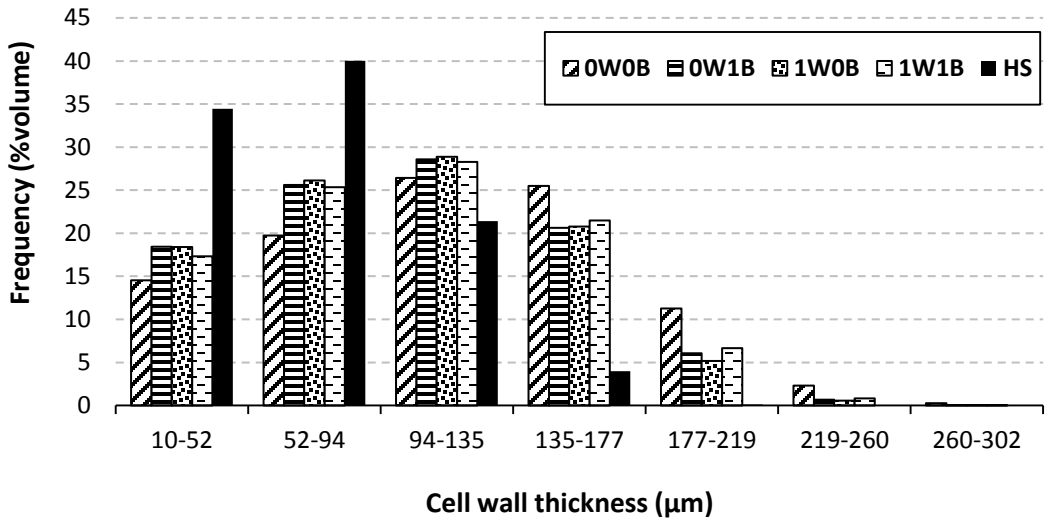

Figure 5-2: The volume-weighted thickness distribution of the cell walls

Table 5-2: The volume-weighted average thickness of the cell walls

Sample code	Average cell wall thickness (µm)
0W0B	117±12
0W1B	102±15
1W0B	102±15
1W1B	105±11
HS	71±13

The volume-weighted cell size distribution of homogeneous foam sample is shown in Figure 5-3, while the cell size distributions of foam the samples prepared from the low melt strength EVA are shown in Figure 5-4, Figure 5-5, Figure 5-6, and Figure 5-7. Table 5-3 lists the volume-weighted average cell size of the developed foam samples. It is clear that all of the foam samples prepared from the low melt strength polymer were characterized by a broad cell size distribution extending from 10µm up to 3000µm. The average cell sizes lied between 1214 and 1429µm compared to 656µm in the case of the reference sample. The broad cell size distribution of the samples prepared from the low melt strength polymers is due to the dominance of cell coalescence.

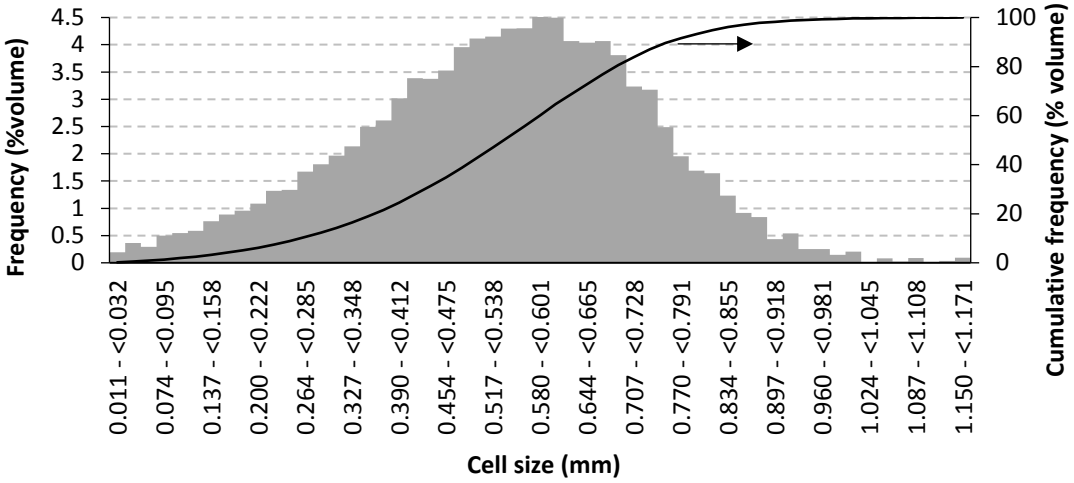

Figure 5-3: The volume-weighted cell size distribution of the homogeneous foam sample

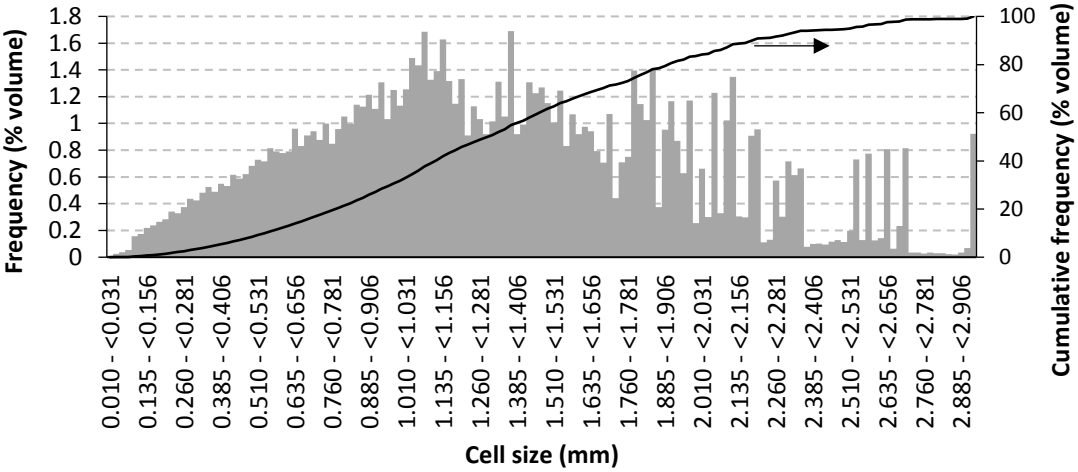

Figure 5-4: The volume-weighted cell size distribution of the foam sample prepared by 0% wollastonite and 0% sodium bicarbonate

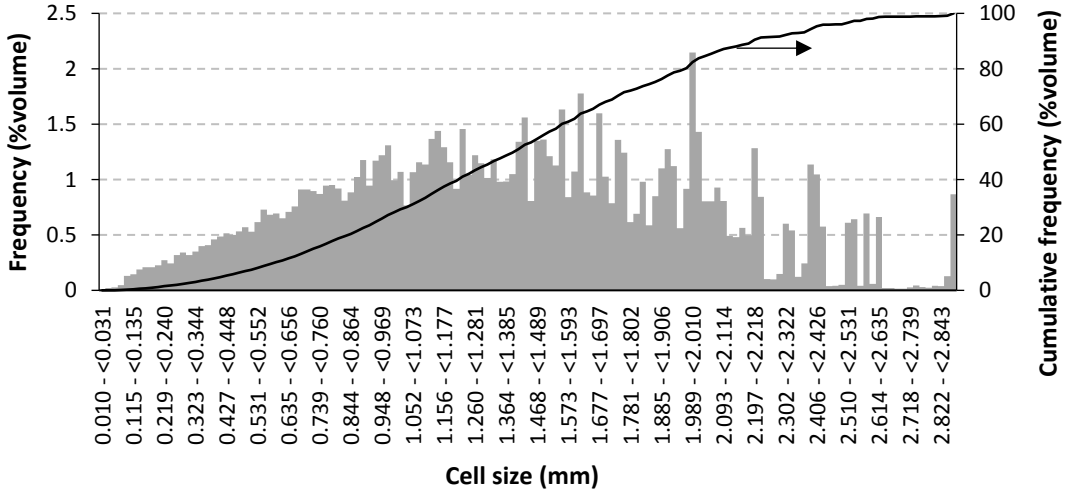

Figure 5-5: The volume-weighted cell size distribution of the foam sample prepared by 0% wollastonite and 1% sodium bicarbonate

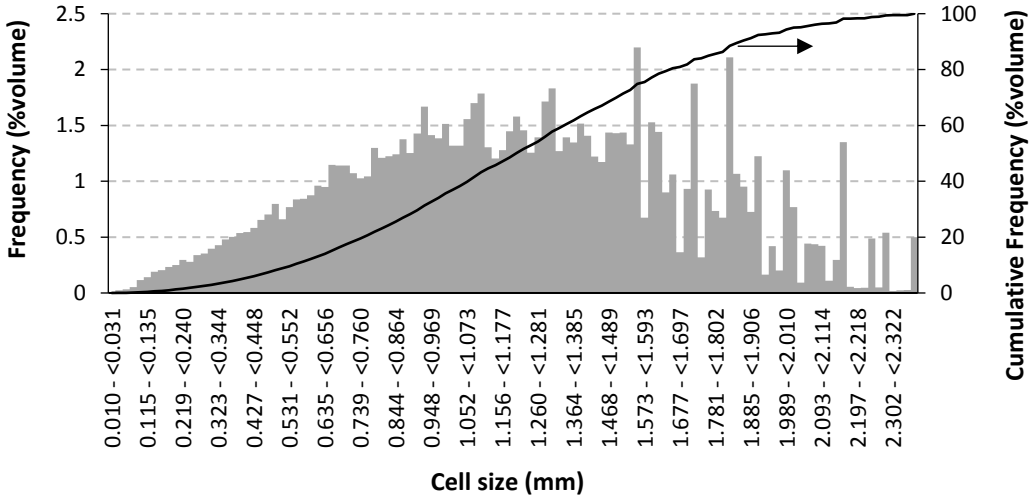

Figure 5-6: The volume-weighted cell size distribution of the foam sample prepared by 1% wollastonite and 0% sodium bicarbonate

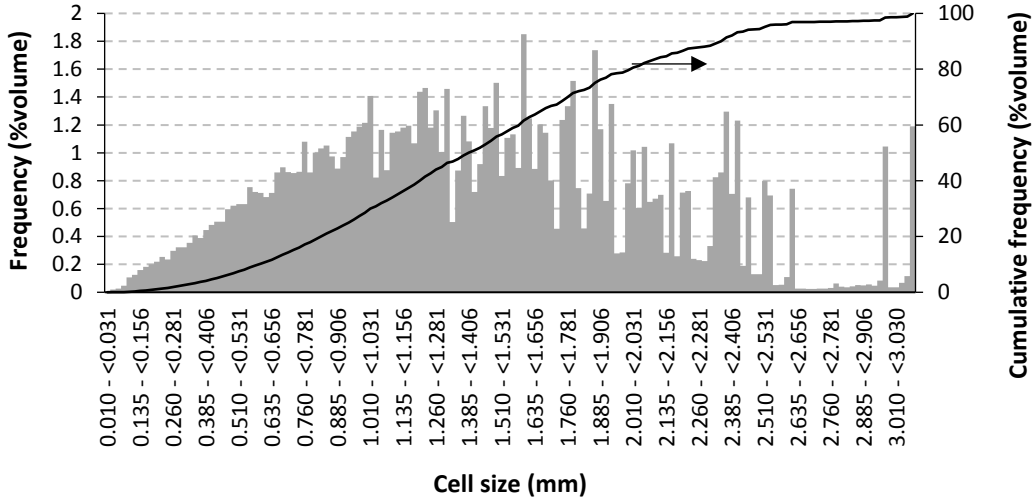

Figure 5-7: The volume-weighted cell size distribution of the foam sample prepared by 1% wollastonite and 1% sodium bicarbonate

Table 5-3: The volume-weighted average cell sizes of the developed foam samples

Sample code	Average cell size (µm)
0W0B	1355±50
0W1B	1429±45
1W0B	1214±66
1W1B	1387±56
HS	656±57

To compare between the cell size distributions of the developed foam samples, the cell size distribution was limited to three bins only: small size bin (<500µm), medium size bin (500-1000µm), and large size bin (>1000µm). This comparison is shown in Figure 5-8. It is clear that the cell size distributions of the samples prepared from the low melt strength polymer are very similar. The samples have a high percentage of the large size bin (62-72%vol.), a small percentage of the medium size bin (20-30%vol.) and a very low percentage of the small size bin (<10%vol.). The high percentage of the large size bin is the reason why the volume-weighted average cell size of these samples is larger than 1200µm. the reference sample, on the other hand, has a completely different cell size distribution, which is characterized by a high percentage of the medium size bin (70%vol.), along with a small percentage of the small size bin (25%vol.), and a very small percentage of the large size bin (5%vol.). Similarly, the high percentage of the medium size bin reduced the volume-weighted average cell size of the reference sample to 656µm.

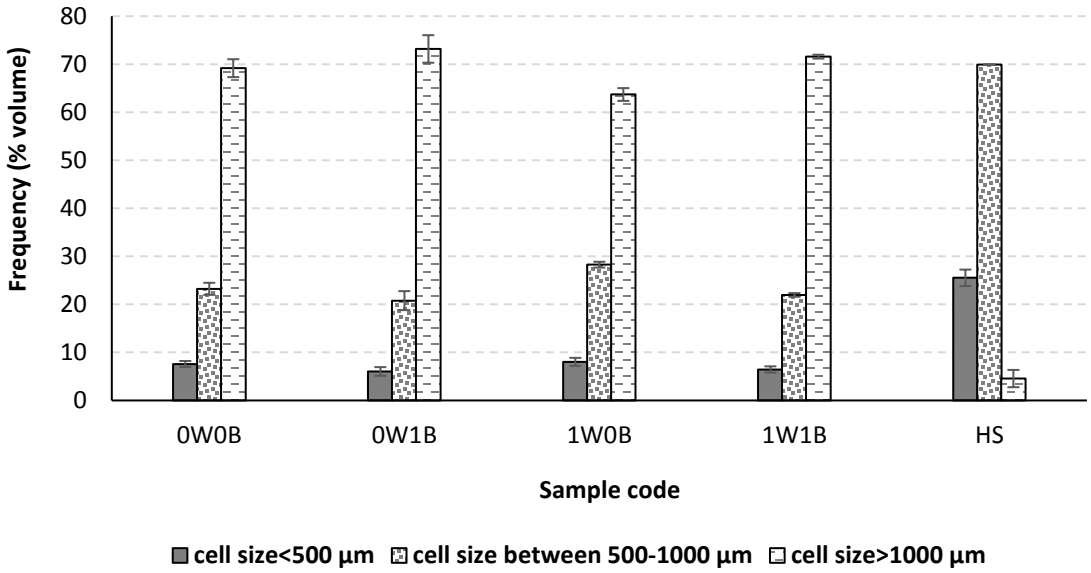

Figure 5-8: Comparison between the volume-weighted cell size distributions of the developed foam samples

Figure 5-9 shows the developed cellular structure of the sample designated as 0W0B in comparison to that of the reference sample, designated as HS. It is obvious that the reference sample is characterized by small cells separated by partially perforated walls, unlike the sample designated as 0W0B which is characterized by large cells and absence of such separating walls.

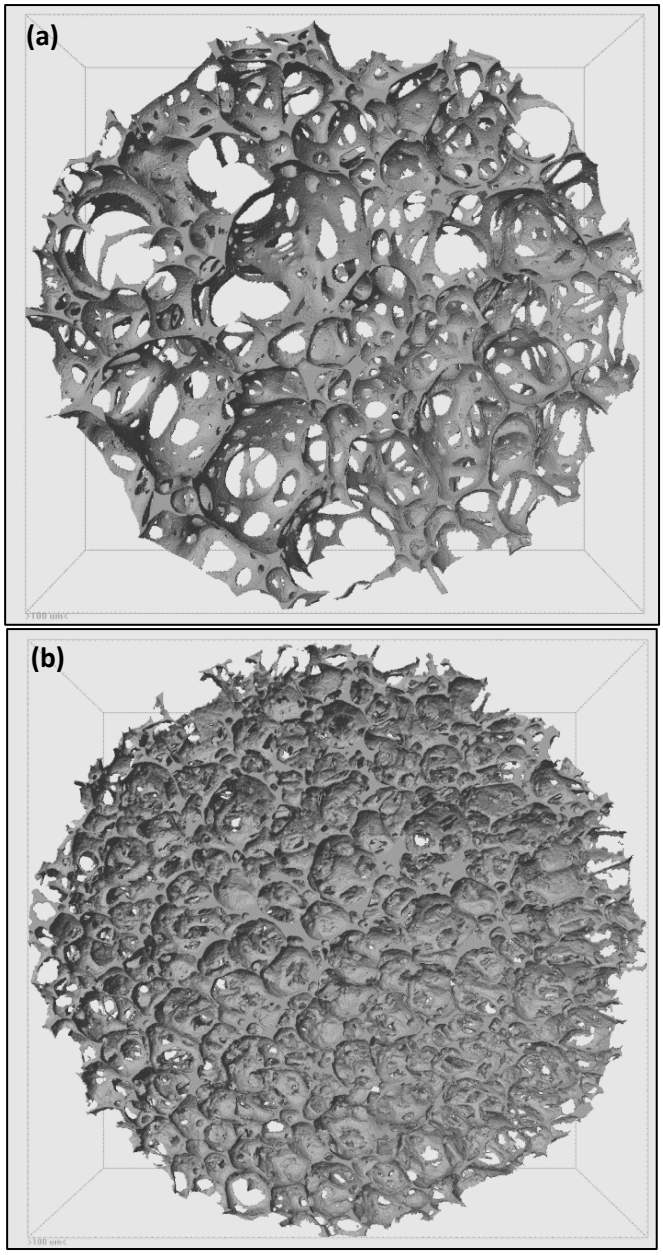

Figure 5-9: 3D models of foam samples designated as: (a) 0W0B, and (b) HS

The volume-weighted cell size distributions of the samples designated as 0W0B, 0W1B, 1W0B, and 1W1B were similar, and discrimintation between them was difficult especially for the small size bin. This is mainly because the fact that small cells do not add much to the volume. Better discrimination between samples cell size distributions can be realized if the cell size distribution is calucalted according to the number of the cells rather than their volume. The cell density of the foam samples can be calculated as well. To

calculate the number of cells and their sizes, the volume of the open cells needs to be separated into individualized cells. Imorph software was used to do this by running some built-in modules such as suface meshing (pores), granulometry (pores), and cell segmentation (watershed-pores) on the processed images that were exported from CTan software. .Two image showing the segmented cells of the samples designated as 0W0B and HS samples are displayed in Figure 5-10.

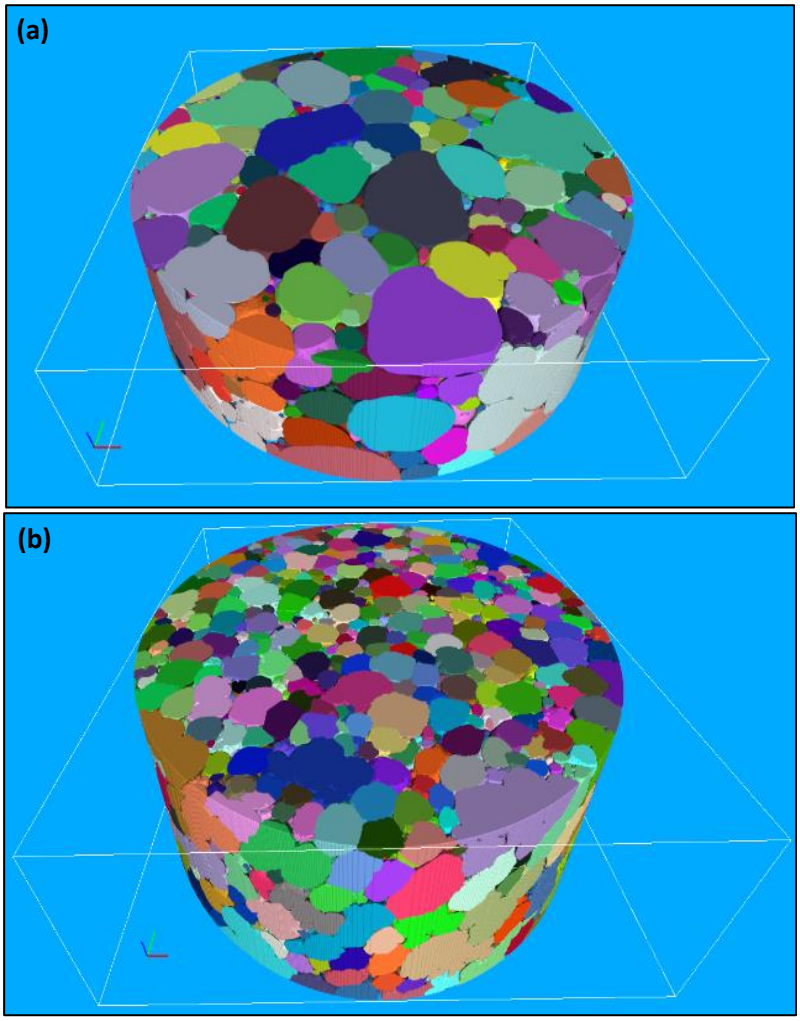

Figure 5-10: Segmented cells obtained by Imorph software for (a) 0W0B, and (b) HS foam samples

Two additional built-in modules including throats from cells segmentation (pores) and tortuosity (Graphs-pores) were also used to compute the size of the throats, and toruoisty of the developed foam samples. Figure 5-11 depicts the relative sizes and the spatial locations of the throats extracted for HS and 0W0B samples by Imorph software.

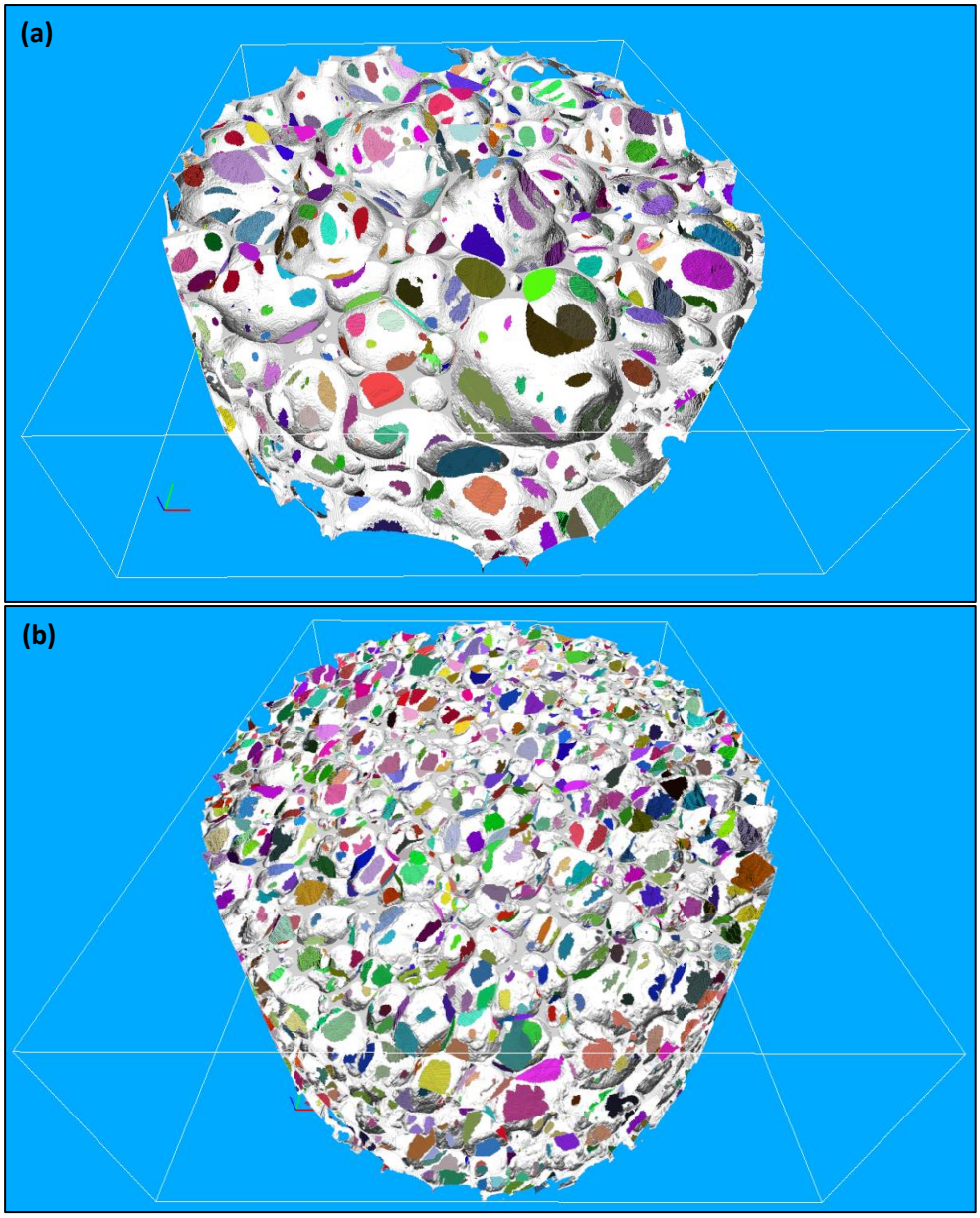

Figure 5-11: Relative sizes and spatial locations of throats extracted by Imorph software for: (a) 0W0B, and (b) HS

The number-weighted cell size distributions of the foam samples prepared from the low melt strength polymer are shown in Figure 5-12 compared to that of the reference sample. For all samples, the cell size distribution was calculated within the same volume of interest to enable comparing between them. It turns out from the figure that most of the cells of the reference sample lie within the 0.5-1mm bin.

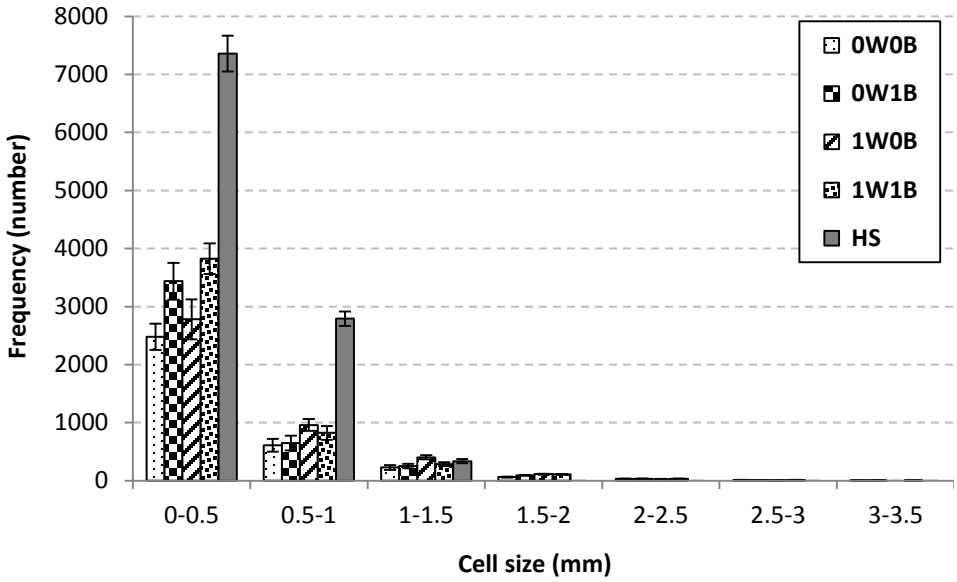

Figure 5-12: Comparison between the number-weighted cell size distributions of the developed foam samples

To investigate the influence of adding wollastonite and bicarbonate on each cell size range, plots showing the variation of the frequency with the amount of sodium bicarbonate added in presence/absence of wollastonite were generated for each bin. These plots are displayed collectively in Figure 5-13. To justify the linearity of the variations over the entire concentration range, two additional midpoints were created by preparing two more samples with compositions 0.5% sodium bicarbonate and 0% wollastonite, and 0.5% sodium bicarbonate and 1% wollastonite.

It can be concluded from these plots that adding sodium bicarbonate individually significantly increased the frequency of the small bin (0-0.5mm) as shown in Figure 5-13-a. Additionally, this reduced the frequency of the large bins (2.5-3 and 3-3.5mm) shown in Figure 5-13-f and Figure 5-13-g at the expense of increasing the frequency of smaller ones (0-0.5 and 1.5-2mm) shown in Figure 5-13-a and Figure 5-13-d. In presence of wollastonite, the addition of bicarbonate increased the frequency of the large bins (2.5-3 and 3-3.5mm) shown in Figure 5-13-f and Figure 5-13-g at the cost of decreasing the frequency of the mid-size bins (0.5-1 and 1-1.5mm) shown in Figure 5-13-b and Figure 5-13-c. Meanwhile, it increased the frequency of the small bin (0-0.5mm) as shown in Figure 5-13-a.

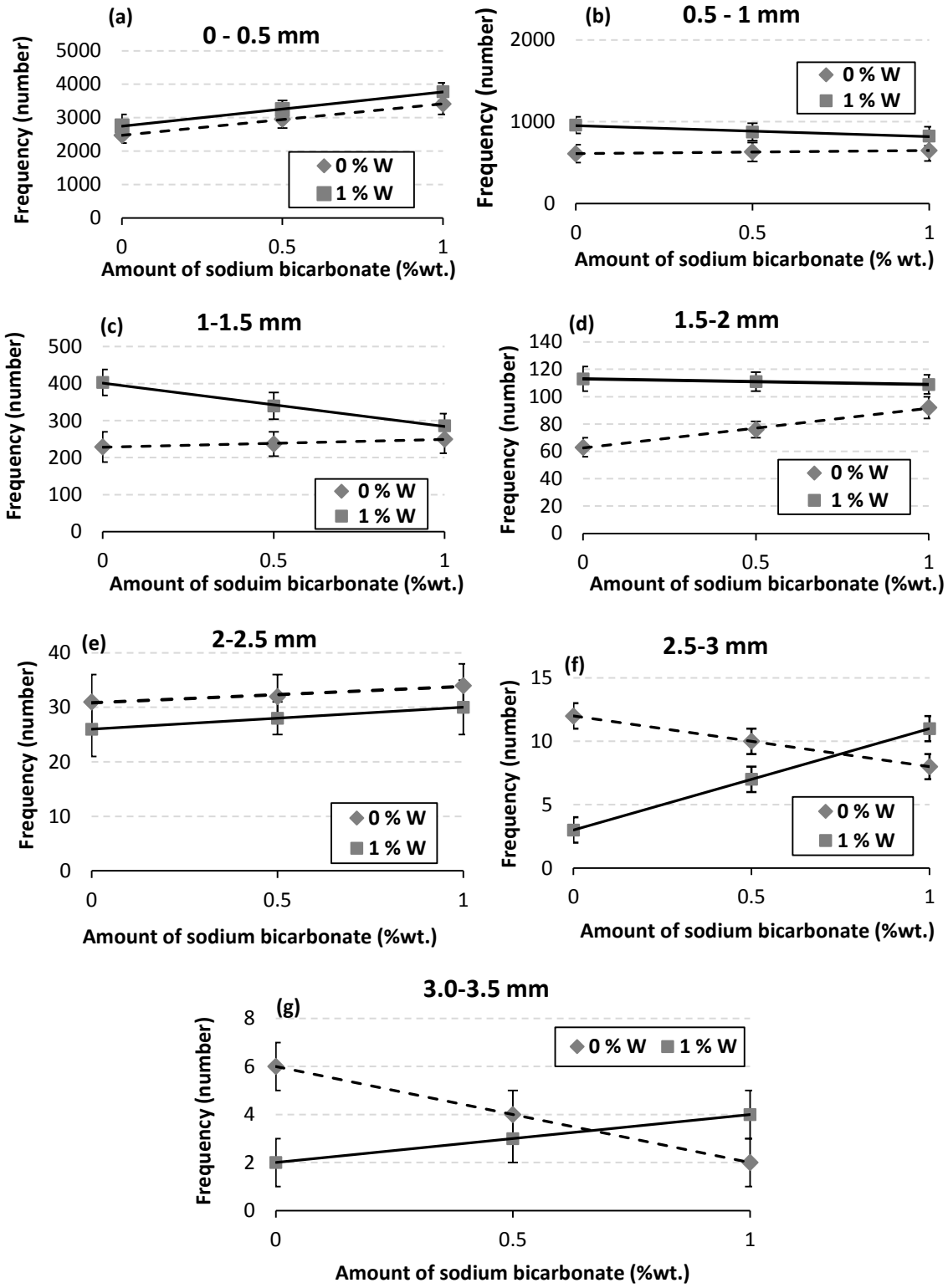

Figure 5-13: Effect of adding wollastonite and sodium bicarbonate on the frequency of each cell size range

Table 5-4 lists the characteristics of the cellular structure of the developed foam samples. Open porosity was greater than or equal to 90% for all foam samples, and it did not change significantly between them, i.e. only 3% difference between the lowest and the highest value. It is clear that the number-based average cell sizes of the samples were smaller than volume-based ones. The reason behind this is that the number-based average cell size is mainly ruled by the number of the cells which is large and influential in the case of small cells. The volume-based average cell size, on the other hand, is mainly governed by the volume of the cells which is large and influential in the case of large cells even if their number is small.

The results also indicate that the addition of wollastonite and sodium bicarbonate either individually or collectively had nearly negligible effect on both tortuosity and average throat size, as the differences were within the experimental error range. The addition of sodium bicarbonate in absence of wollastonite reduced the average cell size by 50μm, whereas it reduced its value by 42μm in presence of 1%wt. wollastonite. Moreover, the addition of sodium bicarbonate, in absence of wollastonite, increased the cell density by 1030cell/cm^3, while its addition in presence of 1% wollastonite increased the cell density by 800cell/cm^3. These results manifested the influence of the simultaneous addition of sodium bicarbonate and wollastonite on increasing the population of both small and large cells in the developed foam samples.

Table 5-4: The celllular structure characteristics of the developed foam samples

Property	**Sample code**				
	0W0B	**0W1B**	**1W0B**	**1W1B**	**HS**
Open porosity (%)	91.78±0.26	93.27±0.25	91.78±0.30	93.26±0.99	90.58±1.18
Cell density (cell/cm^3)	3.40×10^3 (±250)	4.43×10^3 (±299)	3.54×10^3 (±289)	4.20×10^3 (±250)	1.50×10^4 (±266)
Average cell size (μm)	433±30	383±25	479±27	391±27	293±33
Average throat size (μm)	94.79±10	96.28±12	104.35±9	105.90±13	65.56±15
Tortuosity (-)	1.31±0.02	1.29±0.03	1.34±0.01	1.29±0.03	1.65±0.05

5.3.2 Acoustic measurements

The results of the acoustic measurements for the developed foam samples are shown in Figure 5-14. Each curve represents the average of five different measurements with a standard deviation of ±0.05. It is clear that the absorption curve of the reference sample was less than 0.3 for frequencies up to 1450Hz, and the curve was characterized by an absorption peak with a value of 1 occurring at 1534Hz. The absorption coefficients of the samples designated as 0W0B, 0W1B, 1W0B, and 1W1B were greater than these of the reference sample over the entire measurement range except for the 1550Hz frequency where all the peaks coincide. The absorption curves of these samples were characterized by two absorption peaks with a plateau region in-between. The values and the positions of these absorption peaks are listed in Table 5-5. The value of the first peak was between 0.59 (for 1W0B sample) and 0.86 (for 1W1B sample). The second peak occurred at higher frequency (i.e. around 1535Hz), and its values were for all samples. The absorption curve of the sample designated as 1W1B was characterized by a steep rise over the frequency region 100-300Hz. Above 1700Hz, the absorption curves of all foam samples were comparable Over the frequency region 200-1450Hz, the absorption coefficient increased among the developed foam samples in such a way that HS<1W0B<0W1B<0W0B<1W1B.

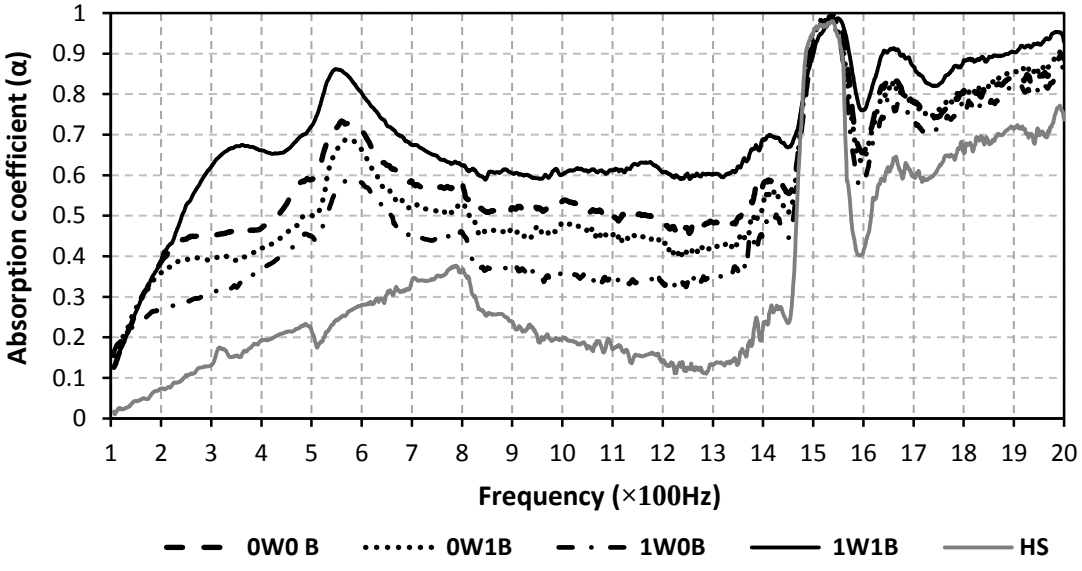

Figure 5-14: The absorption curves of the developed foam samples; sample thickness=5cm

Table 5-5: Values and positions of absorption peaks

Sample code	First absorption peak		Second absorption peak	
	f (Hz)	**α (-)**	**f (Hz)**	**α (-)**
0W0B	560	0.74	1536	1
0W1B	570	0.69	1535	1
1W0B	580	0.59	1534	1
1W1B	550	0.86	1545	1

The poor acoustic performance of the reference homogeneous sample is related to the characteristics of its cellular structure. The sample was characterized by small cells (293±266μm) separated by polymer walls that were partially perforated by small size throats (65.56±36μm). These features increased the complexity of the cellular structure leading to increasing of both tortuosity, which was 1.65 and air flow resistivity, which had the value of 750,547 rayl/m. As a consequence, sound waves were unable to access the foam samples, and experienced severe reflection at the material surface.

To study the effect of adding bicarbonate and wollastonite on the acoustic performance of the developed foam samples over the octave bands 177-355, 355-710, and 710-1420Hz, sound absorption coefficients at the central frequencies 250, 500, and 1000Hz were extracted from Figure 5-14 and plotted versus the amount of sodium bicarbonate added in presence/absence of wollastonite in Figure 5-15, Figure 5-16, and Figure 5-17, respectively. It is apparent that the addition of sodium bicarbonate in presence/absence of wollastonite had a similar effect on sound absorption coefficient over the frequency range extending from 177 to 1420Hz. the addition of wollastonite individually resulted in an adverse effect on sound absorption coefficient. Similarly, the addition of sodium bicarbonate individually had either adverse or insignificant effect on sound absorption coefficient depending on the frequency. In a different way, the simultaneous addition of sodium bicarbonate and wollastonite showed a synergistic effect on improving sound absorption coefficient.

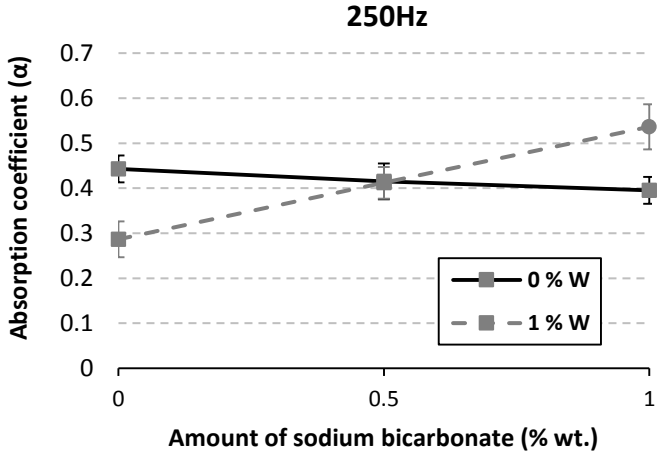

Figure 5-15: The effect of adding wollastonite and sodium bicarbonate on sound absorption coefficient at 250Hz

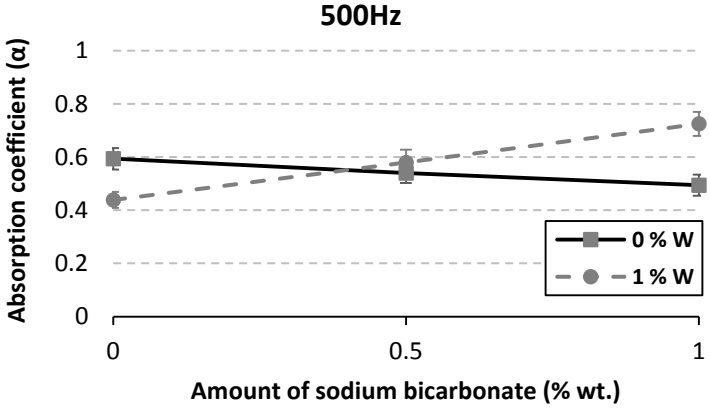

Figure 5-16: The effect of adding wollastonite and sodium bicarbonate on sound absorption coefficient at 500Hz

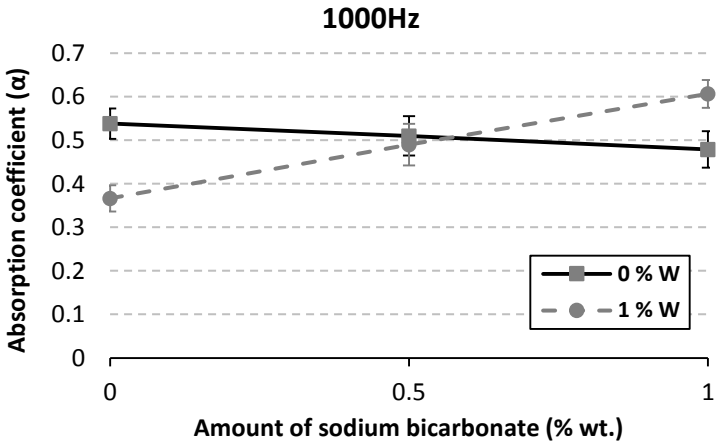

Figure 5-17: The effect of adding wollastonite and sodium bicarbonate on sound absorption coefficient at 1000Hz

Such behavior can be interpreted in terms of the developed cellular structure along with the air flow resistivity measurements which are plotted as a function of the concentrations of sodium bicarbonate and wollastonite in Figure 5-18. The addition of sodium bicarbonate significantly increased the number of small cells (0-0.5mm) at the expense of reducing the number of larger cells (2.5-3 and 3-3.5mm). This led to a slight increase in air flow resistivity. Ultimately these variations resulted in a slight negative or insignificant influence on sound absorption coefficient, depending on the frequency.

Adding wollastonite decreased the number of large cells (2-2.5, 2.5-3, and 3-3.5mm) at the cost of increasing the number small ones (0.5-1, 1-1.5, and 1.5-2mm). These changes caused a significant increase in air flow resistivity, which in turn increased sound reflection at the material surface. The simultaneous addition of these two additives increased the number of the large cells (2.5-3 and 3-3.5mm) at the expense of decreasing the number of the medium size cells (0.5-1 and 1-1.5mm). Meanwhile, it increased the frequency of the small cells (0-0.5mm). The introduction of large cells significantly reduced the air flow resistivity as shown in Figure 5-18. This reduction in flow resistivity minimized sound reflection at the surface of the material, which in turn increased the interaction of sound waves with the material cellular structure. Meanwhile, the presence of small cells enhanced sound dissipation by viscous losses.

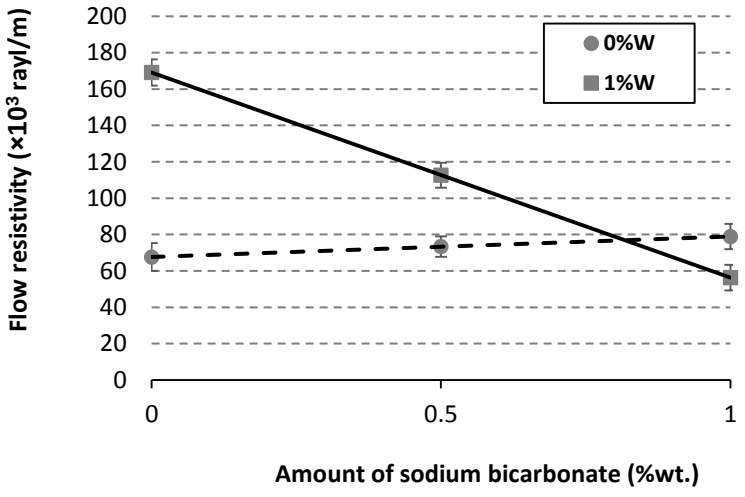

Figure 5-18: The effect of adding wollastonite and sodium bicarbonate on the air flow resistivity of the developed samples

5.4 Summary and Conclusion

In this chapter, development of heterogeneous thermoplastic foams that are characterized by a combination of small cells and large cells was conducted successfully. In the experiments, a low melt strength EVA grade (18% VA) was foamed by Celogen OT at a concentration of 7.5%wt. in the two-stage process 'compression molding-oven foaming' to produce foams with large cells, i.e. larger than 1mm. The addition of the endothermic CBA 'sodium bicarbonate' and the inorganic nucleating agent 'wollastonite' modified the cellular structure by increasing the number of small cells. For comparison, a homogeneous foam sample was prepared by expanding of a foamable EVA grade (9% VA) using 7.5%wt. Celogen OT in presence of 1%wt. wollastonite.

Generally, all foam samples prepared from the low melt strength polymer were characterized by larger cells and broader size distribution compared to the homogeneous foam sample. The addition of sodium bicarbonate individually reduced the frequency of the large bins (2.5-3 and 3.0-3.5mm) at the expense of that of the smaller cells (0-0.5 and 1.5-2mm). The addition of sodium bicarbonate in presence of wollastonite increased not only the frequency of the large size bins (2.5-3 and 3-3.5mm) but also the frequency of the small size bin (0-0.5mm). Regarding the effect of the additives on the characteristics of the developed cellular structure, it was found that adding wollastonite and sodium bicarbonate either individually or collectively had negligible effect on porosity, tortuosity and average throat size. The simultaneous addition of the additives reduced the number-weighted average cell size by 42μm, and increased the cell density by 1031cell/cm^3.

The results of the acoustic measurements indicated that the homogeneous sample had poor absorption performance for frequencies up to 1450 Hz due to the presence of small cells enclosed by partially perforated walls. The heterogeneous foam samples prepared from the low melt strength polymer were characterized by improved sound absorption coefficient over the entire measurement range, and the increase in the absorption performance followed the order: HS<1W0B<0W1B<0W0B<1W1B. For these samples, it was found that the addition of wollastonite resulted in a negative effect on sound absorption

coefficient, whereas the addition of sodium bicarbonate had either a negative or an insignificant effect on sound absorption coefficient. The simultaneous addition of sodium bicarbonate and wollastonite resulted in synergistic effect on improving sound absorption coefficient. The introduction of sodium bicarbonate significantly increased the number of the small cells at the expense of reducing the number of larger cells leading to a slight increase in air flow resistivity and a slight negative or insignificant impact on sound absorption coefficient, depending on the frequency The simultaneous addition of wollastonite and sodium bicarbonate increased the populations of both large and small cells. Such bimodal cellular structure showed a synergistic effect on sound absorption coefficient over the frequency range extending from 177 up to 1420Hz.

Chapter 6 Development of Bimodal Thermoplastic Foams by Blending a Foamable Polymer with a Low Melt Strength Polymer

6.1 Introduction

The proposed mechanism of developing double porosity foams by adding low melt strength polymers is shown in Figure 6-1. It is known from the previous chapter that foaming of the EVA grade, which has 9%VA, using 7.5%wt. Celogen OT produced homogeneous foam samples with small cells (293±33μm). Blending the polymer with another low melt strength polymer would probably introduce some large cells at the sites where the low melt strength polymer is distributed as a result of its cell coalescence. To study the effectiveness of this mechanism in developing double porosity foams, two different low melt strength polymers, EVA grade with 18% VA and PEO, were used in the experiments, and the concentration was varied from 0, 5, 10, to 15% by weight. The maximum concentration of the added polymer was fixed to 15% as extra amounts resulted in the deterioration of the developed cellular structure. Seven different foamable compositions were prepared in accordance with Table 6-1. For each composition, three replicates were prepared giving rise to 21 samples in total.

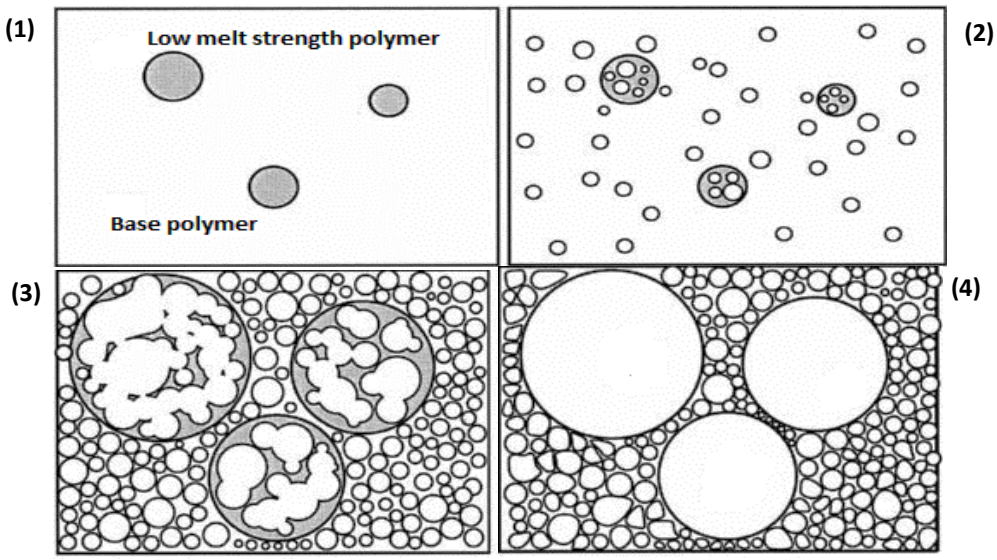

Figure 6-1: Mechanism of developing double porosity foams through blending with a low melt strength polymer

Table 6-1: Variable and fixed factors used in the experiments

Sample Code	Variable factors		Fixed factors			No. of samples
	Polymer type	Polymer concentration (%wt.)	Celogen OT concentration (% wt.)	DOP concentration (% wt.)	Wollastonite concentration (%wt.)	
Neat sample	-	-	7.5	0.5	1.0	3
5E	MU 76000	5	7.5	0.5	1.0	3
10E		10	7.5	0.5	1.0	3
15E		15	7.5	0.5	1.0	3
5P	PEO	5	7.5	0.5	1.0	3
10P		10	7.5	0.5	1.0	3
15P		15	7.5	0.5	1.0	3
Total number of samples						21

6.2 Experimental Work

Chemically-blown foam samples were prepared by a two-stage foaming process 'compression molding-oven foaming' according to the compositions given in Table 6-2. In the first step, a homogeneous mixture was prepared from the powder ingredients by dry-mixing them for 5 min in a high shear mixer. The prepared mixture was then transferred into a mold consisting of a 3mm depth × 101mm diameter circular die frame and two aluminum sheets with 3mm thickness, and it was compression molded at 120^{o}C for 20 min. The mold was heated first without applying any pressure for 10 min to soften the polymer powder. After that, a pressure of 1000psi was applied and released instantaneously for ten times to remove any entrapped air bubbles. After completing this step, the mold was kept closed under a pressure of 1000psi for additional 10 min. The mold was finally removed from the press, and cooled in air for 5 min. In the second stage of the foaming experiment, the molded sample was placed in a larger mold having the same diameter but with a 26mm depth. The mold was closed by using two 2″ C-clamps, and placed in a forced convection heating oven working at 156^{o}C for 26 min to expand the samples in ambient atmosphere. Last, the mold was removed from the oven and cooled in a water bath maintained at 25^{o}C for 7 min before dismantling it and removing the sample.

Table 6-2: Compositions used to develop the double porosity foam samples

Sample Code	Amount of base polymer (g)	Added polymer		Amount of Celogen OT (g)	Amount of DOP (g)	Amount of wollastonite (g)
		Type	Amount (g)			
Neat sample	23.00	Microthene MU76000	0	1.725	0.115	0.23
5E	21.85		1.15	1.725	0.115	0.23
10E	20.70		2.30	1.725	0.115	0.23
15E	19.55		3.45	1.725	0.115	0.23
5P	21.85	PEO	1.15	1.725	0.115	0.23
10P	20.70		2.30	1.725	0.115	0.23
15P	19.55		3.45	1.725	0.115	0.23

6.3 Results and Discussion

6.3.1 Cellular structure characterization

Since the developed foam samples contained cells larger than 1mm in conjunction with other small cells, the cellular structure analysis was performed on a large volume of interest (i.e. a cylindrical region with 16mm diameter×8.4mm height) in order for the results to be statistically significant. The volume-weighted average thickness of the cell walls are listed in Table 6-3, whereas Figure 6-2 shows the variation of the average wall thickness with the concentration of the blended polymer. The experimental results showed that the average thickness of the cell walls experienced a slight linear increase as the amount of blended polymer increased for both polymers. Moreover, the increase was higher in the case of adding PEO. For microthene MU76000, the average thickness of the cell walls increased from 67 to 89μm after adding 15%wt, whereas adding 15%wt. PEO increased the average cell wall thickness from 67 to 109μm.

Table 6-3: The volume–weighted average cell wall thickness of the developed foam samples

Sample code	Cell wall thickness (µm)	Sample code	Cell wall thickness (µm)
Neat sample	67±3	**Neat sample**	67±3
5E	75±3	**5P**	88±5
10E	87±4	**10P**	93±3
15E	89±4	**15P**	109±3

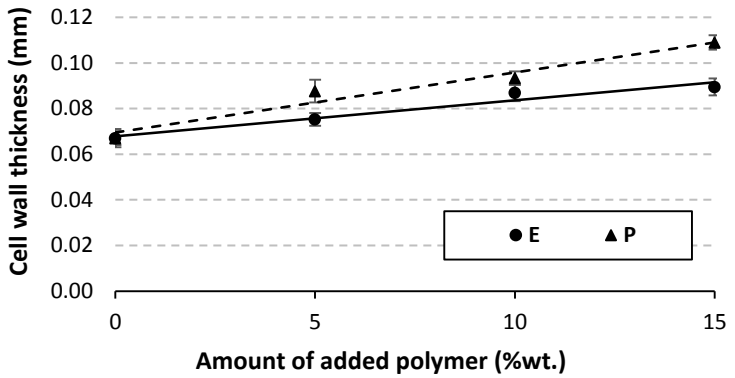

Figure 6-2: The effect of the concentration of the added polymer on the average thickness of the cell walls

The volume-weighted cell size distributions of the developed foam samples are shown in Figure 6-3. To study the effect of the concentration of the added polymer on the cell size distribution, the frequency of each bin was extracted from Figure 6-3 and plotted as a function of the concentration of the added polymer for each polymer type. The results are displayed in Figure 6-4.

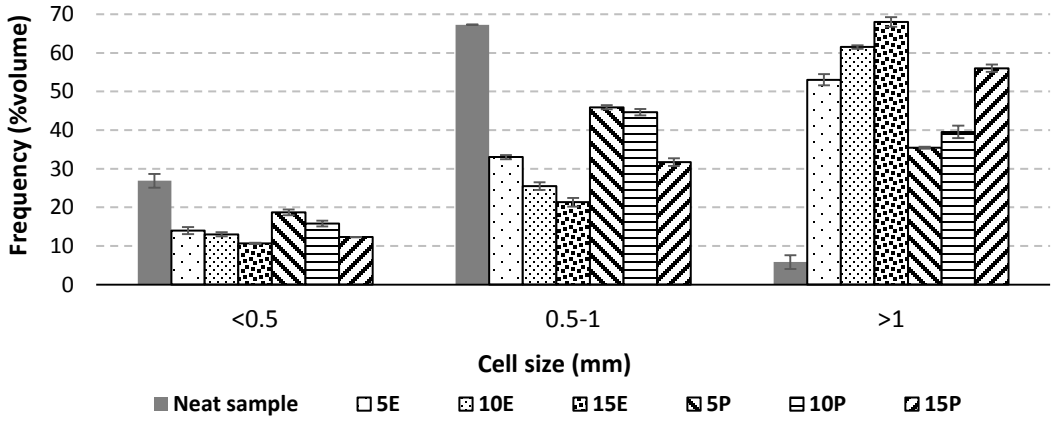

Figure 6-3: The volume-weighted cell size distributions of the developed foam samples

In general, it can be concluded that increasing the concentration of the added polymer increases the population of the large cells at the expense of reducing these of small and mid-size cells. Also, the influence of adding the low melt strength EVA grade is more significant than that of PEO over the entire concentration range. The addition of 5%wt. of any of the two polymers reduced the frequencies of the small (<0.5mm) and medium (0.5-1mm) bins significantly. This reduction shifted the frequency of the large bin (>1mm) to a higher value. These changes were slight when increasing the concentration of the blended polymer from 5% to 10%, as indicated by a slight slope or almost plateau region in the curve segment connecting between these two concentrations.

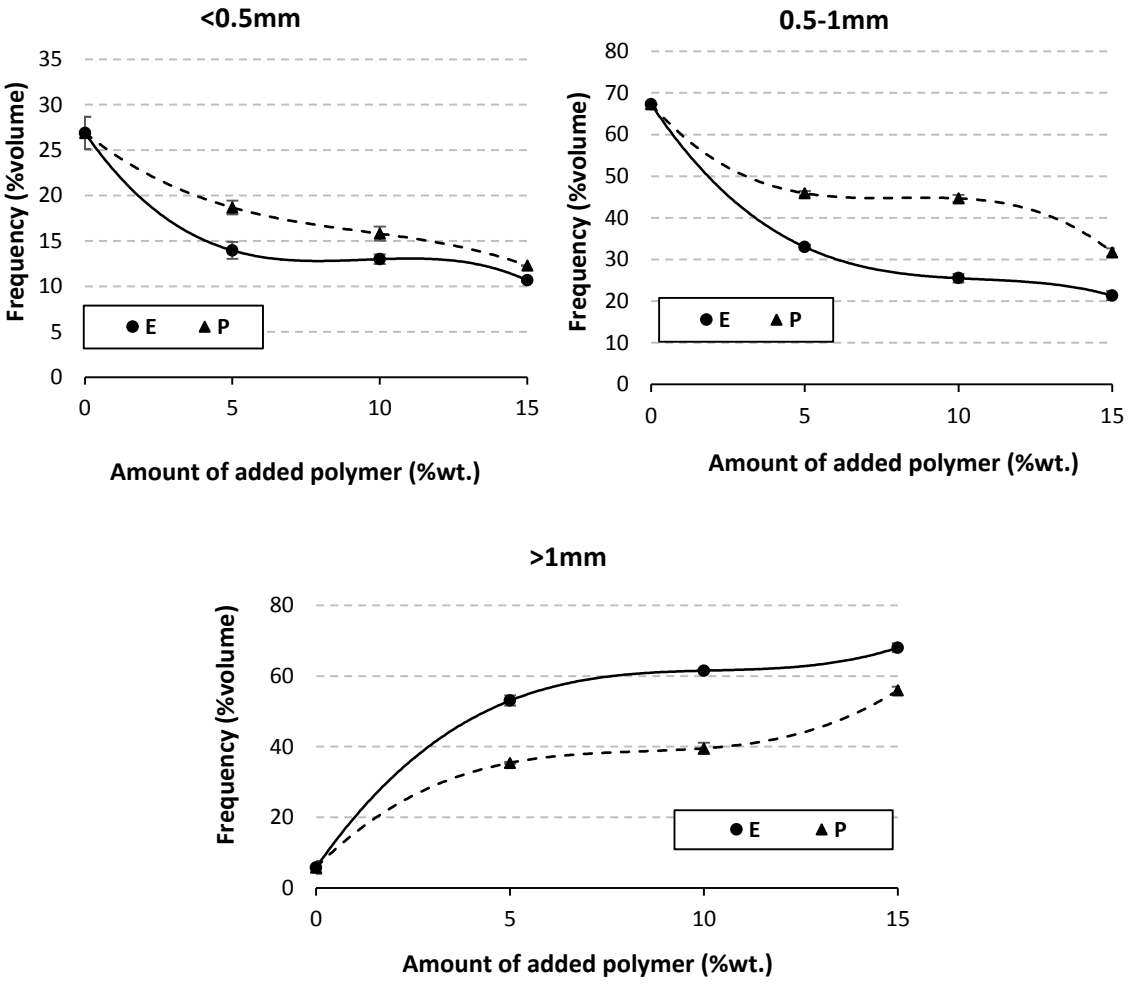

Figure 6-4: The effect of the concentration of the added polymer on the volume-weighted frequency of each size range

The volume-weighted average cell sizes of the developed foam samples are listed in Table 6-4. A plot of the variation of the average cell size with the concentration of the added polymer was generated from the tabulated data, and it is presented in Figure 6-5. The average cell size increased when increasing the concentration of the added polymer, and the effect of the low melt strength EVA grade was higher than that PEO. The average cell size increased from 656µm to 1410µm when 15%wt. of the low melt strength EVA grade was added, whereas adding 15%wt. of PEO increased the average cell size from 656µm to 1129µm. The increase in the average cell size is attributed to the effect of adding the low melt strength polymers on increasing the population of the large cells, which in turn shifted the average cell size to higher values.

Table 6-4: The volume-weighted average cell size of the developed foam samples

Sample code	Cell size (µm)	Sample code	Cell size (µm)
Neat sample	656±51	Neat sample	656±51
5E	1114±18	5P	865±42
10E	1260±13	10P	915±52
15E	1410±19	15P	1129±36

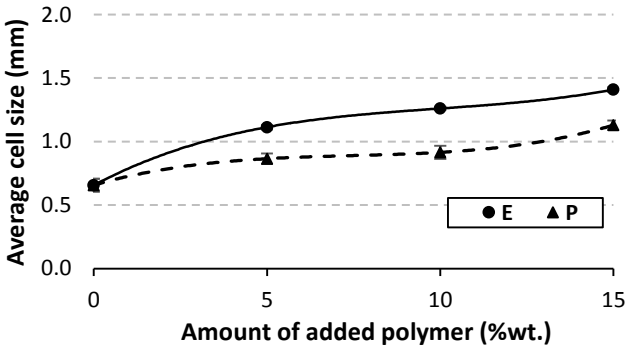

Figure 6-5: The effect of the concentration of the added polymer on the volume-weighted average cell size

To obtain the cell density, the number-weighted cell size distribution, the number-weighted average cell size, the tortuosity, and the average throat size, the volume of the open cells was segmented using Imorph software as shown in Figure 6-6, and a number of built-in modules including surface meshing (pores), granulometry (pores), cell segmentation (watershed-pores), throats from cell segmentation (pores), and tortuosity (graph-pores) were applied to compute these properties.

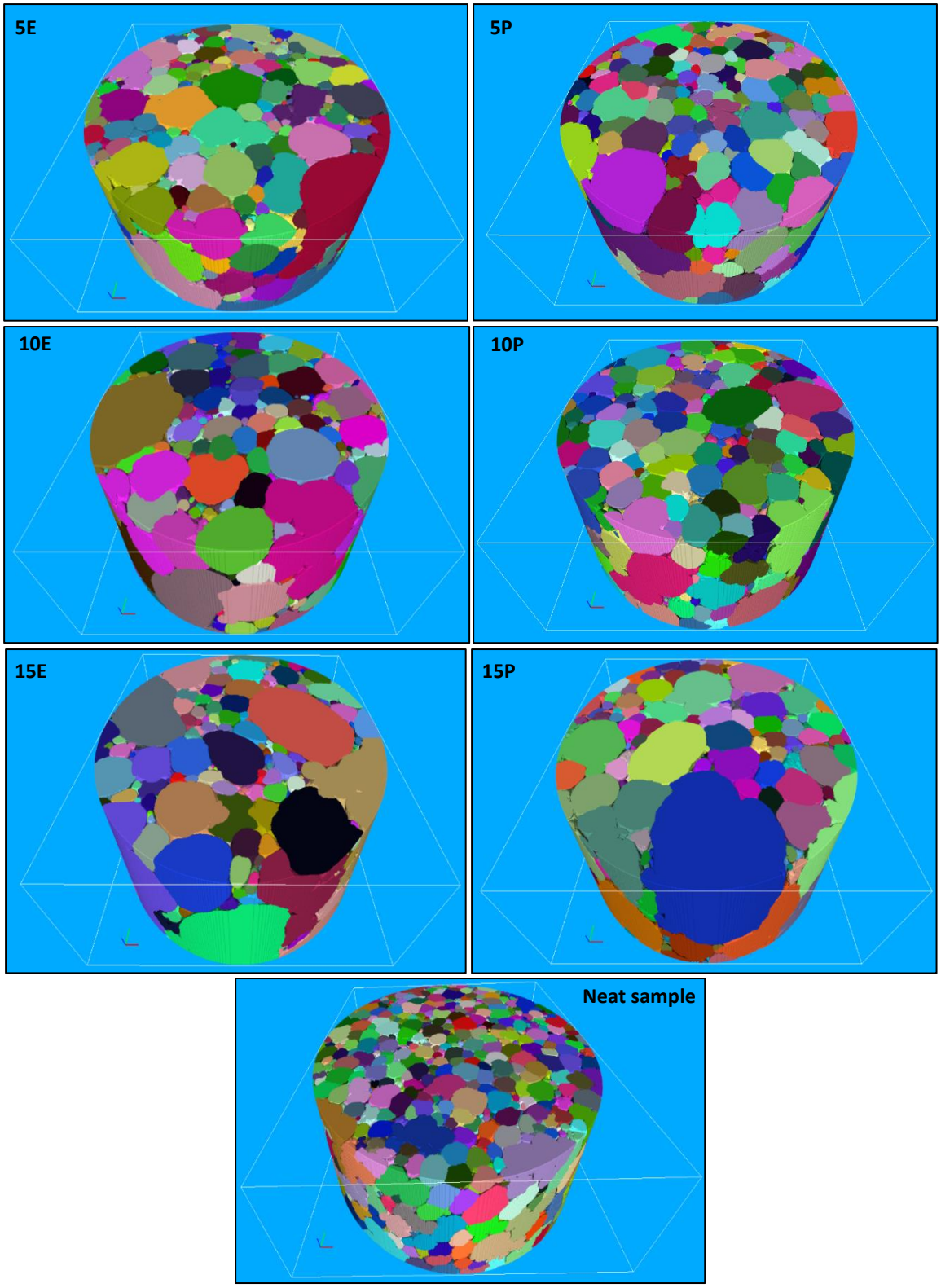

Figure 6-6: Images visualizing the effect of adding the low melt strength polymers on the cell size and the cell density of the developed foams

The number-weighted cell size distributions of the developed foam samples is displayed in Figure 6-7. The analysis was done on the same volume of the foam samples (1672.97mm^3) in order for the results to be valid for comparison. To investigate the effect of the concentration of the added polymer on the cell size distribution, the frequency of each bin was extracted from the graph and plotted as a function of the added polymer concentration. These plots are shown in Figure 6-8.

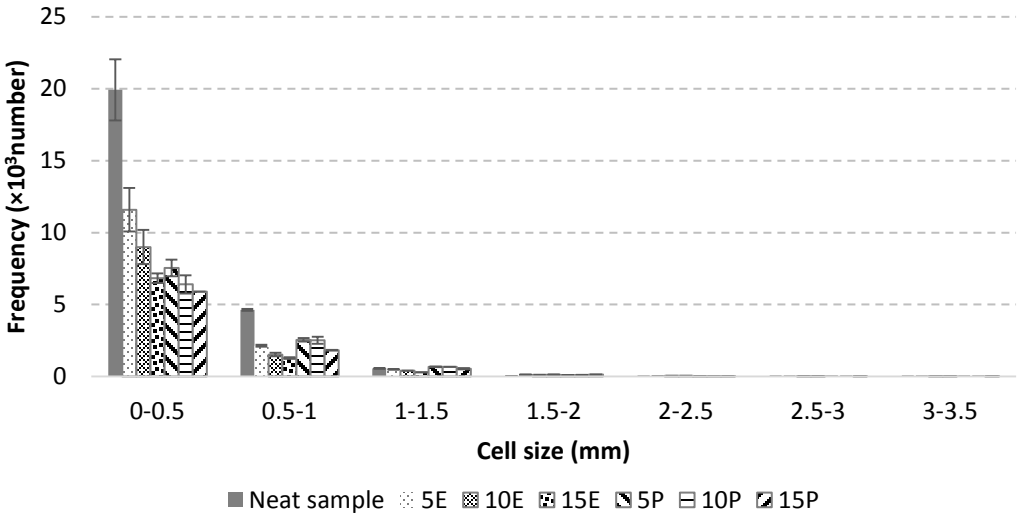

Figure 6-7: The number–weighted cell size distributions of the developed foam samples

It turns out from these plots that the frequency of the 0-0.5mm bin decreased as the concentration of the added polymer increased over the entire concentration range. The influence of adding PEO on reducing the frequency of this bin was more remarkable than that of EVA especially at the concentrations of 5%wt. and 10%wt. The frequency of the 0.5-1mm bin decreased significantly when adding 5% of the polymer, then it experienced a slight reduction at higher concentrations. Additionally, the low melt strength EVA was more effective in reducing the frequency of this bin. Unlike PEO, which slightly increased the frequency of the 1-1.5mm bin especially at the concentrations of 5 and 10%wt., the low melt strength EVA grade reduced the frequency of the bin linearly over the entire concentration range. For the 1.5-2mm bin, PEO increased its frequency over the entire concentration range, while the low melt strength EVA increased the frequency only at the concentration of 5%wt after which a reduction in the frequency occurred.

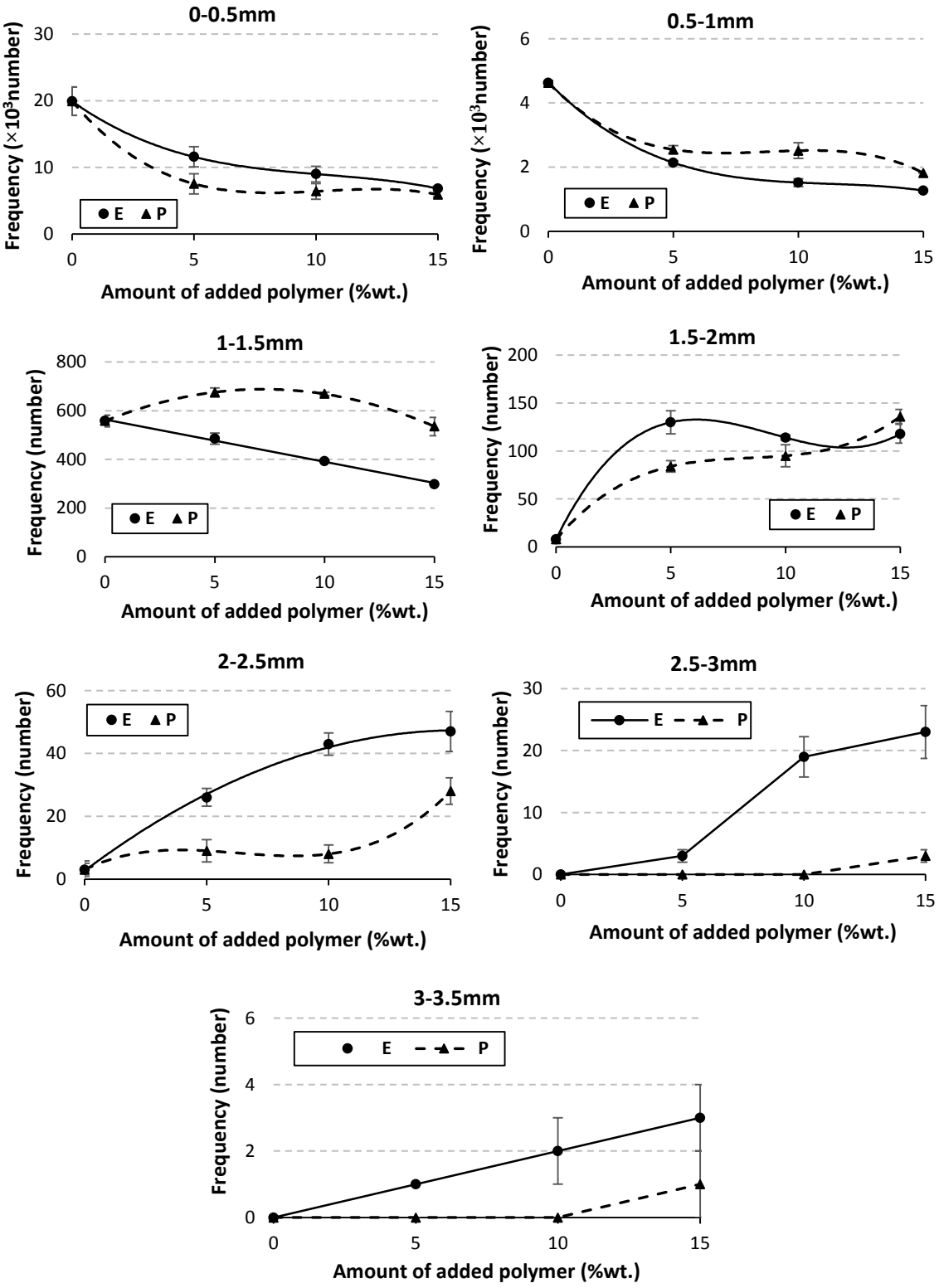

Figure 6-8: The effect of the concentration of the added polymer on the number-weighted frequency of each size range

The frequencies of larger bins (i.e. 2-2.5, 2.5-3, and 3-3.5mm) increased significantly with increasing the concentration of the low melt strength EVA over the entire concentration range. PEO did not introduce a significant increase in the frequency of these bins except for the 2-2.5mm bin whose frequency increased when adding 15%wt. PEO.

The cellular structure characteristics of the developed foam samples are listed in Table 6-5. It is clear that porosity did not change among the foam samples, and the variations were within the experimental error range. The same behavior was observed for tortuosity, which did not change significantly. The throat size increased by about 15µm when adding PEO compared to an increase of about 35µm when adding the low melt strength EVA grade. The addition of any of the two polymers increased the average cell size as show in Figure 6-9, as a result of their influence on reducing the frequencies of the small and the mid-size cells. Unlike the volume-weighted average cell size, which was larger for the low melt strength EVA grade, the number-weighted average cell size for PEO was larger than that of EVA. This can be attributed to the effect of adding PEO on increasing the frequencies of the mid-size and the large bins. Since these bins are characterized by a large number of cells, they contribute significantly to the number-weighted average cell size. The addition of the low melt strength EVA grade, on the other hand, increased the frequency of the large bins (2-2.5, 2.5-3, and 3-3.5mm). These bins do not influence the number-weighted average cell size as they contain a few number of cells.

Table 6-5: The cellular structure characteristics of the developed foam samples

Property	**Sample code**						
	5E	**10E**	**15E**	**5P**	**10P**	**15P**	**Neat sample**
Porosity (%)	93.01±0.40	92.29±0.34	92.84±0.05	91.91±1.56	91.62±0.97	91.44±0.96	90.58±1.18
Cell density (cell/cm^3)	8.59×10^3 (±167)	6.63×10^3 (±637)	5.13×10^3 (±230)	6.49×10^3 (±261)	5.79×10^3 (±516)	5.04×10^3 (±330)	1.50×10^4 (±340)
Cell size (µm)	331±27	342±22	361±17	406±19	433±16	415±18	293±33
Throat size (µm)	105±9	99±11	105±8	79±12	76±8	80±10	65.56±15
Tortuosity	1.19±0.08	1.31±0.15	1.43±0.24	1.17±0.05	1.19±0.08	1.31±0.10	1.65±0.05

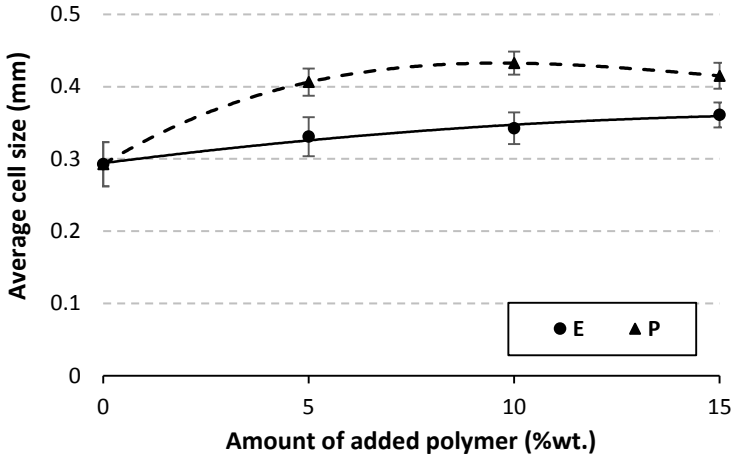

Figure 6-9: The effect of the concentration of the added polymer on the number-weighted average cell size

The effect of the concentration of the added polymer on the cell density is displayed in Figure 6-10. The graph shows that increasing the concentration of any of the two polymers reduced the cell density especially at the 5%wt concentration. This is mainly because of reducing the frequency of the small and the mid-size cells, which are large in number, through converting them into a smaller number of larger cells. Moreover, the reduction in the cell density at the 5%wt. and 10%wt concentrations was higher in the case of PEO compared to the low melt strength EVA. This was mainly due to the significant effect of adding PEO on reducing the frequency of the 0-0.5mm bin as shown in Figure 6-8.

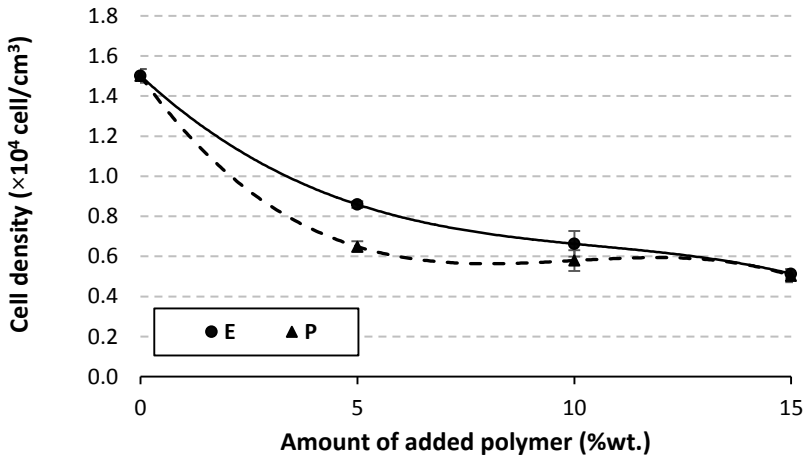

Figure 6-10: The effect of the concentration of the added polymer on the cell density of the developed foam samples

6.3.2 Acoustic measurements

Figure 6-11 shows the sound absorption curves of the foam samples prepared with the low melt strength EVA grade, while Figure 6-12 shows the sound absorption curves of the foam samples prepared with PEO. Each curve is the average of three different measurements with a standard deviation of ±0.05. Generally, the absorption curves of all of the developed foam samples had the same shape as that of the neat foam sample prepared without blending. The addition of 5%wt. of the low melt strength EVA increased sound absorption coefficient significantly over the frequency range extending from 177 up to 1420Hz. More specifically, the inclusion of 5%wt. of the polymer resulted in an increase in absorption coefficient by about 0.3 for all frequencies extending up to 1420Hz compared to the neat sample. The higher concentrations of the added polymer slightly increased sound absorption coefficient over the same frequency range. Increasing the concentration of the polymer from 5%wt. to 10%wt. or from 10%wt. to 15%wt. increased the absorption coefficient by less than 0.1. Above 1420Hz, sound absorption coefficients were almost the same for all foam samples prepared with the low melt strength EVA.

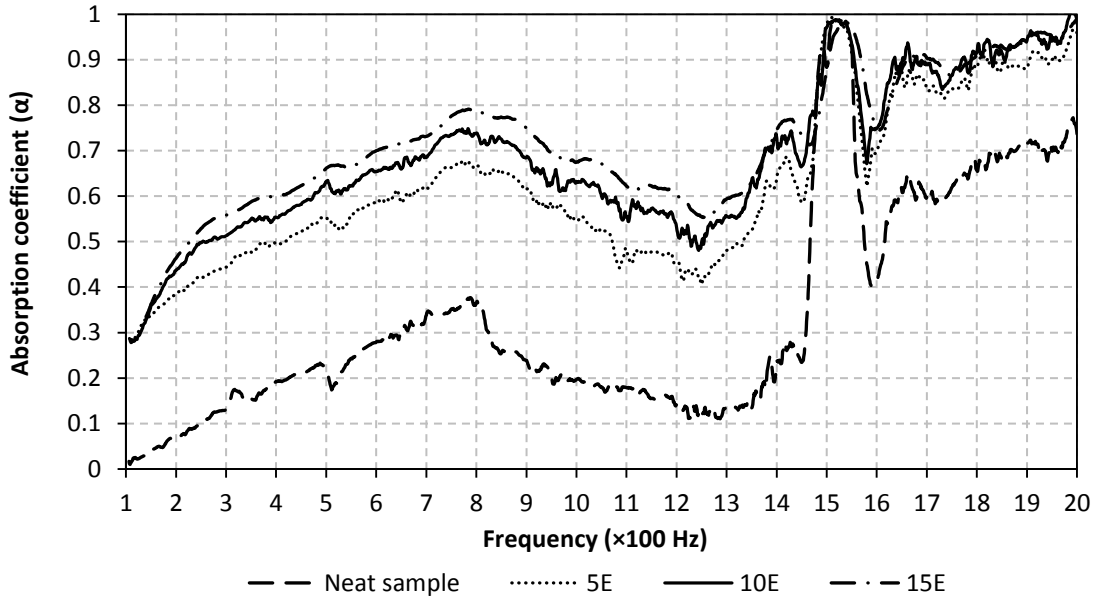

Figure 6-11: Sound absorption curves of the foam samples prepared by adding the low melt strength EVA grade; sample thickness=5cm

No significant improvement in sound absorption coefficient was observed when adding PEO, and the values were very close to these of the neat foam sample prepared without blending. As the concentration of PEO increased from 5, 10, to 15%wt., the absorption coefficient experienced a slight increase correspondingly. In fact, addition of PEO at the concentration of 15%wt. increased sound absorption coefficient by no more than 0.15 over the frequency range 100-1400Hz.

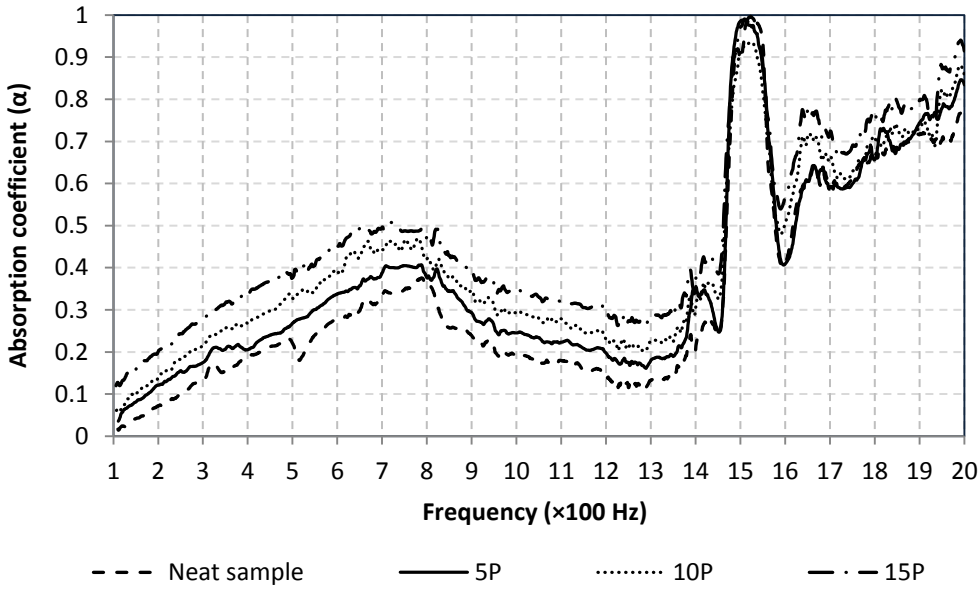

Figure 6-12: Sound absorption curves of the foam samples prepared by adding PEO; sample thickness=5cm

As shown in both figures, the absorption curves were characterized by two distinctive peaks. The values and the positions of these peaks are listed in Table 6-6. The first absorption peak was wide, and it occurred at 800Hz and 750 for the samples prepared with the low melt strength EVA and PEO respectively. Increasing the concentration of the low melt strength EVA grade shifted the absorption peak to a higher value; the peak value increased from 0.38, which was for the neat foam sample to 0.8 when adding 15%wt. The addition of 15%wt. of PEO, on the other hand, increased the peak value by only 0.1. The second absorption peak was narrow, and it occurred almost at 1525Hz for all of the developed foam samples. The values of the second absorption peak were nearly the same for all foam samples, and it had a value close to 1.

Table 6-6: The values and the positions of the sound absorption peaks

Sample code	First absorption peak		Second absorption peak	
	f (Hz)	α (-)	f (Hz)	α (-)
Neat sample	800	0.38	1525	0.98
5E	800	0.52	1525	1
10E	800	0.72	1525	1
15E	800	0.8	1530	0.98
5P	750	0.38	1525	0.98
10P	750	0.42	1525	0.93
15P	750	0.48	1525	0.98

To study the effect of the concentration of the added polymer on sound absorption coefficient over the octave bands 177-355, 355-710, and 710-1420Hz, sound absorption coefficient values at the central frequencies 250, 500, and 1000Hz were extracted from Figure 6-11 and Figure 6-12, and plotted as a function of the concentration of the added polymer for both the low melt strength EVA and PEO. The variation of sound absorption coefficient with the concentration of the added polymer at 250, 500 and 1000Hz are shown in Figure 6-13, Figure 6-14, and Figure 6-15, respectively.

For the low melt strength EVA grade, the sound absorption coefficients at the aforementioned frequencies fitted perfectly into a third order polynomial whose curve was characterized by a steep slope up to the concentration of 5%wt. followed by a slow rising slope over the concentration range extending from 5 up to 15%wt. The previous findings emphasized the conclusion that the addition of 5%wt. of the low melt strength EVA grade significantly increased sound absorption coefficient at these frequencies. Nevertheless, further increase of the polymer concentration introduced a slight increase on sound absorption coefficient. The experimental results showed that the addition of 5%wt. of the low melt strength EVA increased sound absorption coefficient from 0.11 to 0.42 at 250 Hz, from 0.20 to 0.56 at 500Hz, and from 0.20 to 0.55 at 1000Hz. Whereas increasing the concentration from 5%wt. up to 15%wt. increased sound absorption coefficient by no more than 0.14 over the frequency range 177-1420Hz.

For the foams samples prepared with PEO, it was found that sound absorption coefficients at the aforementioned frequencies fitted perfectly into a line characterized by a small slope. In fact, the addition of PEO at any concentration did not enhance sound absorption coefficient, and the increase in sound absorption values was within the experimental error range.

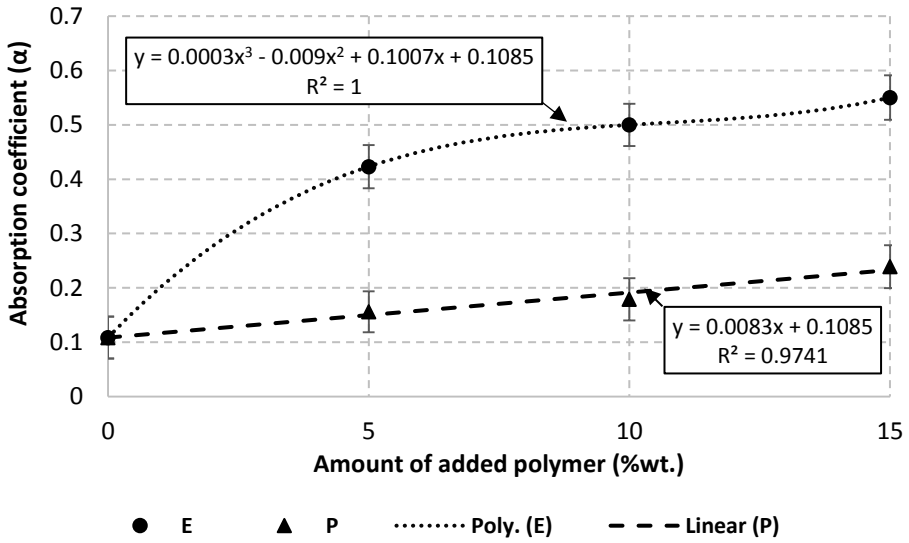

Figure 6-13: Variation of sound absorption coefficient with the concentration of the added polymer at 250Hz

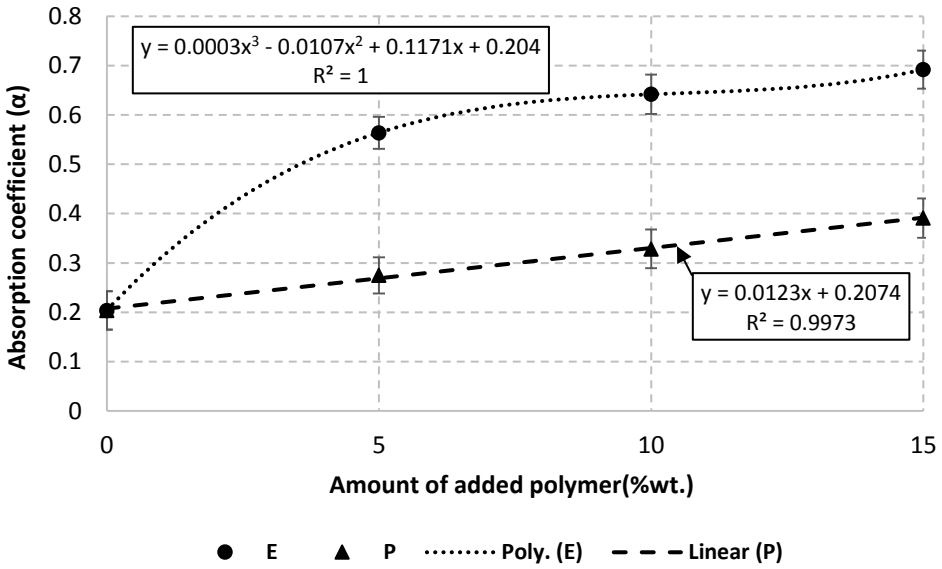

Figure 6-14: Variation of sound absorption coefficient with the concentration of the added polymer at 500Hz

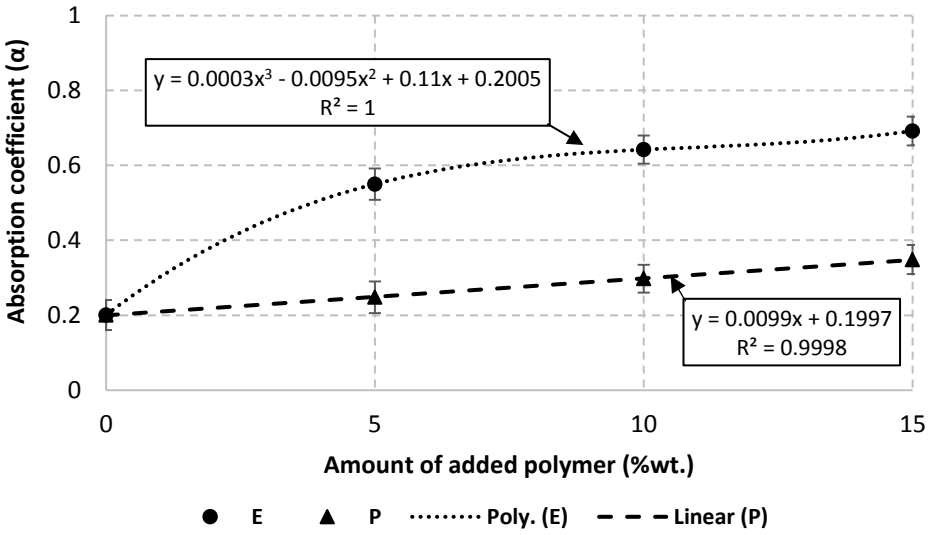

Figure 6-15: Variation of sound absorption coefficient with the concentration of the added polymer at 1000Hz

Static air flow resistivity, which is mainly dependent on the characteristics of foam cellular structure, is one of the most important properties that controls sound absorption coefficient. Therefore, static air flow resistivity of the developed foam samples were measured, and its variation with the concentration of the added polymer is shown in Figure 6-16 for both PEO and the low melt strength EVA grade.

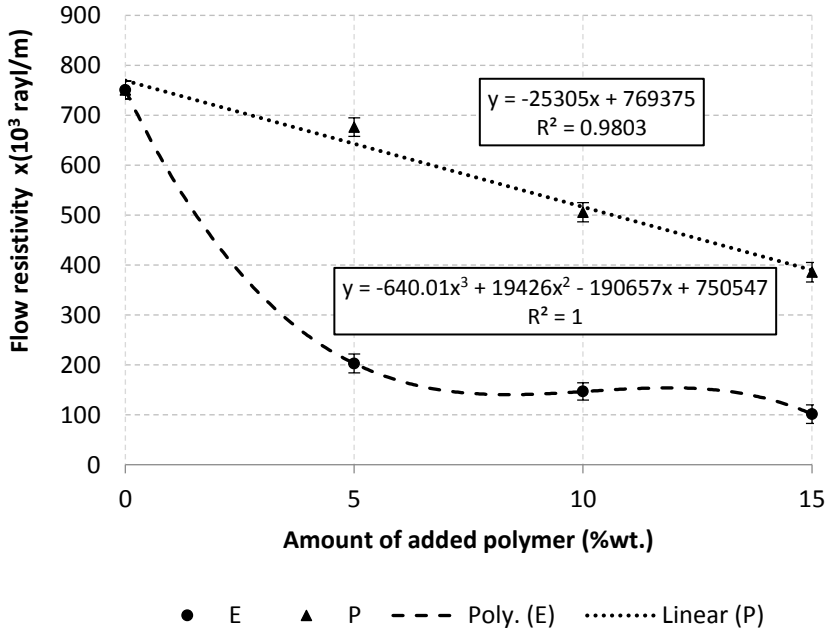

Figure 6-16: The effect of the concentration of the added polymer on air flow resistivity of the foam samples

The addition of 5%wt. of the low melt strength EVA significantly reduced air flow resistivity from 750,547 to 202,905rayl/m. Further increase of the polymer concentration resulted in a slight decrease in the air flow resistivity of the samples. On the other hand, the addition of PEO reduced the air flow resistivity linearly over the entire concentration range. Even though, its effect was less than that of the low melt strength EVA. The addition of 15%wt. of PEO reduced the air flow resistivity of the sample from 750,547 to 385,644rayl/m. The previous result shows that the reduction in air flow resistivity when adding 15%wt. PEO was even less that that occurred when adding 5%wt. of the low melt strength EVA grade.

By referring to Figure 6-8, it turns out that the improvement in sound absorption coefficients of the samples prepared with the low melt strength EVA is due to the fact that its addition resulted in decreasing the frequency of the small and the mid-size cells. In turn, a very large cells, with size ranges 2-2.5mm, 2.5-3mm, and 3-3.5mm, were formed. These large cells played an important role in reducing the air flow resistivity of the samples. Such reduction in air flow resistivity was reflected on decreasing the acoustic impedance at the material surface and enhancing the interaction of sound waves with the foam internal structure, which led ultimately to more sound dissipation. Also, these large cells are characterized by large surface area which took part in dissipation of sound energy of the low frequency through exchanging heat with the foam-saturating fluid.

The effect of adding PEO on the developed cellular structure was a little bit different from that of the low melt strength EVA. It showed the same effect on reducing the frequency of the small size bins (0-0.5, and 0.5-1mm). In turn, it increased the frequency of the cells with sizes 1-1.5 and 1.5-2mm. the addition of PEO did not affect the population of cells larger than 2mm. Merely, these variations was not sufficient to reduce the air flow resistivity of the samples to a significant extent. The high values of air flow resistivity of these samples increased sound reflection at the material surface, which in turn reduced sound absorption coefficients.

Both PEO and the low melt strength EVA influenced the developed cellular structure but in different ways. This difference might be attributed to the difference in the particle size of the raw polymers. PEO was incorporated in the form of a very fine powder with particle sizes less than 106μm. After mixing and melting, PEO formed very small domains dispersed within the main polymer matrix. The coalescence of cells in these small size domains reduced the number of small cells and increased the number of the mid-size cells. Nevertheless, it was not able to develop cells with sizes larger than 2mm. On the other hand, the low melt strength EVA was incorporated in the form of a powder with particle sizes ranging between 250 and 500μm. After mixing and melting, the polymer was dispersed within the main polymer matrix in the form of relatively large domains. The coalescence of cells in these large domains developed cells with sizes greater than 2mm.

6.4 Summary and Conclusion

In this chapter, heterogeneous thermoplastic foams with a combination of small cells and large cells were developed through foaming of a blend consisting of a foamable EVA grade (9%VA) with another low melt strength polymer by a two-stage foaming process. PEO and the low melt strength EVA (18%VA) were used for blending, and the concentration was varied from 0, 5, 10, to 15%wt.

Experimental results showed that both PEO and the low melt strength EVA altered the developed cellular structure but in different ways. Both polymers reduced the frequencies of the small and the mid-size bins (0-0.5, and 0.5-1mm). The addition of PEO increased the frequency of bins with ranges 1-1.5 and 1.5-2mm, whereas it had almost no influence on the cell larger than 2mm. The addition of the low melt strength EVA increased the population of the cells larger than 2mm. This occurred at the cost of reducing the frequency of all cells below 1.5mm. These variations in the cell size distribution shifted the average cell size of the develop foam samples to higher values. Also, the average throat size experienced a slight increase when adding any of the two polymers. However, neither open porosity nor tortuosity changed significantly when adding any of the two polymers.

The absorption curves of the developed foam samples had the same shape as that of the neat foam sample that was prepared without blending. However, they were shifted to higher values. The addition of 5%wt. of the low melt strength EVA increased sound absorption coefficient by about 0.3 at all frequencies extending from 177 up to 1420Hz. The higher concentrations of the polymer slightly increased the absorption coefficient over. Sound absorption coefficient was almost the same for all foam samples above 1400Hz. The addition of PEO did not improve sound absorption coefficient, and the values were very close to these of the neat foam sample. Adding 15% of PEO increased sound absorption coefficient by no more than 0.14 over the frequency range 177-1420Hz.

Obviously, developing cells larger than 2mm within the foam cellular structure, through the addition of the low melt strength EVA, was very helpful in reducing the air flow resistivity of the foams samples. Such reduction in samples air flow resistivity decreased sound reflection at the material surface and increased the interaction of the sound waves with the foam internal structure leading to more sound dissipation. The addition of PEO, on the other hand, was not successful in developing such large cells, and the air flow resistivity of the sample was therefore high. The high values of air flow resistivity increased sound reflection at the material surface and reduced sound absorption coefficient.

Chapter 7 Development of Graded Porosity Thermoplastic Foams

7.1 Introduction

Functionally graded materials (FGMs) consist of two or more constituent phases with a continuously varying composition. Since all of the material properties, such as mechanical, thermal, acoustic, electrical, and optical, are principally function of composition, a gradual variation in composition and microstructure can be useful for obtaining higher specific properties such as impact strength, abrasion resistance, and superficial hardness [128]. The continuous variation in the microstructure of such materials discriminates them from laminated composite materials, which normally experience mechanical properties mismatch, and delamination problem at the layers interface as a result of the discrete variation in properties among the constituting layers. The unique characteristics of FGMs made them optimum choice for application such as energy conversion, coating, biomaterials, and commodities [185]. Graded porosity foams are a special category of FGMs where porosity changes continuously across the thickness of the foamed article due to the change in cell size and cell density.

In this work, the temperature gradient approach was used in a two-stage foaming process 'compression molding-oven foaming' to produce open cell thermoplastic foams with graded porosity for sound absorption application. The process is shown schematically in Figure 7-1. In the first stage of the process, a temperature gradient is applied during molding the sample to induce heterogeneous nucleation across the molded part. After that, the pre-foamed part is expanded in a heating oven to obtain the final porosity, thickness, and shape of the foamed part. The effects of the temperature difference and the molding time were studied in terms of the developed porosity profile. Additionally, the acoustic performance of the developed foam samples was examined over the frequency range extending from 100 to 2000Hz.

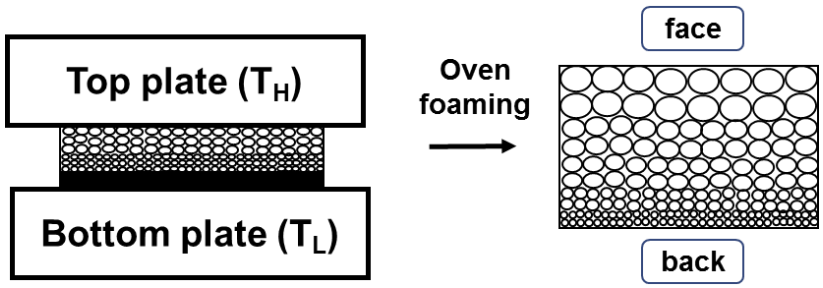

Figure 7-1: Strategy used to develop graded porosity open cell thermoplastic foams

7.2 Experimental Work

7.2.1 Sample preparation

Graded porosity foams were developed by a three-step process. In the first step, specified amounts of the EVA grade with 9% VA, Celogen OT, DOP, and wollastonite, according to Table 7-1, were dry mixed in a plastic bag to obtain a homogeneous mixture. Then, 25g of the prepared powder was weighed and placed inside a cylindrical aluminum mold having dimensions of 110mm diameter×3mm height. The mixture was compression molded in a Carver hot press at a temperature of 115^{o}C using a constant pressure of 1000 psi for 20 minutes. The mold was heated first without applying any pressure for 10 min to soften and sinter the powder. After that, a pressure of 1000psi was applied and released instantaneously for ten times to remove any entrapped air bubbles. After completing this step, the mold was kept closed under a pressure of 1000psi for additional 10 min. The mold was finally removed from the press, and cooled in air for 5 min.

Table 7-1: Compositions used to produce graded porosity foams

Ingredient	Concentration (%wt.)	Amount (g)
EVA (9% VA)	-	23
Celogen OT	10%	2.3
DOP	0.5%	0.12
Wollastonite	1%	0.23

In the second step, heterogeneous nucleation of the molded sample was conducted by compression molding the sample under a temperature gradient for a period of time. The temperatures of the upper (T_H) and bottom (T_L) plates of the compression press were

adjusted to two different values, with the highest temperature on the top plate in all experiments. The mold was then inserted into the press and compression molded under a pressure of 1000psi for a specified period of time before releasing the pressure and cooling the mold. All the conditions used to produce the foam samples in this work are listed in Table 7-2. The minimum temperature of lower plate was set to 80°C, as lower values did not initiate prefoaming. While, the maximum temperature of the upper plate was set to 140°C as higher values led to the complete decomposition of the chemical blowing agent. Similarly, the minimum molding time sufficient to initiate prefoaming was found to be 2 min, whereas the upper bound before the occurrence of complete decomposition of the chemical blowing agent was found to be 4 min.

Table 7-2: The processing conditions used to induce heterogeneous prefoaming

Sample code	**T_L (°C)**	**T_H (°C)**	**ΔT (°C)**	**Time (min)**
A	115	115	0	2 and 4
A30-2	100	130	30	2
A30-4	100	130	30	4
A40-2	100	140	40	2
A40-4	100	140	40	4
A50-2	80	130	50	2
A50-4	80	130	50	4
A60-2	80	140	60	2
A60-4	80	140	60	4

In the last step, the pre-foamed sample was expanded in a heating oven to achieve the required expansion ratio. To this end, the sample was transferred into a larger mold having the same diameter, but with a 36mm depth. The mold was closed by two 2″ C-clamp and inserted into a heating oven working at 156^{o}C for 26 min. By the end of the foaming time, the mold was removed from the oven, and cooled in water maintained at 25^{o}C before dismantling it. The use of 10%wt. Celogen OT achieved an expansion ratio of 12. Since the diameters of both molds were the same, this expansion ratio increased the thickness of the sample from 3mm to 36mm.

7.2.2 Porosity profile measurement

The micro-CT technique was used to measure the porosity profile developed across each foam sample. For each set of experimental conditions, three different specimens with dimensions 30mm height×16mm diameter were prepared. Since it was not possible to scan such long specimens, each specimen was further divided into two halves and each half was scanned by the large camera, which has a pixel size of 25μm. This produced 600 images with a resolution of 640×640pixels. A number of custom image processing steps, listed in Table 7-3, was applied to the constructed images to extract the porosity profile developed across each foam sample. Since closed porosity was negligible in all foam samples, closed pores were removed, and in that case the total porosity calculated in 2D represented the open porosity in each image directly

Table 7-3: A list of custom image processing operations used to extract porosity profile

Process	Sub-process	Function
Thresholding	Global (5-255)	Convert gray scale image into binarized image
Despecle	Sweep all except the largest object (3D)	Rectify the foam skeleton by removing any isolated object
Despecle	Remove pores (3D)	Remove closed pores (3D)
2D analysis	2D analysis	Calculate porosity of each image

7.3 Results and Discussion

7.3.1 Porosity profile characterization

The porosity profile developed across each foam sample is shown in Figure 7-2. It is clear that porosity at the lower surface was between 83 and 85%, while it was between 80 and 93% at the upper surface for all foam samples. The porosity gradient (i.e. the slope of the line) of the sample designated A, which was not exposed to a temperature gradient during the prefoaming step, was almost zero. The porosity gradient increased with increasing the temperature gradient applied across the sample during molding. However, the molding time had negligible effect on the developed porosity gradient.

To study the effect of the molding time and the molding temperatures on the porosity gradient developed across each foam sample, porosity at the lower and upper surfaces of each sample was extracted from Figure 7-2, and the difference between these two values, which is proportional to the porosity gradient, was plotted versus the imposed temperature difference as shown in Figure 7-3.

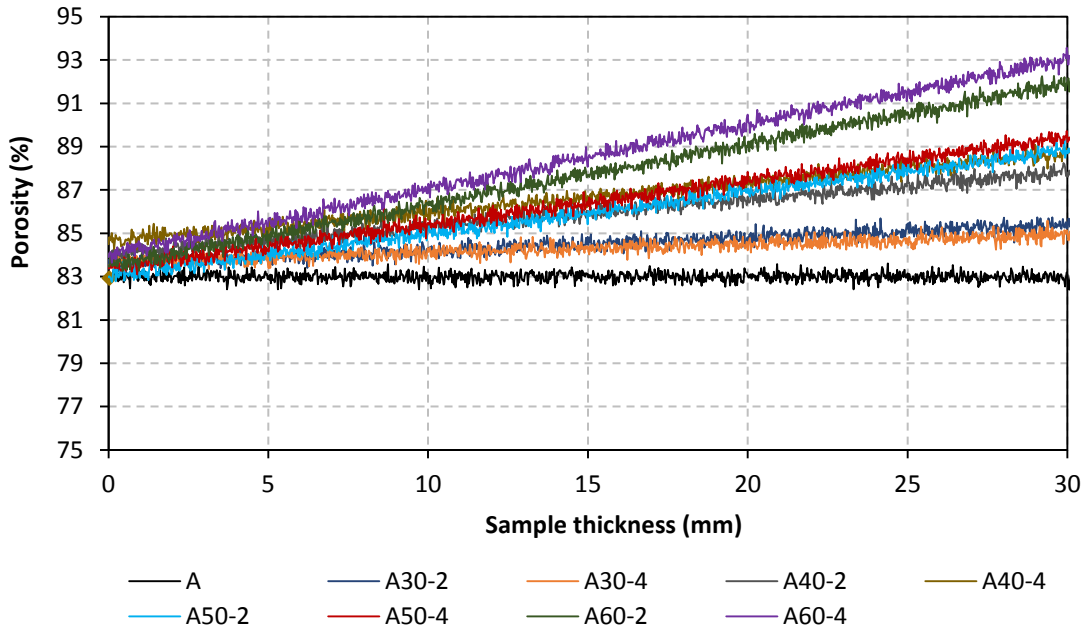

Figure 7-2: Porosity profiles of the developed foam samples

It is clear that applying the same temperature gradient for different periods of time (2min or 4min) had negligible effect on increasing the porosity gradient, and the difference was within the experimental error range. On the other hand, increasing the temperature gradient increased the porosity difference almost linearly. For the sample that was pre-foamed for a period of 4 min, applying a temperature difference of 30°C increased its porosity difference by 2.36% (sample designated as A30-4). A temperature difference of 40°C achieved porosity difference of 4.48% (sample designated as A40-4), while 50°C temperature difference achieved porosity difference of 6.34% (sample designated as A50-4). The highest porosity difference achieved was for the sample designated as A60-4 which exhibits a porosity difference of 9.1% after molding it under a temperature difference of 60°C for 4 min.

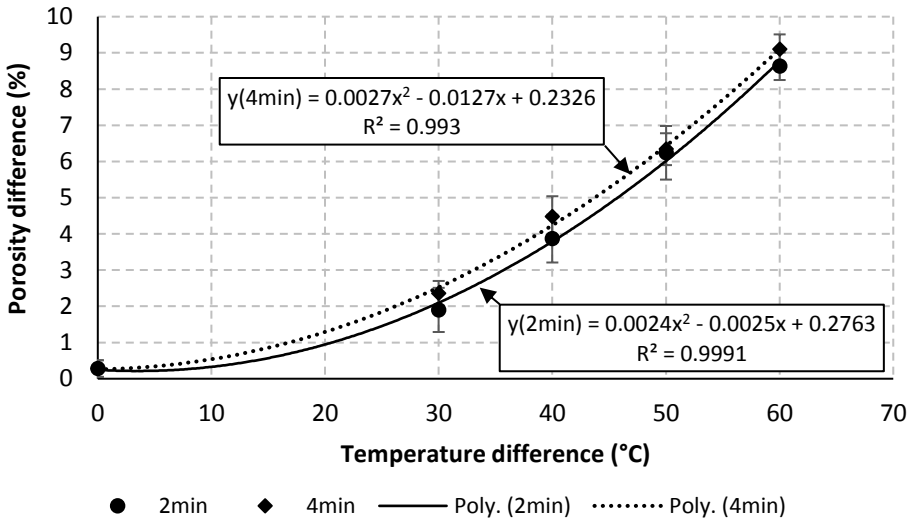

Figure 7-3: The effect of the applied temperature difference on the porosity difference between the upper and the lower surfaces of the foam sample

The average porosity of the developed foam sample is shown in Figure 7-4. A plot of the variation of average porosity with the temperature gradient imposed during molding is also shown in Figure 7-5. Since the molding time had negligible effect on the developed porosity profile, average did not change when changing the molding time. On the other hand, the average porosity increased with increasing the temperature gradient applied across the sample during molding except for the samples pre-foamed under temperature gradients of 40 and 50°C. Without applying any temperature difference across the sample, the average porosity was 82.99±0.20% (sample designated as A). Applying a temperature difference of 30°C for 4 min increased the average porosity of the foam sample to 84.54±0.57% (sample designated as A30-4). For the foam sample designated as A40-4, the average porosity reached 86.69±1.22% when applying a temperature difference of 40°C for 4 min. The average porosity of the foam sample exposed to a temperature difference of 50°C for 4 min (sample designated as A50-4) was 86.52±1.81%. The maximum average porosity was achieved when a temperature difference of 60°C was imposed for 4 min. across the sample during the prefoaming step. For this case, the average porosity was 88.69±2.71% (sample designated as A60-4).

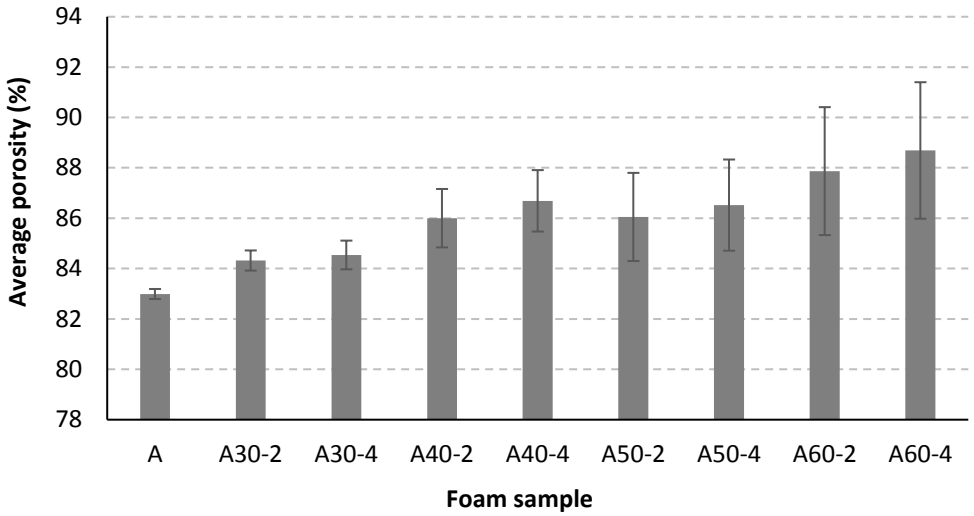

Figure 7-4: The average porosity of the developed foam samples

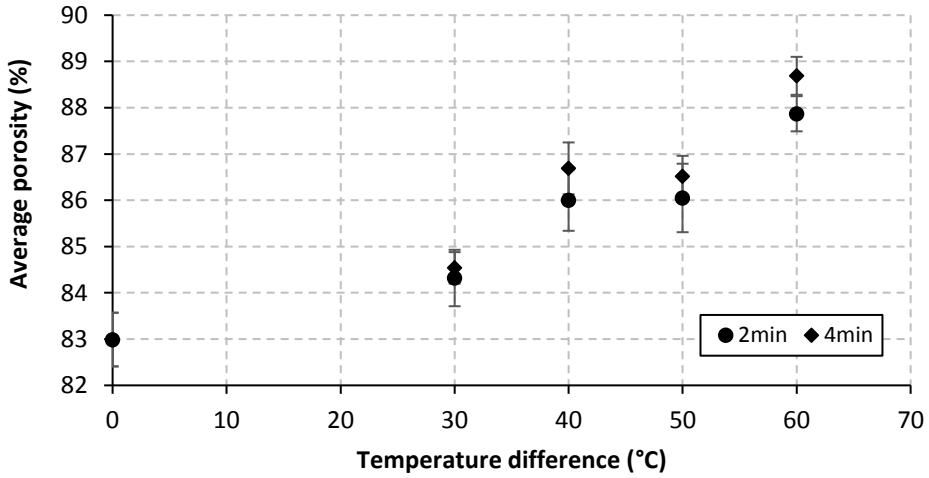

Figure 7-5: The effect of the applied temperature difference on the average porosity of the developed foam samples

7.3.2 Acoustic measurements

To acoustically examine the existence of porosity gradation across the developed foam samples, sound absorption coefficient was measured at the two sides (i.e. face and back) of each foam sample, and the results were compared with each other. As shown in Figure 7-6, sound absorption curves measured at the face and the back of the sample designated as A coincide meaning that the sample is homogeneous.

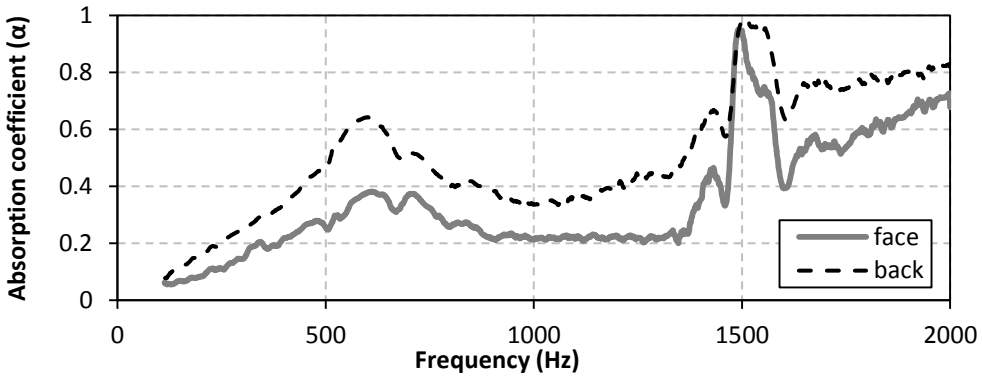

Figure 7-6: Sound absorption coefficient measured at the face and at the back of a 3.6cm thick foam sample A (ΔT=0°C, t=4min)

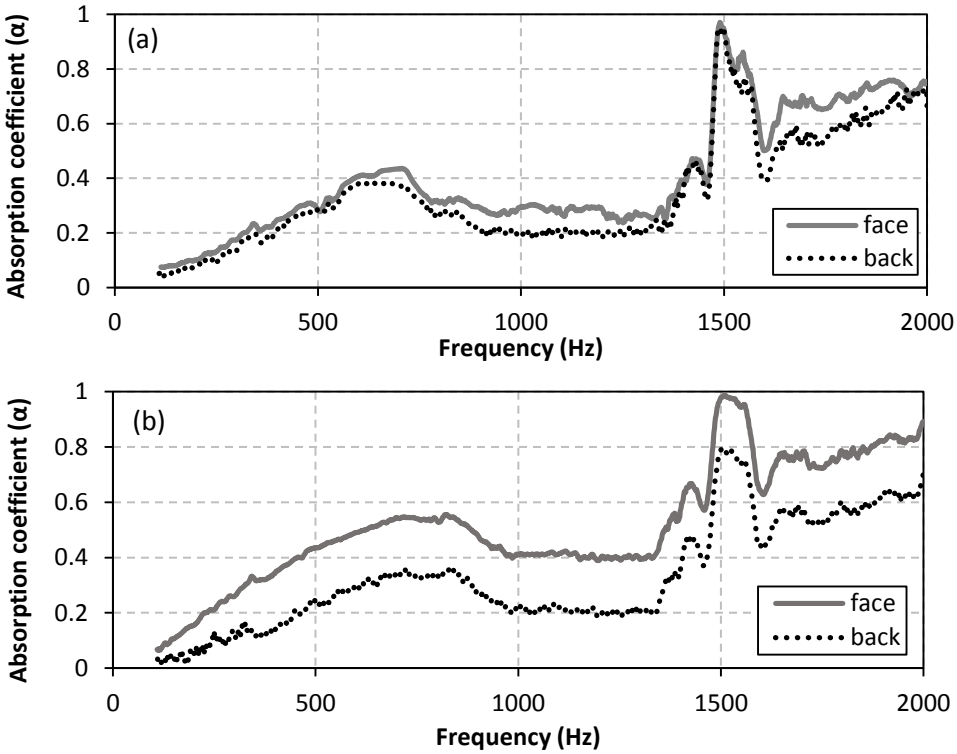

Figure 7-7: Sound absorption coefficient measured at the face and at the back of 3.6cm thick sample: (a) A30-2 (ΔT=30°C, t=2min), and (b) A30-4 (ΔT=30°C, t=4min)

The same behavior was observed in Figure 7-7 for the foam samples pre-foamed under a temperature difference of 30°C (A30-2 and A30-4). This means that imposing a temperature difference of 30°C across the sample for 2 or 4 min was not sufficient to produce gradation in porosity. Increasing the temperature difference imposed across the sample to 40°C led to the emergence of noticeable gradation in porosity, with the highest value at the sample surface facing the hot plate of the press (face) and the lowest value at

the sample surface facing the plate with the lower temperature (back). As shown in Figure 7-8, sound absorption coefficient measured at the face of samples designated A40-2 and A40-4 was higher than the value measured at their back. The same behavior is shown in Figure 7-9 for the samples designated as A50-2 and A50-4, and in Figure 7-10 for samples designated as A60-2 and A60-4. When the foam sample was placed with the face fronting the incident sound wave, the high porosity at the surface reduced the acoustic impedance at the material surface and minimized sound reflection. Conversely, placement of the foam sample with the back confronting the incident sound wave increased the acoustic impedance at the material surface and increased sound reflection.

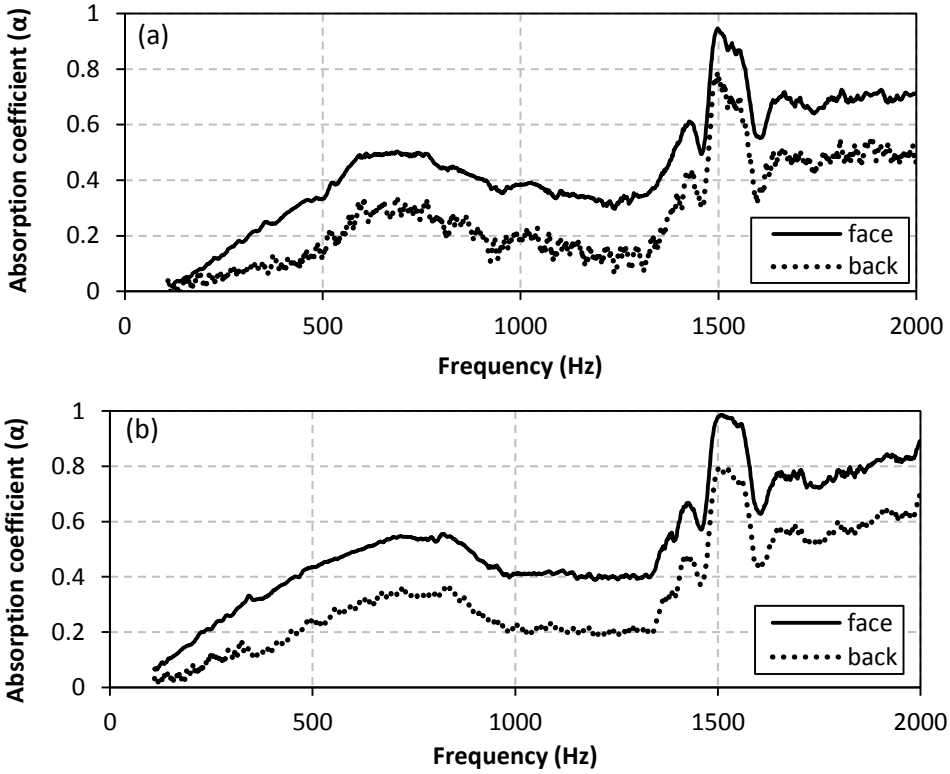

Figure 7-8: Sound absorption coefficient measured at the face and at the back of 3.6cm thick sample: (a) A40-2 (ΔT=40°C, t=2min), and (b) A40-4 (ΔT=40°C, t=4min)

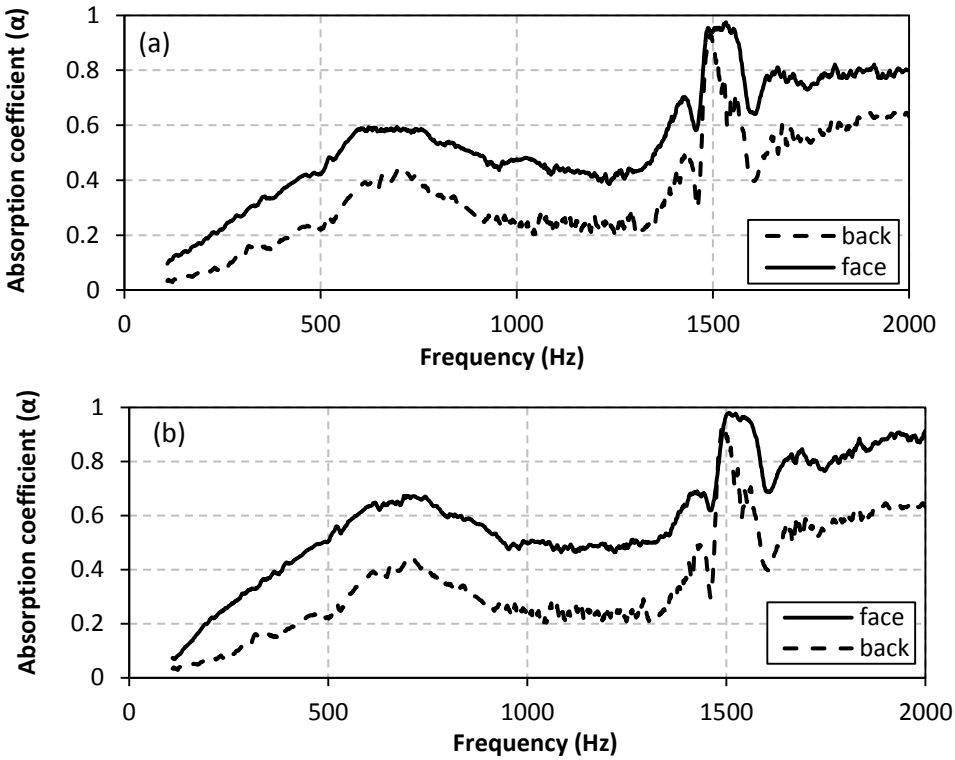

Figure 7-9: Sound absorption coefficient measured at the face and at the back of 3.6cm thick sample: (a) A50-2 (ΔT=50°C, t=2min), and (b) A50-4 (ΔT=50°C, t=4min)

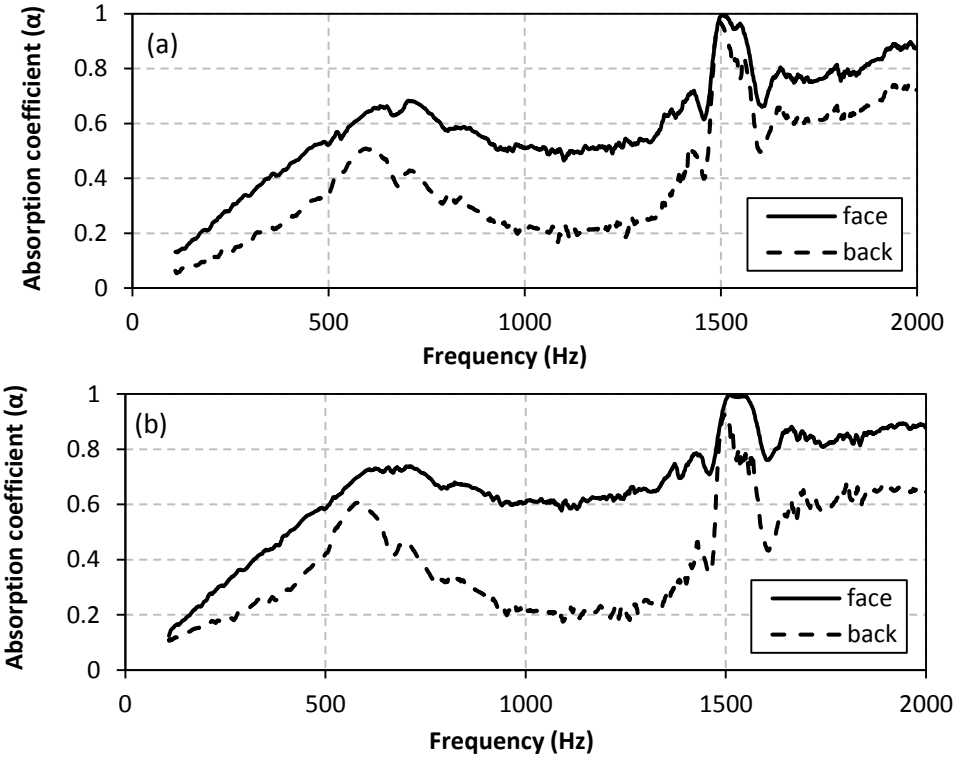

Figure 7-10: Sound absorption coefficient measured at the face and at the back of 3.6cm thick sample: (a) A60-2 (ΔT=60°C, t=2min), and (b) A60-4 (ΔT=60°C, t=4min)

Comparison between sound absorption curves of the developed foam samples which were measured with the sample face fronting the incident sound wave are shown in Figure 7-11. All the curves showed the same pattern, with a linear region over the frequency range 100-600Hz, followed by a hump (i.e. a wide absorption peak) located between 600 and 800Hz. The curve has also a flat plateau region between 800-1300Hz followed by a high narrow absorption peak located between 1490 and 1580Hz.

Generally speaking, increasing the temperature difference and/or the molding time increased sound absorption coefficient over the frequency range extending from 177 to 1420Hz. The effect of the temperature difference on sound absorption coefficient was studied at three different frequencies: 250, 500, and 1000Hz which represent the central frequencies of the octave bands 177-355, 355-710, and 710-1420Hz respectively. The results are displayed as a plot of sound absorption coefficient versus the applied temperature difference in Figure 7-12.

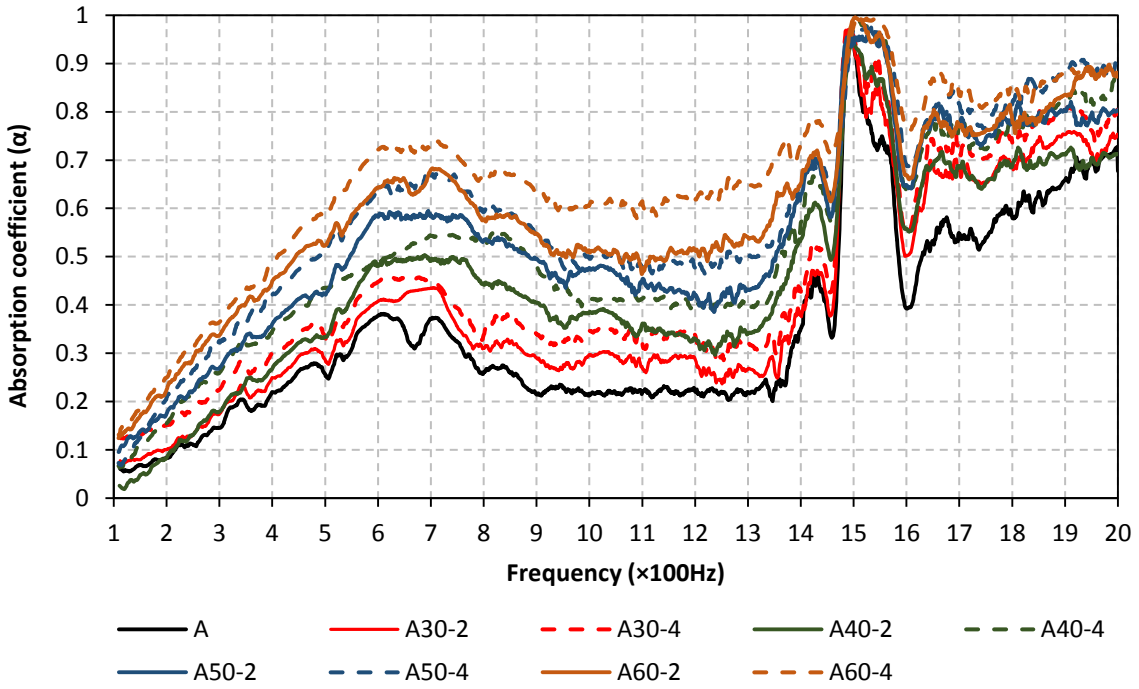

Figure 7-11: Sound absorption curves of the developed foam samples; with the face fronting the incident sound wave and sample size=3.6cm

It is clear that sound absorption coefficient increased progressively with increasing the temperature difference imposed across the sample. Imposing a temperature difference of 60°C across the sample for 4min increased sound absorption coefficient at 250Hz from 0.12 to 0.33, while it increased sound absorption coefficient at 500Hz from 0.26 to 0.59. Furthermore, sound absorption coefficient at 1000Hz increased from 0.25 to 0.62.

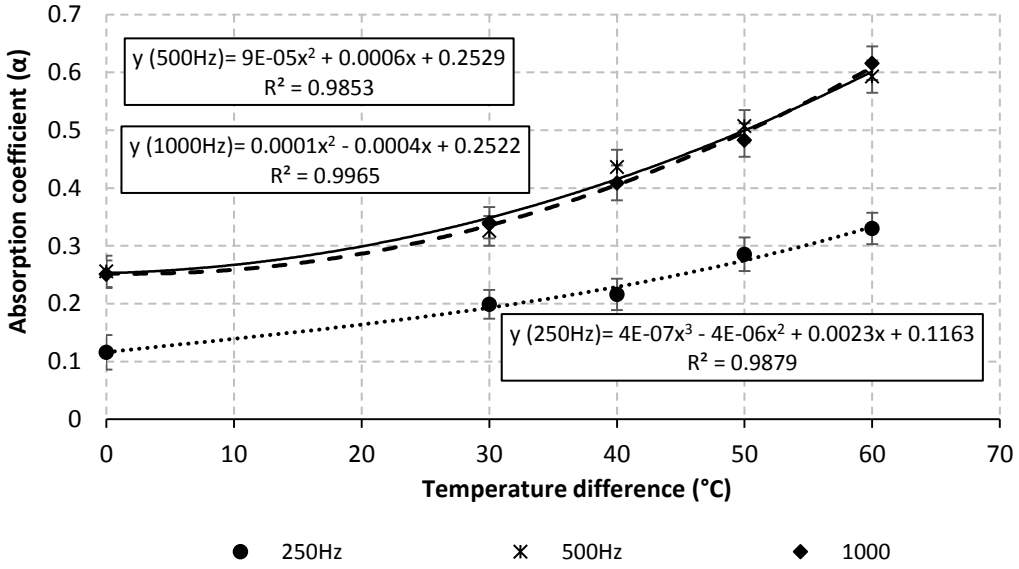

Figure 7-12: Variation of sound absorption coefficient with the applied temperature difference at the central frequencies 250, 500, and 1000Hz

Since static air flow resistivity is considered a key factor that controls the performance of acoustic foams for sound absorption, it was measured for the developed foam samples, and the results are presented in Figure 7-13 It is obvious from Figure 7-13 that the values of air flow resistivity for the samples designated A, A30-2, and A30-4 were high and close to each other. Air flow resistivity decreased with increasing the temperature difference imposed across the sample. Increasing the temperature difference from 40 to 50°C reduced air flow resistivity from 136,397 (sample designated A40-4) to 99,198rayls/m (sample designated A50-4). The maximum reduction in air flow resistivity happened when a temperature difference of 60°C was imposed across the sample designated A60-4, and its value reached 61,998 rayl/m. The reduction in air flow resistivity may be attributed to the increase of the average porosity, which in turn increased with increasing the temperature difference imposed across the samples during prefoaming.

The flow resistivity measurements are in good agreement with the acoustic measurements of the developed foam samples. The increase in the temperature difference imposed across the samples increased the average porosity of the sample leading to reduction of its air flow resistivity. The reduction of air flow resistivity minimized sound reflection at the material surface, and increased sound absorption coefficient.

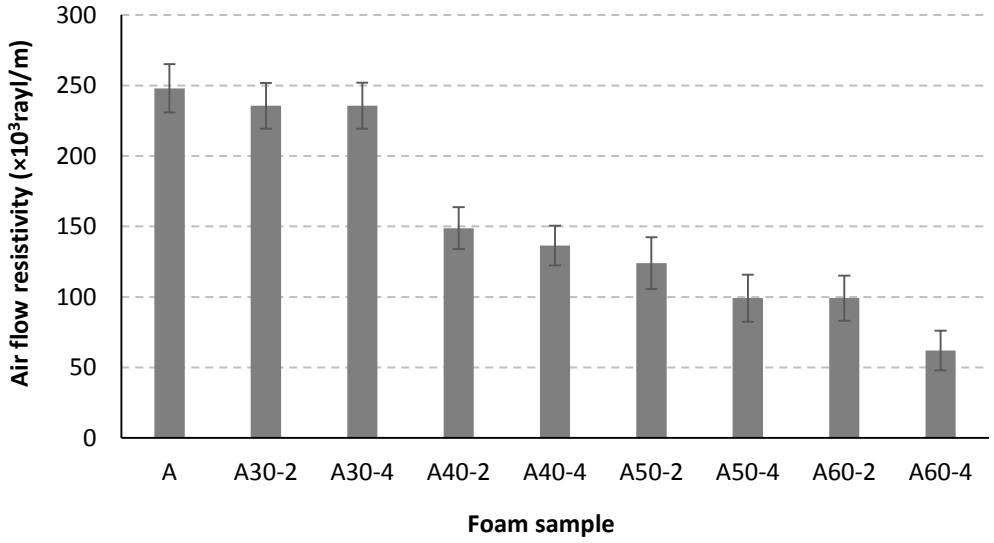

Figure 7-13: The air flow resistivity of the developed foam samples

7.4 Summary and Conclusion

In this work, thermoplastic foams with graded porosity were developed by applying different temperature gradients and molding times in a two-stage foaming process including compression molding and oven foaming. Experimental results showed clearly that the molding time had insignificant effect on the porosity profile developed across the foam samples. Increasing the temperature gradient imposed across the sample increased the porosity gradient developed. Also the average porosity of the sample increased with increasing the temperature gradient. This in turn was reflected on the reduction of air flow resistivity of the developed foam samples. Regarding acoustic measurements, it was found that sound absorption coefficient measured at the face of all foam samples, except for samples designated A, A30-2, and A30-4, was different from that measured at its back. This was attributed to the presence of porosity profile with the highest porosity at the

surface and the lowest porosity at the back. Last, it was found that sound absorption coefficient increased with increasing the temperature gradient over three octave band. Such increase in sound absorption coefficient was in part because of the reduction in the samples air flow resistivity in addition to the formation of porosity gradient across the samples. Higher porosity value at the surface minimized sound reflection at the surface and facilitated the accessibility of sound wave into the material. Meanwhile, the continuous decrease in porosity increased the acoustic impedance gradually leading to more dissipation of sound wave.

Chapter 8 Summary, Contributions and Fututre Work

8.1 Summary

Heterogeneous thermoplastic foams provide an efficient and economic solution to the problem of the low frequency noise, which constitutes a challenge to automotive, transportation, and building industries. A number of methods and concepts have been proposed to produce these materials. However, all methods of fabrication, reported in literature, use either batch processes which have long processing times and produce small sized samples, or produce foams that are not suitable for sound absorption applications. In this context, the work presented aimed at manufacturing of thermoplastic foams with double porosity and graded porosity for acoustic applications by using processes that can potentially be scaled up for large scale production.

8.2 Thesis Contributions

The main technical contributions of the thesis can be summarized in the following:

(1) Development of three different strategies for fabricating heterogeneous thermoplastic foams

Three different approaches were applied in a two-stage foaming process 'compression molding-oven foaming' to produce thermoplastic foams with heterogeneous cellular structures. Double porosity thermoplastic foams were developed through foaming of a low melt strength polymer in presence of additives such as sodium bicarbonate and wollastonite. Also, double porosity foams were developed through foaming a blend consisting of a base polymer and another low melt strength polymer. A third approach was utilized to develop graded porosity thermoplastic foams by molding the sample under a temperature gradient, to induce heterogeneous nucleation, followed by expansion in a heating oven. Compared to batch processes such as gas foaming and salt leaching, the proposed approaches are promising for application on a large scale for many reasons. They have lower processing time (less than 1 hour). Also, large samples

can be fabricated by these approaches, in addition the produced foams possess good mechanical properties.

(2) Development of thermoplastic open celled foams for acoustic applications

Sound absorption applications requires materials with high open cell content (greater than 75%) to achieve good performance. The majority of open cell foams available in the market are produced with non-recyclable thermosetting polymers such as polyurethane and melamine. Fabrication of open cell thermoplastic foams is of great interest for environmental considerations. However, fabrication of open cell thermoplastic foams is challenging, and it requires application of a certain strategy, such as partial crosslinking, mechanical crushing or blending with incompatible polymers, to increase the open cell content. In this work, thermoplastic foams with open porosity of about 88% were fabricated by a simple foaming process that did not include any of cell opening strategies thanks to the proper selection of the raw materials and the processing parameters.

(3) Development of open celled thermoplastic foams with double porosity and graded porosity

Heterogeneous thermoplastic foams with porosity of 88% were developed successfully in this thesis. Foaming of the low melt strength EVA grade (18%VA) in presence of 1%wt. wollastonite and 1%wt. sodium bicarbonate produced a cellular structure consisting of a combination of large cells (greater than 2mm) and small cells (less than 0.5mm). Likewise, cells larger than 2mm were developed within a finer cellular structure through foaming of a blend of a foamable EVA grade (9%VA) and another low melt strength EVA grade (18%VA). A graded porosity foam, with porosity difference of 9%, was developed by applying a temperature gradient of 60°C for 4 min across the samples during molding.

(4) Improving noise reduction over the frequency range 100-2000Hz

All of the thermoplastic foams developed in the thesis exhibit an increase in sound absorption coefficient by about three times over the frequency range extending from 177 up to 1420Hz compared to homogeneous samples. For example, sound absorption coefficient of the heterogeneous foam sample, produced with 1% sodium bicarbonate and 1% wollastonite, increased from 0.11 to 0.53 at 250Hz, from 0.21 to 0.72 at 500Hz, and from 0.20 to 0.61 at 1000Hz. In a similar way, the addition of 5%wt. of the low melt strength EVA grade increased sound absorption coefficient from 0.11 to 0.42 at 250 Hz, from 0.20 to 0.56 at 500Hz, and from 0.20 to 0.55 at 1000Hz. Last, imposing a temperature gradient of 60°C for 4min during molding of the sample increased sound absorption coefficient from 0.12 to 0.33 at 250Hz, from 0.26 to 0.59 at 500Hz and from 0.25 to 0.62 at 1000Hz.

(5) Using X-ray computed tomography for complete characterization of the cellular structure of thermoplastic foams

All the properties of the cellular structure, such as porosity, cell size, cell wall thickness, cell density, throat size, and tortuosity have been extracted by using X-ray computed tomography along with the image processing software 'Imorph'. These properties are very important for developing mathematical models capable of estimating the acoustic performance of these materials.

8.3 Recommendations for Future Work

The following recommendations can be made for the future research:

- Manufacture of graded porous thermoplastic foams in a one-stage process by applying a temperature gradient during compression molding foaming.
- Study the effect of adding different types of fillers, e.g. glass fibers, carbon nanotubes, graphene sheets, and wood fibers, on cellular structure, mechanical properties, and acoustic performance of thermoplastic foams.

- Using different types of low melt strength polymers for blending, and investigating the developed cellular structured in terms of polymer melt strength and blend morphology.
- Measure sound transmission loss of the developed bimodal and graded porous thermoplastic foams.
- Develop mathematical models that can estimate the acoustic performance of heterogeneous cellular thermoplastic foams in terms of their structural characteristics.

References

1. Müller, G., and Möser, M. (2012). Handbook of engineering acoustics, (Springer Science & Business Media).

2. Jansen, G. (1992). Auswirkungen von Lärm auf den Menschen. VGB Kraftwerkstechnik *72*, 60-64.

3. Kuttruff, H. (2000). Room acoustics, (New York, N.Y: Spon Press).

4. Fuchs, H. (2012). Applied acoustics: Concepts, absorbers, and silencers for acoustical comfort and noise control, (Springer).

5. Raichel, D.R. (2006). The science and applications of acoustics, (Springer).

6. Babuke, G., Leistner, P., Fuchs, H., and Zha, X. (2004). Structured molded parts for sound absorption. (Google Patents).

7. Kang, Y.-J., Kim, Y.-Y., and Lee, J.-S. (2007). Poroelastic acoustical foam having enhanced sound-absorbing performance. (Google Patents).

8. Cox, T.J., and D'antonio, P. (2009). Acoustic absorbers and diffusers: theory, design and application, (CRC Press).

9. Yang, T.L., Chiang, D.-M., and Chen, R. (2001). Development of a novel porous laminated composite material for high sound absorption. Journal of Vibration and Control *7*, 675-698.

10. Park, S.-H. (2013). Acoustic properties of micro-perforated panel absorbers backed by Helmholtz resonators for the improvement of low-frequency sound absorption. Journal of Sound and Vibration *332*, 4895-4911.

11. Chanaud, R. (1994). Effects of geometry on the resonance frequency of Helmholtz resonators. Journal of Sound and Vibration *178*, 337-348.

12. Frommhold, W., Fuchs, H., and Sheng, S. (1994). Acoustic performance of membrane absorbers. Journal of Sound and Vibration *170*, 621-636.

13. Kingan, M.J., and Pearse, J.R. (2004). Sound absorption of porous material in combination with perforated facings. Proceedings of Acoustics 2004, 83-87.

14. Chevillotte, F. (2012). Controlling sound absorption by an upstream resistive layer. Applied Acoustics *73*, 56-60.

15. Borelli, D., Schenone, C., and Pittaluga, I. (2013). Analysis of sound absorption behaviour of polyester fibre material faced with perforated panels. In Proceedings of Meetings on Acoustics, Volume 19. (Acoustical Society of America), p. 015045.

16. Abd AL-Rahman, L. , Raja, I. R. , and Roslan, A.R. (2012). Attenuation of noise by using absorption materials and barriers: A review. International Journal of Engineering and Technology *2*, 11.

17. Maa, D.-Y. (1975). Theory and design of microperforated panel sound-absorbing constructions. Scientia Sinica *18*, 55-71.

18. Maa, D.-Y. (1987). Microperforated-panel wideband absorbers. Noise Control Engineering Journal *29*, 77-84.

19. Maa, D.-Y. (1998). Potential of microperforated panel absorber. the Journal of the Acoustical Society of America *104*, 2861-2866.

20. Nocke, C., Hilge, C., and Scherrer, J.-M. (2014). Micro-perforated sheets as day-light ceilings. In INTER-NOISE and NOISE-CON Congress and Conference Proceedings, Volume 249. (Institute of Noise Control Engineering), pp. 4340-4344.

21. Auriault, J.L., and Boutin, C. (1992). Deformable porous media with double porosity. Quasi-statics. I: Coupling effects. Transport in Porous Media *7*, 63-82.

22. Auriault, J.L., and Boutin, C. (1993). Deformable porous media with double porosity. Quasi-statics. II: Memory effects. Transport in Porous Media *10*, 153-169.

23. Auriault, J.L., and Boutin, C. (1994). Deformable porous media with double porosity III: Acoustics. Transport in Porous Media *14*, 143-162.

24. Boutin, C., Royer, P., and Auriault, J.L. (1998). Acoustic absorption of porous surfacing with dual porosity. International Journal of Solids and Structures *35*, 4709-4737.

25. Atalla, N., Panneton, R., Sgard, F.C., and Olny, X. (2001). Acoustic absorption of macro-perforated porous materials. Journal of Sound and Vibration *243*, 659-678.

26. Sgard, F.C., Olny, X., Atalla, N., and Castel, F. (2005). On the use of perforations to improve the sound absorption of porous materials. Applied Acoustics *66*, 625-651.

27. B´ecot, F.-X. , Dazel, O. , and Jaouen, L. (2010). Structural effects in double porosity materials: analyticalmodeling and numerical validation.

28. Gourdon, E., and Seppi, M. (2010). On the use of porous inclusions to improve the acoustical response of porous materials: Analytical model and experimental verification. Applied Acoustics *71*, 283-298.

29. Mosanenzadeh, S.G., Naguib, H.E., Park, C.B., and Atalla, N. (2014). Development of polylactide open-cell foams with bimodal structure for high-acoustic absorption. Journal of Applied Polymer Science *131*, 1-11.

30. Mahasaranon, S., Horoshenkov, V. K. , Khan, A. , and Benkreira, H. (2012). The effect of continuous pore stratification on the acoustic absorption in open cell foams. Journal of Applied Physics *111*.

31. Mosanenzadeh, S.G. (2014). Design, characterization and modeling of biobased acoustic foams.

32. Gendron, R. (2005). Thermoplastic foam processing: principles and applications, (Boca Raton, Fla: CRC).

33. Kuczmarski, M.A., and Johnston, J.C. (2011). Acoustic Absorption in Porous Materials.

34. Lee, S.T., and Scholz, D. (2008). Polymeric Foams: Polymeric Foams : Technology and Developments in Regulation, Process, and Products, (CRC Press).

35. Lee, S.-T., and Ramesh, N.S. (2004). Polymeric foams: mechanisms and materials, (CRC press).

36. Matuana, L.M., Park, C.B., and Balatinecz, J.J. (1998). Structures and mechanical properties of microcellular foamed polyvinyl chloride. Cellular polymers *17*, 1-16.

37. Collias, D.I., Baird, D.G., and Borggreve, R.J. (1994). Impact toughening of polycarbonate by microcellular foaming. Polymer *35*, 3978-3983.

38. Collias, D., and Baird, D. (1995). Tensile toughness of microcellular foams of polystyrene, styrene-acrylonitrile copolymer, and polycarbonate, and the effect of dissolved-gas on the tensile toughness of the same polymer matrices and microcellular foams. Polymer engineering and science *35*, 1167-1177.

39. Han, X. (2003). Continuous production of microcellular foams. (The Ohio State University).

40. Chu, R.K.M. (2007). Synthesis and characterization of rotational molded polymeric foams for optimal acoustic absorption. Volume MSc. (University of Toronto), p. 144.

41. Lee, E.K. (2010). Novel manufacturing processes for polymer bead foams. Volume Dissertation/Thesis. (ProQuest, UMI Dissertations Publishing).

42. Lee, S.T., Park, C.B., and Ramesh, N.S. (2007). Polymeric foams: science and technology, (Boca Raton: CRC/Taylor & Francis).

43. Klempner, D., and Frisch, K.C. (1991). Handbook of polymeric foams and foam technology, Volume 404, (Hanser Munich etc.).

44. Chu, R.K.M. (2014). Open-cell foaming with injection molding.

45. Atalla, Y., Atalla, N., Fu, J., and Naguib, H. (2006). The effect of processing parameters on the acoustical efficiency of open-cell PMMA materials. (SAE Technical Paper).

46. Mills, N., and Zhu, H. (1999). The high strain compression of closed-cell polymer foams. Journal of the Mechanics and Physics of Solids *47*, 669-695.

47. Gibson, L.J., and Ashby, M.F. (1999). Cellular solids: structure and properties, (Cambridge university press).

48. Muehleisen, R.T., Beamer IV, C.W., and Tinianov, B.D. (2005). Measurements and empirical model of the acoustic properties of reticulated vitreous carbon. The Journal of the Acoustical Society of America *117*, 536-544.

49. Alvarez-Lainez, M., Rodriguez-Perez, M., and De Saja, J. (2008). Thermal conductivity of open-cell polyolefin foams. Journal of Polymer Science Part B: Polymer Physics *46*, 212-221.

50. Pop-Iliev, R., Lee, K.H., Chew, Y.C., and Park, C.B. (2007). ANTEC: Processing fine-celled recyclable CBA-based polyolefin foams in compression foam molding. Cellular Polymers *26*, 330.

51. Ahmed, M.Y.S.E.-S. (2008). Design and manufacturing of novel microcellular acoustical foams. Volume Dissertation/Thesis. (Canada: University of Toronto), p. 196.

52. Zhang, P., Zhou, N.Q., Wu, Q.F., Wang, M.Y., and Peng, X.F. (2007). Microcellular foaming of PE/PP blends. Journal of applied polymer science *104*, 4149-4159.

53. Park, C.P. (2003). Acoustical open-cell polylefins and process for making. (Google Patents).

54. Reichelt, N., Stadlbauer, M., Folland, R., Park, C.B., and Wang, J. (2003). PP-blends with tailored foamability and mechanical properties. Cellular polymers *22*, 315-327.

55. Naguib, H.E., Park, C.B., Lee, P.C., and Xu, D. (2006). A study on the foaming behaviors of PP resins with talc as nucleating agent. Journal of polymer engineering *26*, 565-588.

56. Doroudiani, S., and Kortschot, M.T. (2003). Polystyrene foams. I. Processing-structure relationships. Journal of Applied Polymer Science *90*, 1412-1420.

57. Rodeheaver, B.A., and Colton, J.S. (2001). Open-celled microcellular thermoplastic foam. Polymer Engineering and Science *41*, 380-400.

58. Doroudiani, S., and Kortschot, M.T. (2004). Expanded wood fiber polystyrene composites: processing–structure–mechanical properties relationships. Journal of Thermoplastic Composite Materials *17*, 13-30.

59. Wong, C.M., Tsai, S.J., Ying, C.H., and Hung, M.L. (2006). Effect of low density polyethylene on polystyrene foam. Journal of Cellular Plastics *42*, 153-163.

60. Mengeloglu, F., and Matuana, L.M. (2001). Foaming of rigid PVC/wood-flour composites through a continuous extrusion process. Journal of Vinyl and Additive Technology *7*, 142-148.

61. Xiong, C., Lu, S., Wang, D., Dong, L., Jiang, D.D., and Wang, Q. (2005). Microporous polyvinyl chloride: novel reactor for PVC/$CaCO_3$ nanocomposites. Nanotechnology *16*, 1787.

62. Lee, P.C., Guangming, L., Lee, J.W.S., and Park, C.B. (2007). Improvement of cell opening by maintaining a high temperature difference in the surface and core of a foam extrudate. Journal of Cellular Plastics *43*, 431-444.

63. Barlow, C., Kumar, V., Flinn, B., Bordia, R.K., and Weller, J. (2001). Impact strength of high density solid-state microcellular polycarbonate foams. Journal of engineering materials and technology *123*, 229-233.

64. Ito, Y., Yamashita, M., and Okamoto, M. (2006). Foam processing and cellular structure of polycarbonate-based nanocomposites. Macromolecular Materials and Engineering *291*, 773-783.

65. Huang, S., Wu, G., and Chen, S. (2007). Preparation of open cellular PMMA microspheres by supercritical carbon dioxide foaming. The Journal of supercritical fluids *40*, 323-329.

66. Zeng, C., Hossieny, N., Zhang, C., and Wang, B. (2010). Synthesis and processing of PMMA carbon nanotube nanocomposite foams. Polymer *51*, 655-664.

67. Pinto, J., Dumon, M., Pedros, M., Reglero, J., and Rodriguez-Perez, M.A. (2014). Nanocellular CO_2 foaming of PMMA assisted by block copolymer nanostructuration. Chemical Engineering Journal *243*, 428-435.

68. Quintans, J., Xanthos, M., Dey, S., and Yilmazer, U. (2000). Melt viscoelasticity of polyethylene terephthalate resins for low density extrusion foaming. Polymer Engineering & Science *40*, 554-566.

69. Xanthos, M., Wan, C., Dhavalikar, R., Karayannidis, G., and Bikiaris, D. (2004). Identification of rheological and structural characteristics of foamable poly (ethylene terephthalate) by reactive extrusion. Polymer international *53*, 1161-1168.

70. Jacobs, M.A., Kemmere, M.F., and Keurentjes, J.T. (2004). Foam processing of poly (ethylene-co-vinyl acetate) rubber using supercritical carbon dioxide. Polymer *45*, 7539-7547.

71. Rodriguez-Perez, M., Simoes, R., Roman-Lorza, S., Alvarez-Lainez, M., Montoya-Mesa, C., Constantino, C., and de Saja, J. (2012). Foaming of EVA/starch blends: characterization of the structure, physical properties, and biodegradability. Polymer Engineering & Science *52*, 62-70.

72. Dutta, J., and Naskar, K. (2014). Investigation of morphology, mechanical, dynamic mechanical and thermal behaviour of blends based on ethylene vinyl acetate (EVA) and thermoplastic polyurethane (TPU). RSC Advances *4*, 60831-60841.

73. Henderson, A.M. (1993). Ethylene-vinyl acetate (EVA) copolymers: a general review. IEEE Electrical Insulation Magazine *1*, 30-38.

74. Jeng, Y.-R., Liu, D.-S., and Yau, H.-T. (2012). Designing experimental methods to predict the expansion ratio of EVA foam material and using finite element simulation to estimate the shoe expansion shape. Materials Transactions *53*, 1685-1688.

75. Chen, N. (2012). The effects of crosslinking on foaming of EVA. Volume Dissertation/Thesis. (ProQuest, UMI Dissertations Publishing).

76. Alothman, O.Y. (2012). Processing and characterization of high density polyethylene/ethylene vinyl acetate blends with different VA contents. Advances in Materials Science and Engineering *2012*.

77. Hayman, G., Jenkin, M., Murrells, T., and Johnson, C. (1994). Trospospheric degradation chemistry of HCFC-123 (CF_3CHCl_2): A proposed replacement chlorofluorocarbon. Atmospheric Environment *28*, 421-437.

78. Zipfel, L., Barthtlemy, P., and Dournel, P. (1999). The next generation blowing agents: from one single product to a product range. Journal of cellular plastics *35*, 345-364.

79. Gendron, R., and Daigneault, L.E. (2003). Continuous extrusion of microcellular polycarbonate. Polymer Engineering & Science *43*, 1361-1377.

80. Lee, C.-D.P. (2001). Manufacture of microcellular open-celled polyolefin foams. Volume Dissertation/Thesis. (Canada: University of Toronto).

81. Lee, J.W., Wang, K., and Park, C.B. (2005). Challenge to extrusion of low-density microcellular polycarbonate foams using supercritical carbon dioxide. Industrial & engineering chemistry research *44*, 92-99.

82. Behravesh, A.H., Park, C.B., and Venter, R.D. (1998). Challenge to the production of low-density, fine-cell HDPE foams using CO_2. Cellular polymers *17*, 309-326.

83. Park, C.B., Behravesh, A.H., and Venter, R.D. (1998). Low density microcellular foam processing in extrusion using CO_2. Polymer Engineering & Science *38*, 1812-1823.

84. Lee, J.W., and Park, C.B. (2006). Use of nitrogen as a blowing agent for the production of fine-celled high-density polyethylene foams. Macromolecular Materials and Engineering *291*, 1233-1244.

85. Li, G. (2007). Thermodynamic investigation of the solubility of physical blowing agents in polymer melts, (ProQuest).

86. Pierick, D., and Janisch, R. (2001). Blowing agents and foaming process conference. Paper *19*, 1.

87. Eaves, D. (2004). Handbook of polymer foams, (GB: Ismithers Rapra).

88. Quinn, S. (2001). Chemical blowing agents: providing production, economic and physical improvements to a wide range of polymers. Plastics, Additives and Compounding *3*, 16-21.

89. Rowland, D.G. (1993). Practical chemical blowing agents for expanding rubber. Rubber Chemistry and Technology *66*, 463-475.

90. Eaves, D. (2004). Handbook of polymer foams. polimeri *25*, 1-2.

91. Baldwin, D.F., Tate, D., Park, C.B., Cha, S.W., and Suh, N. (1994). Microcellular plastics processing technology (1). Seikei-Kakou *6*, 187-194.

92. Klempner, D., Sendijarevic, V., and Aseeva, R.M. (2004). Handbook of polymeric foams and foam technology, (Hanser Verlag).

93. Lee, S.T., and Ramesh, N.S. (2004). Polymeric foams: mechanisms and materials, (Boca Raton: CRC Press).

94. Books24x, I., and Smithers, R. (2013). Blowing agents & foaming processes 2013: conference proceedings : Hilton Mainz Hotel, 14-15 May 2013, Mainz, Germany. (Shawbury, Shrewsbury, Shropshire, UK: Smithers Information Ltd).

95. Lundberg, J., Wilk, M., and Huyett, M. (1960). Solubilities and diffusivities of nitrogen in polyethylene. Journal of Applied Physics *31*, 1131-1132.

96. Throne, J.L. (2004). Thermoplastic Foam extrusion. in the foaming Process pp. 39-48.

97. Lee, P.C., Wang, J., and Park, C.B. (2006). Extrusion of microcellular open-cell LDPE-based sheet foams. Journal of Applied Polymer Science *102*, 3376-3384.

98. Park, C.B., Liu, Y.J., and Naguib, H.E. (2000). Challenge to fortyfold expansion of biodegradable polyester foams by using carbon dioxide as a blowing agent. J Vinyl Addit Techn *6*, 39-48.

99. Xu, D., Pop-Iliev, R., Park, C.B., and Fenton, R.G. (2005). Fundamental study of CBA-blown bubble growth and collapse under atmospheric pressure. Journal of Cellular Plastics *41*, 519-538.

100. Chu, R.K.M., Naguib, H.E., and Atalla, N. (2009). Synthesis and characterization of open-cell foams for sound absorption with rotational molding method. POLYMER ENGINEERING AND SCIENCE *49*, 1744-1754.

101. Wu, L., Zhang, H., Zhang, J., and Ding, J. (2005). Fabrication of three-dimensional porous scaffolds of complicated shape for tissue engineering. I. Compression molding based on flexible-rigid combined mold. Tissue Eng *11*, 1105-1114.

102. Yamsaengsung, W., and Sombatsompop, N. (2009). Effect of chemical blowing agent on cell structure and mechanical properties of EPDM foam, and peel strength and thermal conductivity of wood/NR composite–EPDM foam laminates. Composites Part B *40*, 594-600.

103. Islam, M.R. (2010). Profile extrusion of wood plastic cellular composites and formulation evaluation using compression molding. Volume MSc. (University of Ontario Institute of Technology), p. 109.

104. Luo, Y., Zhang, J., Qi, R., Lu, J., Hu, X., and Jiang, P. (2013). Polylactide foams prepared by a traditional chemical compression-molding method. Journal of Applied Polymer Science *130*, 330-337.

105. Ito, H., Kasanami, T., and Miura, S. (1984). Method of producing open-cell foamed articles of cross-linked polyolefins. (Google Patents).

106. Susumu, N., and Minoru, S. (2006). Experiments on solid-state cell nucleation in polystyrene and polycarbonate as a function of foaming temperature and foaming time. Cellular Polymers *25*, 127.

107. Tai, H., Howdle, S.M., Shakesheff, K.M., Mather, M.L., Howard, D., Wang, W., White, L.J., Crowe, J.A., Morgan, S.P., Chandra, A., et al. (2007). Control of pore size and structure of tissue engineering scaffolds produced by supercritical fluid processing. European cells & materials *14*, 64-77.

108. Zhou, C., Ma, L., Li, W., and Yao, D. (2011). Fabrication of tissue engineering scaffolds through solid-state foaming of immiscible polymer blends. Biofabrication *3*, 045003-045003.

109. Mikos, A.G., and Temenoff, J.S. (2000). Formation of highly porous biodegradable scaffolds for tissue engineering. Electronic Journal of Biotechnology *3*, 23-24.

110. Murphy, W.L., Dennis, R.G., Kileny, J.L., and Mooney, D.J. (2002). Salt fusion: an approach to improve pore interconnectivity within tissue engineering scaffolds. Tissue Eng *8*, 43-52.

111. Tran, R.T., Naseri, E., Kolasnikov, A., Bai, X.C., and Yang, J. (2011). A new generation of sodium chloride porogen for tissue engineering. Biotechnology and Applied Biochemistry *58*, 335-344.

112. Chanda, M., and Roy, S.K. (2006). Plastics Technology Handbook, Fourth Edition, (Hoboken: CRC Press).

113. Keiichi, M., Minoru, S., and Yasushi, M. (2005). Correlation of decompression time and foaming temperature on the cell density of foamed polystyrene. cellular polymers *24*, 15.

114. Velasco, J.I., Antunes, M., and Realinho, V. (2010). Foaming behaviour, structure, and properties of polypropylene nanocomposites foams. Journal of Nanomaterials *2010*, 1-11.

115. Yao, J., and Rodrigue, D. (2012). Density graded polyethylene foams produced by compression moulding using a chemical blowing agent. Cellular Polymers *31*, 189.

116. Saiz-Arroyo, C., de Saja, J.A., Velasco, J.I., and Rodríguez-Pérez, M.Á. (2012). Moulded polypropylene foams produced using chemical or physical blowing agents: structure–properties relationship. Journal of Materials Science *47*, 5680-5692.

117. Rodriguez-Perez, M.A., Simoes, R.D., Roman-Lorza, S., Alvarez-Lainez, M., Montoya-Mesa, C., Constantino, C.J.L., and de Saja, J.A. (2012). Foaming of EVA/starch blends: Characterization of the structure, physical properties, and biodegradability. Polymer Engineering & Science *52*, 62-70.

118. Lopez-Gil, A., Saiz-Arroyo, C., Tirado, J., and Rodriguez-Perez, M.A. (2015). Production of non-crosslinked thermoplastic foams with a controlled density and a wide range of cellular structures. Journal of Applied Polymer Science.

119. Tran, R.T., Thevenot, P., Gyawali, D., Chiao, J.-C., Tang, L., and Yang, J. (2010). Synthesis and characterization of a biodegradable elastomer featuring a dual crosslinking mechanism. Soft Matter *6*, 2449-2461.

120. Gong, X., Tang, C.Y., Zhang, Y., Wong, C.T., Wu, S., and Liu, J. (2012). Fabrication of graded macroporous poly(lactic acid) scaffold by a progressive solvent casting/porogen leaching approach. Journal of Applied Polymer Science *125*, 571-577.

121. Sriharsha, S.S. (2013). Fabrication and characterization of open celled micro and nano foams. (University of Texas at Austin).

122. Salerno, A., Oliviero, M., Di Maio, E., Iannace, S., and Netti, P.A. (2007). Design and preparation of μ-bimodal porous scaffold for tissue engineering. Journal of Applied Polymer Science *106*, 3335-3342.

123. Taki, K., Nitta, K., Kihara, S.I., and Ohshima, M. (2005). CO_2 foaming of poly (ethylene glycol)/polystyrene blends: Relationship of the blend morphology, CO_2 mass transfer, and cellular structure. Journal of applied polymer science *97*, 1899-1906.

124. Kieback, B., Neubrand, A., and Riedel, H. (2003). Processing techniques for functionally graded materials. Materials Science & Engineering A *362*, 81-106.

125. Barzegari, M.R., Yao, J.L., and Rodrigue, D. (2013). Mechanical properties of density graded foams: tensile properties. CELLULAR POLYMERS *32*, 323-341.

126. Jiaolian, y. (2011). Density graded LMDPE foams produced under a temperature gradient: morphology and properties. MSc (Univesité Laval).

127. Zhou, C., Wang, P., and Li, W. (2011). Fabrication of functionally graded porous polymer via supercritical CO_2 foaming. Composites Part B: Engineering *42*, 318-325.

128. Miyamoto, Y., Kaysser, W., Rabin, B., Kawasaki, A., and Ford, R.G. (2013). Functionally graded materials: design, processing and applications, Volume 5, (Springer Science & Business Media).

129. Zhang, W. (2011). Controllable growth of porous structures from co-continuous polymer blend. In Georgia Institute of Technology, Volume Dissertation/Thesis. (Georgia Institute of Technology).

130. Al Jahwari, F., Anwer, A.A.W., and Naguib, H.E. (2015). Fabrication and microstructural characterization of functionally graded porous acrylonitrile butadiene styrene and the effect of cellular morphology on creep behavior. Journal of Polymer Science Part B: Polymer Physics *53*, 795-803.

131. Landis, E.N., and Keane, D.T. (2010). X-ray microtomography. Materials characterization *61*, 1305-1316.

132. Kastner, J., Plank, B., and Salaberger, D. (2012). High resolution X-ray computed tomography of fibre-and particle-filled polymers. In 18th World Conference on Nondestructive Testing, Durban, South Africa. pp. 16-20.

133. Nikishkov, Y., Airoldi, L., and Makeev, A. (2013). Measurement of voids in composites by X-ray Computed Tomography. Composites Science and Technology *89*, 89-97.

134. Yang, P., and Elhajjar, R. (2014). Porosity content evaluation in carbon-fiber/epoxy composites using X-ray computed tomography. Polymer-Plastics Technology and Engineering *53*, 217-222.

135. Thi, T.B.N., Morioka, M., Yokoyama, A., Hamanaka, S., Yamashita, K., and Nonomura, C. (2015). Measurement of fiber orientation distribution in injection-molded short-glass-fiber composites using X-ray computed tomography. Journal of Materials Processing Technology *219*, 1-9.

136. Ma, Y., Pyrz, R., Rodriguez-Perez, M.A., Escudero, J., Rauhe, J.C., and Su, X. (2011). X-ray microtomographic study of nanoclay-polypropylene foams. Cellular Polymers *30*, 95.

137. Kelkar, S.M. (2013). Using x-ray imaging techniques to determine density of foods.

138. Chevallier, S., Réguerre, A.-L., Le Bail, A., and Della Valle, G. (2014). Determining the cellular structure of two cereal food foams by X-ray micro-tomography. Food biophysics *9*, 219-228.

139. Adedeji, A.A., and Ngadi, M.O. (2011). Microstructural characterization of deep-fat fried breaded chicken nuggets using X-ray micro-computed tomography. Journal of Food Process Engineering *34*, 2205-2219.

140. Petit, C., Meille, S., and Maire, E. (2013). Cellular solids studied by X-ray tomography and finite element modeling–a review. Journal of Materials Research *28*, 2191-2201.

141. Bock, J., and Jacobi, A.M. (2013). Geometric classification of open-cell metal foams using X-ray micro-computed tomography. Materials Characterization *75*, 35-43.

142. Bock, J.J., and Jacobi, A.M. (2012). X-ray micro-computed tomography imaging of open-cell metal foams. Journal of Heat Transfer *134*, 080911.

143. Kumar, P., Hugo, J.-M., Topin, F., and Vicente, J. (2012). Influence of pore and strut shape on open cell metal foam bulk properties. In Porous Media and its Applications in Science, Engineering, and Industry: Fourth International Conference, Volume 1453. (AIP Publishing), pp. 243-248.

144. Buyens, F., Legoupil, S., and Vabre, A (2007). Metallic foams characterization using X-ray microtomography. In International Symposium on Digital industrial Radiology and Computed Tomography.

145. Pauwels, E., Van Loo, D., Cornillie, P., Brabant, L., and Van Hoorebeke, L. (2013). An exploratory study of contrast agents for soft tissue visualization by means of high resolution X-ray computed tomography imaging. Journal of microscopy *250*, 21-31.

146. Walton, L.A., Bradley, R.S., Withers, P.J., Newton, V.L., Watson, R.E., Austin, C., and Sherratt, M.J. (2015). Morphological Characterisation of Unstained and Intact Tissue Micro-architecture by X-ray Computed Micro-and Nano-Tomography. Scientific reports *5*.

147. Tahara, R., and Larsson, H.C. (2013). Quantitative analysis of microscopic X-ray computed tomography imaging: Japanese quail embryonic soft tissues with iodine staining. Journal of anatomy *223*, 297-310.

148. Vandeweghe, S., Coelho, P.G., Vanhove, C., Wennerberg, A., and Jimbo, R. (2013). Utilizing micro-computed tomography to evaluate bone structure

surrounding dental implants: A comparison with histomorphometry. Journal of Biomedical Materials Research Part B: Applied Biomaterials *101*, 1259-1266.

149. Nakayama, H., Burns, D.M., and Kawase, T. (2011). Non-destructive microstructural analysis of porous bioceramics by microfocus X-ray computed tomography (μCT): a proposed protocol for standardized evaluation of porosity and interconnectivity between macro-pores. Journal of Nondestructive Evaluation *30*, 71-80.

150. Vergés, E., Tost, D., Ayala, D., Ramos, E., and Grau, S. (2011). 3D pore analysis of sedimentary rocks. Sedimentary Geology *234*, 109-115.

151. Jia, L., Chen, M., and Jin, Y. (2014). 3D imaging of fractures in carbonate rocks using X-ray computed tomography technology. Carbonates and Evaporites *29*, 147-153.

152. Yun, T.S., Jeong, Y.J., Kim, K.Y., and Min, K.-B. (2013). Evaluation of rock anisotropy using 3D X-ray computed tomography. Engineering Geology *163*, 11-19.

153. Fernandes, J.S., Appoloni, C.R., and Fernandes, C.P. (2012). Determination of the representative elementary volume for the study of sandstones and siltstones by X-ray microtomography. Materials Research *15*, 662-670.

154. Zhang, L., Ferreira, J.M.F., Olhero, S., Courtois, L., Zhang, T., Maire, E., and Rauhe, J.C. (2012). Modeling the mechanical properties of optimally processed cordierite-mullite-alumina ceramic foams by X-ray computed tomography and finite element analysis. Acta Materialia *60*, 4235.

155. Wallenstein, M., Hafen, N., Heinzmann, H., Schug, S., Arlt, W., Kind, M., and Dietrich, B. (2015). Qualitative and quantitative insights into multiphase flow in ceramic sponges using X-ray computed tomography. Chemical Engineering Science *138*, 118-127.

156. Rhodes, M., and Khaykin, B. (1986). Foam characterization and quantitative stereology. Langmuir *2*, 643-649.

157. Montminy, M.D., Tannenbaum, A.R., and Macosko, C.W. (2001). New algorithms for 3-D imaging and analysis of open-celled foams. Journal of cellular plastics *37*, 501-515.

158. Gosselin, R., and Rodrigue, D. (2005). Cell morphology analysis of high density polymer foams. Polymer testing *24*, 1027-1035.

159. Russ, J.C., and Russ, J.C. (2007). Introduction to image processing and analysis, (CRC press).

160. Bruker microCT Method Note MN059: Porosity analysis (2005).

161. Kumar, J., Abulrub, A.H.G., Attridge, A., and Williams, M.A. (2012). Effect of X-ray computed tomography scanning parameters on the estimated porosity of foam specimens. Applied Mechanics and Materials *110*, 808-815.

162. Maire, E. (2012). X-ray tomography applied to the characterization of highly porous materials. Annual Review of Materials Research *42*, 163-178.

163. Fernandes, J.S., Appoloni, C.R., Moreira, A.C., and Fernandes, C.P. (2007). Porosity and pore size distribution determination of tumblagooda formation sandstone by X-Ray Microtomography. In 2007 International Nuclear Atlantic Conference INAC.

164. Rémy, É., and Thiel, É. (2002). Medial axis for chamfer distances: computing look-up tables and neighbourhoods in 2D or 3D. Pattern Recognition Letters *23*, 649-661.

165. Hildebrand, T., and Rüegsegger, P. (1997). A new method for the model-independent assessment of thickness in three-dimensional images. Journal of microscopy *185*, 67-75.

166. Van Dalen, G., and Koster, M. (2012). 2D & 3D particle size analysis of micro-CT images. Unilever Res Dev Netherlands.

167. Montminy, M.D., Tannenbaum, A.R., and Macosko, C.W. (2004). The 3D structure of real polymer foams. Journal of colloid and interface science *280*, 202-211.

168. Vicente, J., Topin, F., and Daurelle, J.-V. (2006). Open celled material structural properties measurement: from morphology to transport properties. Materials transactions *47*, 2195-2202.

169. Kumar, P., Topin, F., and Vicente, J. (2014). Determination of effective thermal conductivity from geometrical properties: Application to open cell foams. International Journal of Thermal Sciences *81*, 13-28.

170. Pardo-Alonso, S., Vicente, J., Solórzano, E., Rodriguez-Perez, M.Á., and Lehmhus, D. (2014). Geometrical tortuosity 3D calculations in infiltrated aluminium cellular materials. Procedia Materials Science *4*, 145-150.

171. (2010). D6226 Standard test method for open cell content of rigid cellular plastics.

172. (2009). C522 Standard test method for airflow resistance of acoustical materials.

173. McGrory, M., Cirac, D.C., Gaussen, O., and Cabrera, D.(2012). Sound absorption coefficient measurement: Re-examining the relationship between impedance tube and reverberant room methods.

174. DIN, E. (2003). 354: Acoustics measurement of sound absorption in a reverberation room (ISO 354: 2003). German version EN ISO *354*, 2003.

175. ISO, U. 10534-1: 2002. Acoustics. determination of sound absorption coefficient and impedance in impedance tubes, Part *1*.

176. ISO, B. (2001). 10534-2: 2001. Acoustics. determination of sound absorption coefficient and impedance in impedance tubes. Transfer-function method. Geneve.

177. da Silva, G.C.C., de Araújo Nunes, M.A., Lopes, R.V., and Júnior, A.B.A. (2013). Design and construction of a low cost impedance tube for sound absorption coefficients measurements. In 22nd International Congress of Mechanical Engineering

178. Suhanek, M., Jambrosic, K., and Horvat, M. (2008). A comparison of two methods for measuring the sound absorption coefficient using impedance tubes. In ELMAR, 2008. 50th International Symposium, Volume 1. (IEEE), pp. 321-324.

179. Jones, M.G., and Stiede, P.E. (1997). Comparison of methods for determining specific acoustic impedance. The Journal of the Acoustical Society of America *101*, 2694-2704.

180. Seybert, A.F. (2003). Notes on absorption and impedance measurements. In Noise and Vibration Conference SAE, Traverse City.

181. Satyajeet P Deshpande, and Mohan D. Rao (2014). Development of a lowcost impedance tube to measure acoustic absorption and transmission loss of materials. In 121st ASEE Annual Conference and Exposition.

182. Han, J., Herrin, D., and Seybert, A. (2007). Accurate measurement of small absorption coefficients. (SAE Technical Paper).

183. Piechowicz, J. (2011). Estimating surface acoustic impedance with the inverse method. International Journal of Occupational Safety and Ergonomics *17*, 271-276.

184. Levine, H., and Schwinger, J. (1948). On the radiation of sound from an unflanged circular pipe. Physical review *73*, 383.

185. Santare, M., and Lambros, J. (2000). Use of graded finite elements to model the behavior of nonhomogeneous materials. Journal of Applied Mechanics *67*, 819-822.